GAIA-CLIM deliverable D4.6

Gap Analysis for Integrated Atmospheric ECV CLImate Monitoring:

D4.6: Individual reports on validation of satellites, version 3

A Horizon 2020 project; Grant agreement: 640276

Date: 20/12/2017

Lead beneficiary: Met Office

Nature: Report

Dissemination level: Public

Work Package	WP 4
Deliverable	D4.6
Title	Individual reports on validation of satellites, version 3
Nature	Report
Dissemination	Public
Beneficiary	Met Office
Date	20/12/2017
Status	Version 1.0 (see version control in sub-documents)
Authors	Heather Lawrence, Fabien Carminati, Jacqueline Goddard, Stuart Newman, William Bell, Niels Bormann, Stephen English, Nigel Atkinson
Reviewers	Peter Thorne, Anna Mikalsen
Contacts	**Heather Lawrence (heather.lawrence@ecmwf.int), Fabien Carminati (fabien.carminati@metoffice.gov.uk)**
URL	http://www.gaia-clim.eu/

Executive summary

Work Package 4 of the GAIA-CLIM project has investigated the role of Numerical Weather Prediction (NWP) for calibration/validation of new satellite missions. Previous WP4 reports have assessed the data quality of AMSR2 on the GCOM-W1 satellite (Deliverable 4.2) and MWHS-2/MWRI on FY-3C (Deliverable 4.5). Here, two more satellite instruments are subject to detailed assessment within the NWP framework at ECMWF and the Met Office. The individual reports follow as Annexes. Annex 1 is entitled "An Evaluation of the MTVZA-GY microwave imager/sounder on the Russian Meteor-M N2 satellite, using O-B statistics at ECMWF and the Met Office". Annex 2 is entitled "Calibration/validation study of GPM GMI".

The analysis of MTVZA-GY reveals the presence of biases (observed minus model brightness temperature departures) related to the spacecraft position relative to the sun and/or dependent on latitude, which are reminiscent of similar behavior seen for other conical scanning instruments such as SSMI/S. Some channels exhibit rather large biases (10-20 K) relative to predicted NWP brightness temperatures which are somewhat larger than those observed for similar channels on AMSR2. NWP departures are also shown to be sensitive enough to detect scan line dependent "striping" and scan angle dependent biases which are attributable to instrument calibration problems.

By contrast, when assessing the GMI instrument the magnitude of brightness temperature departures is small, with global mean biases relative to NWP within +/- 1 K for most channels. GMI is a state-of-the-art radiometer with a stringent design specification for radiometric calibration and stability. The quality of GMI data is borne out by the lack of significant biases between daytime and night-time passes, in contrast to similar imagers such as MWRI. Geographically localised biases are seen which suggest model-related rather than instrument-related origins and highlight the need for strict quality control when applying the NWP cal/val approach to missions with very high calibration standards.

An Evaluation of the MTVZA-GY microwave imager/sounder on the Russian Meteor-M N2 satellite, using O - B statistics at ECMWF and the Met Office

Heather Lawrence[1], Stuart Newman[2], William Bell[1], Niels Bormann[1], Stephen English[1], Fabien Carminati[2], Nigel Atkinson[2]

[1]European Centre for Medium-Range Weather Forecasting (ECMWF), Shinfield Park, Reading, RG2 9AX, United Kingdom, [2]Met Office, Fitzroy Road, Exeter, EX1 3PB, United Kingdom

1 INTRODUCTION

This report presents an evaluation of the MTVZA-GY (Imaging/Sounding Microwave Radiometer - improved) instrument, a microwave imager/sounder flown onboard the Russian Meteor-M N2 satellite. MTVZA-GY is a conical scanner with imaging and sounding channels sensitive to temperature and humidity at different heights of the atmosphere, as well as total column water vapour. The Meteor-M N2 satellite was launched in 2014 and provided observations up to August 2017, with data made available in near-real-time on EUMETCAST from April 2016. In August 2017, the MTVZA-GY instrument was switched off following technical issues and so can no longer be used for operational Numerical Weather Prediction (NWP) systems. However it is of potential interest for Reanalysis systems since it provides observations sensitive to temperature and humidity, which have the potential to improve the estimate of the atmospheric state.

Before assimilating a new instrument such as MTVZA-GY in NWP and/or Reanalysis systems, the data must first undergo a calibration/validation (cal/val) process in order to verify the quality of the new observations and carry out corrections if necessary. As part of this process, an important step is to compare the observations to the short-range forecasts in radiance space from either global NWP systems such as the ECMWF and Met Office systems, or Reanalysis systems such as ERA-5. Short-range forecasts (or background fields) for temperature and humidity are highly accurate and have been shown to be a powerful tool for the assessment of new satellite data (Lu et al., 2011, Newman et al., 2016, Lawrence et al., 2017). They allow for a global assessment of satellite data and for inter comparisons between data from new instruments and instruments which are known to be of good quality. To do such an assessment, the short-range forecasts at the time of observation are transformed into radiance space and compared to the observations. The chief diagnostic for this comparison is the observation minus background fields in radiance space (O - B's), also known as the background departures. Once these have been calculated for a new instrument they can be compared to statistics of a similar instrument of good quality. This highlights any potential issues and allows for an assessment of the quality of the data in comparison to other instruments.

In work package 4 of the GAIA-CLIM project, evaluations of new satellite data have been carried out for a number of different satellite instruments, in order to both explore and demonstrate the power of using NWP short-range forecasts as a reference for satellite data cal/val. This report is part of that

series, summarising the results of the assessment of the MTVZA-GY instrument. It follows on from initial assessments carried out by Uspensky et al. (2015) for data in 2015.

This report is organised as follows. Firstly the MTVZA-GY instrument is described in section 2, then the calculation of O - B values is described in section 3 and the cloud screening in section 4. Finally results are presented in section 5 and conclusions in section 6.

2   The MTVZA-GY instrument

The MTVZA-GY instrument (Uspensky et al., 2015, Mitnik et al., 2016) is a conical scanning microwave sounding/imaging instrument flown on the Russian Meteor-M satellite series. In this report we evaluate the instrument flown onboard the second satellite in this series (Meteor-M N2), which was launched in 2014 and took measurements up to August 2017. MTVZA-GY has microwave imager channels, sensitive to total column water vapour and cloud, microwave temperature sounding channels and microwave humidity sounding channels. MTVZA-GY is similar to the Special Sensor Microwave Imager/Sounder (SSMI/S) instrument flown on the Defence Meteorological Satellite Program satellite series (F-15 to F-18), which also has imaging and sounding channels. However it measures at a higher Earth incidence angle of 65° (rather than 53.1° for SSMI/S), and the frequencies of some channels are different. In particular, the MTVZA-GY instrument has additional imaging channels at 31.5 GHz, 42.0 GHz and 48 GHz (H and V polarisation) and some of the temperature sounding channels have different central frequencies to other instruments (as shown in Table 2). However, observations are not available for the 42 GHz and 48 GHz channels and so they are not considered in this study. The channels evaluated are listed in Table 2, along with their central frequencies and polarisations. Similar channels on the Advanced Microwave Scanning Radiometer - 2 (AMSR-2), SSMI/S, and the Advanced Microwave Sounding Unit-A (AMSU-A) instruments are also given.

In this study we evaluate the MTVZA-GY data using both ECMWF and Met Office background fields, for the period of February - August 2017. This study follows on from an initial evaluation of MTVZA-GY carried out using ECMWF O - B statistics for 24 hours of data, in 2015 (Uspensky et al., 2015).

3   Calculating O - B statistics

Observation minus background statistics were calculated for the MTVZA-GY instrument using the ECMWF and Met Office background fields transformed into radiance space. Unlike previous studies in the GAIA-CLIM project (and elsewhere) this was done offline, using the forecast fields stored in the operational runs of the NWP systems. These forecast fields were interpolated to the observation time and location and transformed into brightness temperatures using the RTTOV radiative transfer model (Saunders et al., 1999, Lupu and Geer, 2015, Hocking et al., 2015, 2017). The transformation of ECMWF background fields was done using version 11.2 of RTTOV (the same as the current ECMWF operational system), and version 12 (the most recent version) was used for transforming the Met Office background fields into radiance space. Normally it would be best to use the same version of RTTOV for both ECMWF and the Met Office calculations in radiance space (as done for GMI for example), to check that differences between ECMWF and Met Office statistics are not due to the different versions of RTTOV. However, in this study it was found that O - B statistics were dominated by instrument-

Table 1: MTVZA-GY channel numbers and frequencies. Note that the MTVZA-GY channel numbers follow those of RTTOV (the same as those shown on the World Meteorological Organization's (WMO's) OSCAR database), rather than the channel numbers given in the hdf files. Observations from some channels were not available for the period considered and so were not evaluated: only those evaluated are shown in this table. Equivalent channels of AMSR-2, SSMI/S and AMSU-A are also shown. Note that there are some small differences between the channel frequencies of MTVZA-GY and the other instruments and in some cases the MTVZA-GY falls between two channel frequencies, as indicated.

MTVZA-GY channel number	MTVZA-GY central frequency	AMSR-2 channel equivalent	SSMI/S channel equivalent	AMSU-A channel equivalent
1	10.66 (V)	5	-	-
2	10.66 (H)	6	-	-
3	18.71 (V)	7	13	-
4	18.71 (H)	8	12	-
5	23.82 (V)	9	14	-
6	23.82 (H)	10	-	-
7	31.52 (V)	-	-	2
8	31.52 (H)	-	-	-
9	36.73 (V)	11	16	-
10	36.73 (H)	12	17	-
15	52.8 (V)	-	2	4
16	53.3 (V)	-	3/4	4/5
17	53.8 (V)	-	3/4	5
18	54.7 (V)	-	4/5	6/7
19	55.7 (V)	-	5/6	8
20	$57.29 \pm 0.32 \pm 0.1$ (H)	-	-	10/11
21	$57.29 \pm 0.32 \pm 0.05$ (H)	-	-	11
22	$57.29 \pm 0.32 \pm 0.025$ (H)	-	-	12
23	$57.29 \pm 0.32 \pm 0.01$ (H)	-	-	13
24	$57.29 \pm 0.32 \pm 0.005$ (H)	-	-	14
25	91.72 (V)	13	17	-
27	183.31 ± 7 (V)	-	11	-
28	183.31 ± 3 (V)	-	10	-
29	183.31 ± 1 (V)	-	9	-

related biases for most channels. The exception was for the lower-peaking temperature sounding channels - the influence of the RTTOV version for these channels is discussed in section 5.2. At ECMWF most imagers and humidity-sounding instruments are assimilated in all-sky conditions, where the background brightness temperatures are calculated for both clear and cloudy conditions. However, for the purposes of this evaluation the background-equivalent brightness temperatures were calculated for clear-sky conditions only.

The evaluation of MTVZA-GY was carried out over ocean only, where surface emissivity modelling is more reliable, with an additional screening which keeps data only between the latitudes of 60°N and 60°S, to remove any data which are over sea-ice. The ocean surface emissivity was calculated using the FAST Emissivity Model (FASTEM), which is integrated into RTTOV. Version 5 was used for the ECMWF background calculation and version 6 for the Met Office calculation. Note that the differences between these versions of FASTEM have been characterised by Kazumori and English (2015) and by Saunders et al. (2017).

Many of the MTVZA-GY channels are sensitive to cloud and precipitation, including all imager channels, all humidity-sounding channels, and the lower-peaking temperature sounding channels (channels 15 - 19). While the cloud and precipitation information can be very useful in a data assimilation system, for the purposes of satellite calibration/validation it is important to screen observations sensitive to cloud and precipitation, as these can have very high background departures which dominate statistics. The cloud/precipitation screening used for this evaluation is described in section 4.

4   Cloud Screening

In order to identify observations affected by cloud and/or precipitation, we used the cloud predictor based on the difference between the 36.73 GHz observations at V polarisation (37V observations), and those at H polarisation (37H observations). This cloud predictor is used in the ECMWF all-sky assimilation scheme for defining the observation errors of microwave imagers, and has been used in previous evaluation studies for screening cloud including the first and second year GAIA-CLIM work package 4 reports (Newman et al., 2016, Lawrence et al., 2017). The observation cloud predictor C_{37}^o is calculated as $1 - P_{37}^o$, where P_{37}^o is given by:

$$P_{37}^o = \left(T_v^o - T_h^o \right) / \left(T_{v\_clear}^b - T_{h\_clear}^b \right),$$ (1)

where T_v^o and T_h^o are the 37V and 37H observations respectively, and T_{v_clear} and T_{h_clear} are the clear-sky background brightness temperatures for these channels.

This cloud predictor is usually calculated before bias correction. However, the 36.73 GHz observations were found to have global biases of a high magnitude, and so before applying (1), the observation brightness temperatures were corrected for a global bias value. This value was calculated as the mode of the O - B values for a 12-hour period. Different values were calculated for ECMWF and the Met Office statistics. The brightness temperatures were corrected as follows:

37V channel, Met Office:

$T_{v,corrected}^o = T_v^o - 9.75K$
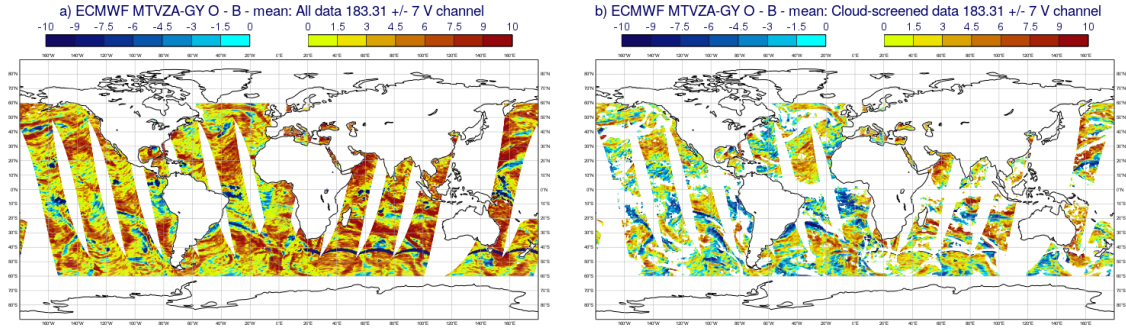
Figure 1: Maps of ECMWF O - B for the lowest peaking 183.31 GHz channel, shown a) before and b) after cloud screening.

37V channel, ECMWF:

$$T^o_{v,corrected} = T^o_v - 9.1K$$

37H channel, Met Office:

$$T^o_{h,corrected} = T^o_h + 15.91K$$

37H channel, ECMWF:

$$T^o_{h,corrected} = T^o_h + 16.75.$$

C^o_{37} was calculated from the corrected brightness temperatures and the data screened for cloud, keeping data below a threshold of 0.04 for ECMWF and 0.05 for the Met Office. Note that the Met Office departures were also screened for the background cloud amount (calculated in the same way as C^o_{37} with the all-sky background radiances used instead of observations) with the same threshold of 0.05. Once the cloud screening had been applied to both sets of O - B values, we then also matched the longitudes and latitudes of the Met Office and ECMWF values and kept only the observations appearing in both samples. Thus in the following we compare exactly the same sample of data. As an illustration of the cloud-screening applied, Fig. 1 shows a map of O - B for the lowest peaking 183 GHz channel, before and after cloud-screening, shown for the ECMWF statistics.

5 Results

Observation minus background (O - B) statistics were analysed for the MTVZA-GY instrument, using both the ECMWF and Met Office background fields, for the period February - August 2017. The main results are summarised in section 5.1 for the imager channels, section 5.2 for the temperature-sounding channels and section 5.3 for the humidity sounding channels.

5.1 Imager channels

Maps of O - B for selected imager channels of MTVZA-GY are shown in Figs. 3 - 5 for a 12-hour period on 1 February 2017. For comparison, maps are also shown for ECMWF O - B values for the
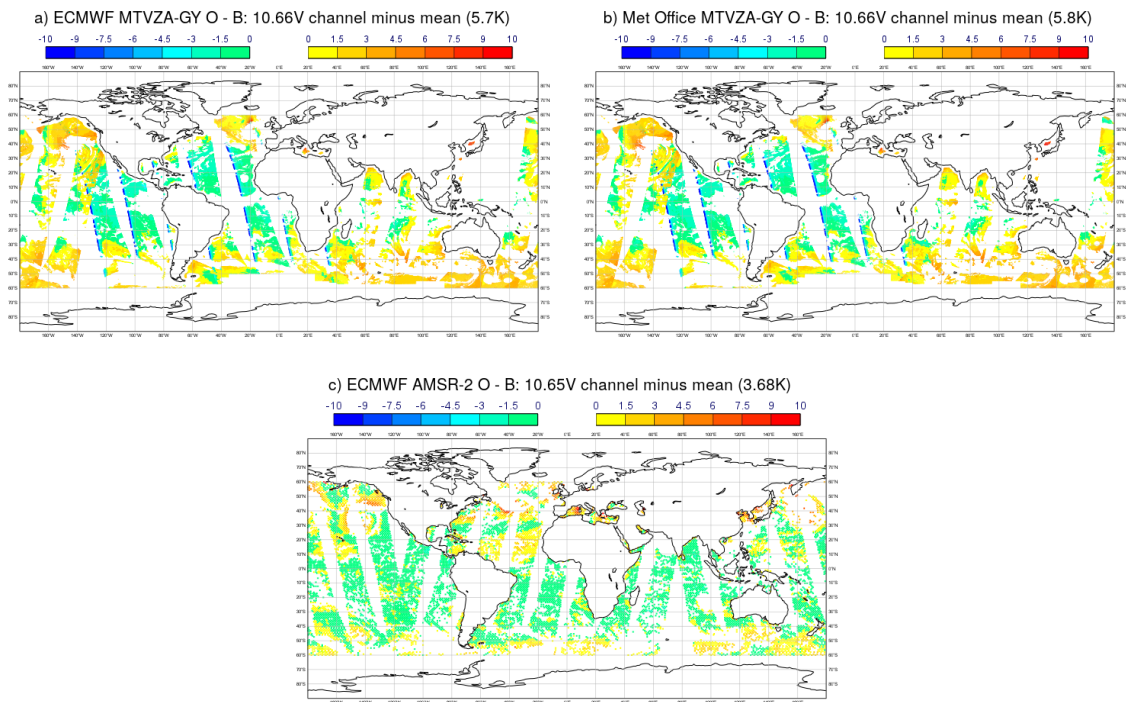
Figure 2: Maps of O - B for the 10.66 GHz, V polarisation (10.66V) channel of MTVZA-GY, on 2 February 2017, shown for calculations using a) ECMWF background fields, and b) Met Office background fields. A map of ECMWF O - B for the equivalent channel of AMSR-2 is also shown (c).

equivalent channels of AMSR-2. Note that O - B values for AMSR-2 are taken from those calculated in the ECMWF operational system for the same date, for all data over ocean after applying a cloud screening (as used for the ECMWF online monitoring of data). Although the instrument is assimilated in all-sky conditions, the clear-sky background departures are also calculated and these are the values shown in these plots. Since the AMSR-2 O - B values were calculated in the operational system, a grid-based thinning was applied, unlike for MTVZA-GY. There is also a small difference in the time period, with MTVZA-GY data plotted for the available data in the full 24-hours on 1 February 2017 and AMSR-2 for data from 21:00 31 January to 09:00 on 1 February (the time period for the 0z cycle of the ECMWF operational system).

As Figs. 2 and 3 show, the 10.66 GHz channels show a clear ascending/descending bias for both the ECMWF and Met Office statistics which is not observed in the departures for AMSR-2. This bias is similar to those observed previously for SSMI/S instruments (Geer et al., 2010) and for the MWRI instrument (Lawrence et al., 2017) and indicates an instrument-related error likely due to solar heating of the instrument. Similar biases have been observed in previous conical scanners since the calibration measurements of these instruments involves the use of a different reflector to the Earth-scene measurements. If the reflector coating of one or more of the reflectors degrades then it can become emissive, leading to the instrument measuring an additional (unknown) emission from a reflector, which itself varies depending on the heating and cooling of the reflector throughout the orbit. Such orbital biases have been successfully corrected by bias correction schemes, however, such as using the orbital angle (Booton et al., 2014) or the solar hour (Geer et al., 2010).

The other imager channels of MTVZA-GY do not have an obvious ascending/descending bias, as
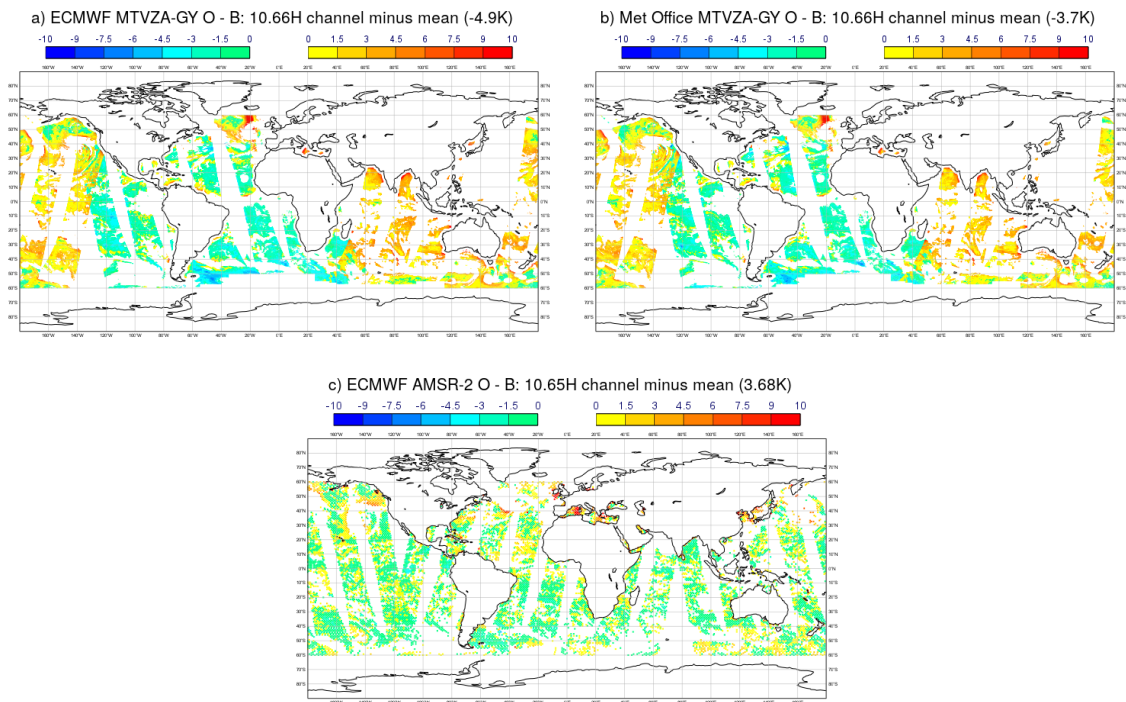
Figure 3: Maps of O - B for the 10.66 GHz H polarisation (10.66H) channel of MTVZA-GY, on 2 February 2017, shown for calculations using a) ECMWF background fields, and b) Met Office background fields. A map of ECMWF O - B for the equivalent channel of AMSR-2 is also shown (c).

shown in Figs. 4 - 5 for the 23.82 GHz channels. However there may be a bias there which is masked by the higher variation in the background departures. To test this, O - B values would need to be analysed as a function of latitude and time (for example) or as a function of the orbital angle for a long time series (see e.g. Booton et al. (2014) for a similar analysis).

In addition to the orbital-dependent biases, the 10.66 GHz channels of MTVZA-GY have strong assymetric scan angle biases, particularly the H-polarisation channel (see Fig. 2). For these channels, the scan-angle bias is also different between ascending and descending passes, which is not something seen before in O - B statistics. This type of bias must be instrument-related since it cannot be a bias in the forecast fields or in the radiative transfer model (since the viewing angle is the same across the scan position). An assymetric scan-angle bias often indicates that the satellite platform is in the field of view at the edge of the scan-line. Since the scan-angle bias is different for ascending and descending passes, the cause is also likely related to the heating/cooling of the instrument. Further investigation is needed to understand this.

As well as orbital and scan-angle biases, it was found that all of the V polarisation imager channels of MTVZA-GY have a similar latitude-dependent bias, with the extra-Tropics warmer than the Tropics. This is strongest for the 23.82 GHz, V polarisation channel, shown in Fig. 4, and is not seen for imager channels of AMSR-2, also shown in the Figure. There is also the opposite pattern visible in the H polarisation channels, as shown for the 23.82 GHz, H polarisation channel of MTVZA-GY in Fig. 5. This latitude-dependent bias has a smaller magnitude for the H channels, however. Similar latitude-dependent biases are also seen for the low-peaking temperature-sounding channels (see section 5.2). Since this type of bias is not observed in imager channels of other instruments, it appears to be an
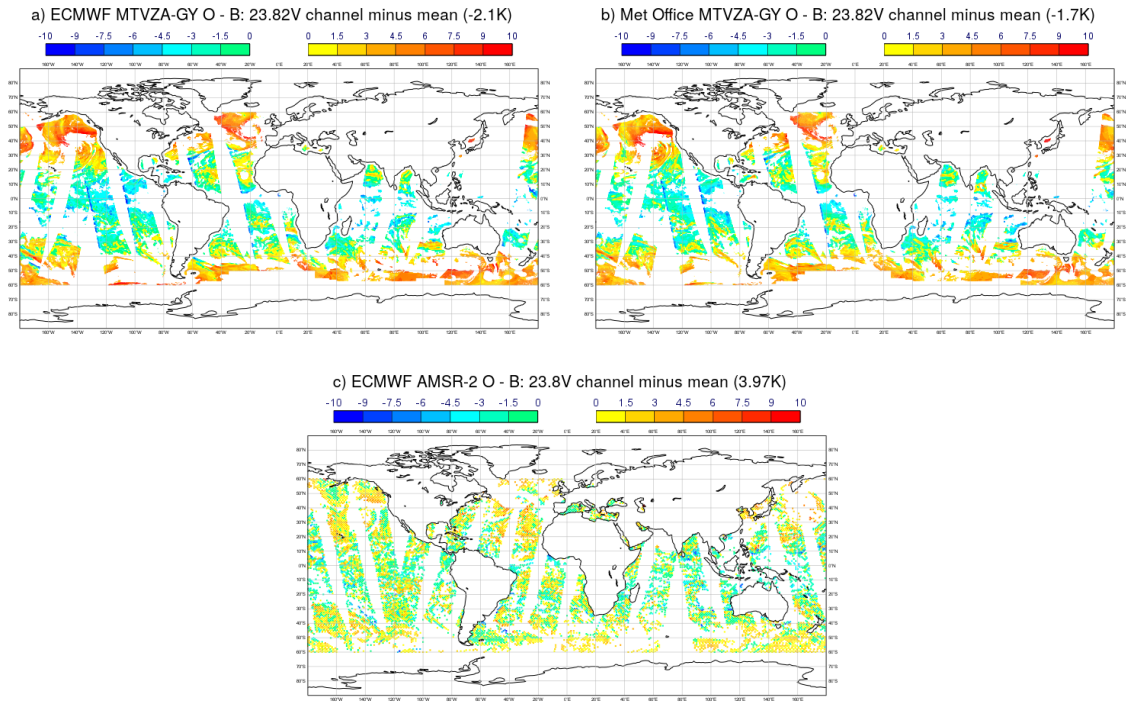
Figure 4: Maps of O - B for the 23.82 GHz V polarisation (23.8V) channel of MTVZA-GY, on 2 February 2017, shown for calculations using a) ECMWF background fields, and b) Met Office background fields. A map of ECMWF O - B for the equivalent channel of AMSR-2 is also shown (c).

instrument-related problem. One possibility is that it is due to a non-linear calibration error, which would lead to biases varying with scene temperature. It could also be due to the actual passbands for these channels not being consistent with the specified passbands used in the RTTOV calculations.

The mean O - B values for the imager channels averaged over 5 days of data are shown in Fig. 6a in comparison to equivalent channels of AMSR-2 (calculated for the same 5 days and clear-sky background departures after cloud screening and over ocean). As shown in this Figure, the 10.66 GHz channels have a similar magnitude of bias in comparison to AMSR-2, but the magnitude of bias is much higher for the higher frequency channels. The bias magnitude is particularly large for the 31.52 GHz, H polarisation channel, and for the 36.73 GHz, V and H polarisation channels, where the magnitude is of the order 10 - 20 K. This is much larger than the biases of both AMSR-2 and other imager instruments, which tend to be of the order 1 - 4 K. The standard deviation, shown in Fig. 6b, is also higher than for equivalent channels of AMSR-2. This increased standard deviation is likely due to the latitude-dependent biases observed in the maps of O - B.

5.2 Temperature-sounding channels

The temperature-sounding channels of MTVZA-GY show some striping features, similar to those of ATMS and MWHS-2 (Bormann et al., 2013, Lu et al., 2015), visible for channels 15, 16, 18 and 19. This can be seen in Fig. 7 which shows the ECMWF departures for channel 16 for a small zone near South-Western Africa (data for 1 February 2017). Such striping features do not preclude assimilation however, since the ATMS and MWHS-2 instruments have been successfully assimilated in
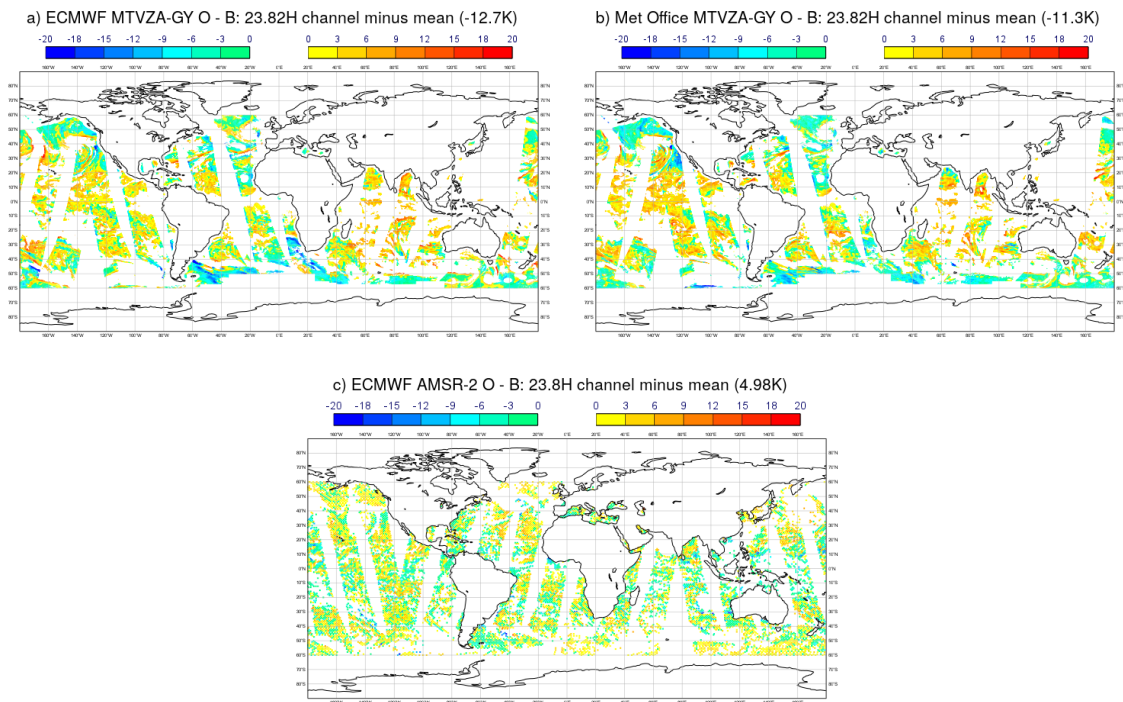
Figure 5: Maps of O - B for the 23.82 GHz H polarisation (23.8H) channel of MTVZA-GY, on 2 February 2017, shown for calculations using a) ECMWF background fields, and b) Met Office background fields. A map of ECMWF O - B for the equivalent channel of AMSR-2 is also shown (c).
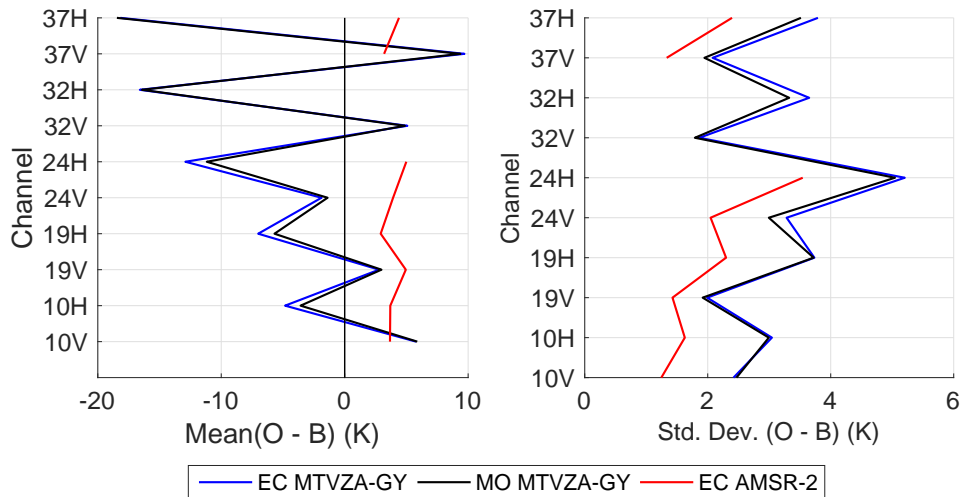

Figure 6: a) Mean and b) Standard deviation of the O - B values for the imager channels of MTVZA-GY, averaged over 5 days of data. Values are shown for ECMWF (EC) and the Met Office (MO). Note that on the y-axis a shorthand is used to refer to each channel e.g. 10H refers to the 10.66 GHz H polarisation channel, 10V the 10.66 GHz V polarisation channel, etc. ECMWF Statistics for the equivalent channels of AMSR-2 are also shown.

operational NWP systems despite the striping noise. There are also orbital-dependent biases for the temperature-sounding channels of MTVZA-GY which are similar to those observed previously for the temperature-sounding channels of SSMI/S (Bell et al., 2008). The orbital-dependent biases are visible
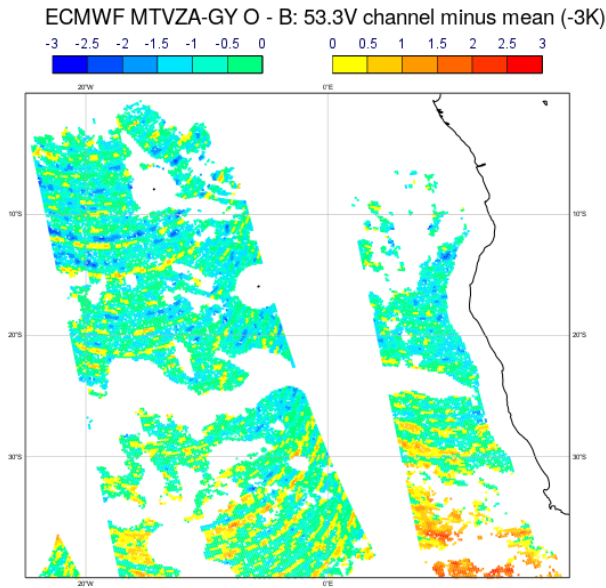
Figure 7: Map of the ECMWF O - B for MTVZA-GY channel 16 (53.6 GHz, V polarisation) for an area in the Atlantic ocean near Southern Africa.
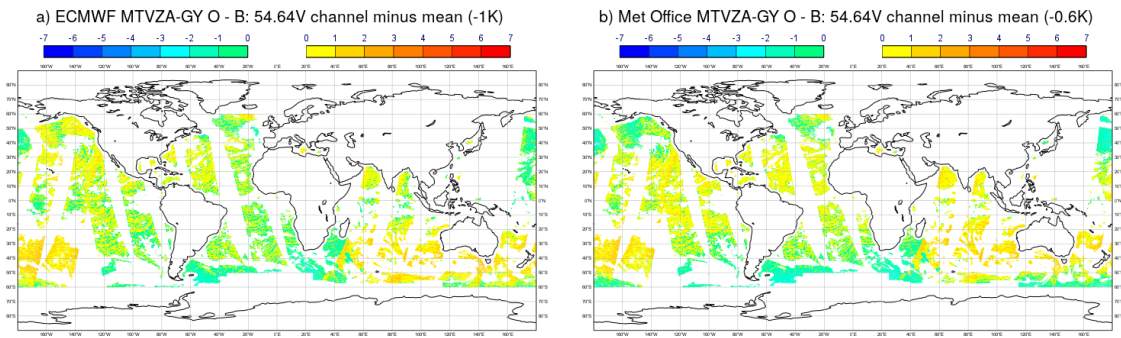

Figure 8: Maps of O - B for temperature-sounding channel 18 (54.64 GHz V polarisation) of MTVZA-GY, on 2 February 2017, shown for calculations using a) ECMWF background fields, and b) Met Office background fields.

for all temperature-sounding channels, but are strongest for the two highest peaking channels (channels 23 and 24). However, the pattern appears to be 'backwards' for channels 23 and 24 in comparison to the other temperature-sounding channels. For these latter two channels there are warm areas which are cold in the other channels and vice versa. This is illustrated in fig. 9 for channel 19 and Fig. 10 for channel 24.

Besides the striping and orbital-dependent biases, which are visible in most channels, channels 16 and 17 show a similar latitude-dependent bias to the imager channels, discussed in section 5.1. This is shown in Figs. 11 and 12. It is difficult to know what is causing this, but the magnitude for channel 17 is particularly large ($\sim$10 K), making it unlikely to be due to a model problem (e.g. a latitude-dependent forecast model error or an emissivity error). Note that orbital-dependent biases and striping are not observed for channels 16, and 17, but this is most likely due to such biases being masked by this larger latitude-dependent bias.
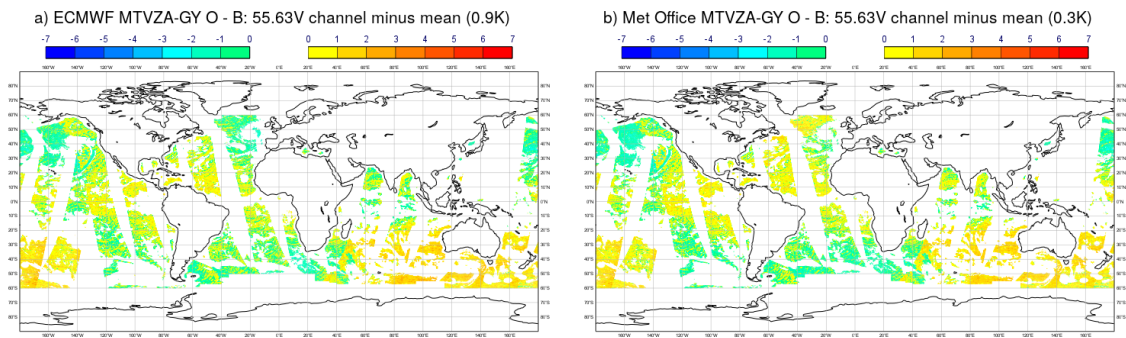
Figure 9: Maps of O - B for temperature-sounding channel 19 (53.65 GHz V polarisation) of MTVZA-GY, on 2 February 2017, shown for calculations using a) ECMWF background fields, and b) Met Office background fields.
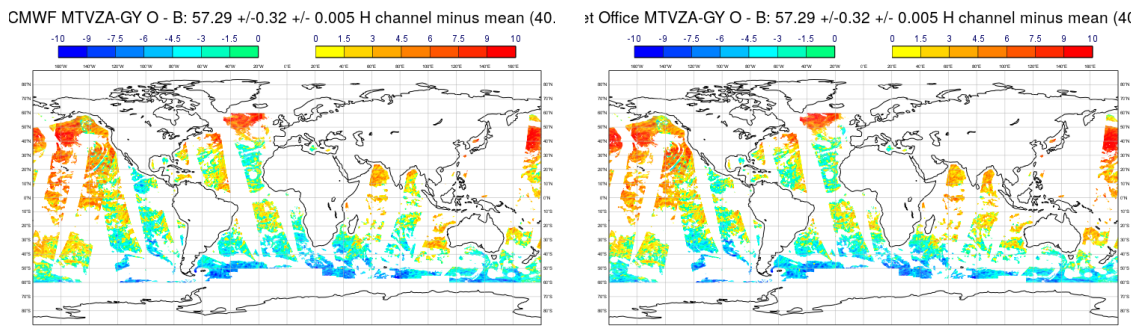

Figure 10: Maps of O - B for temperature-sounding channel 24 (57.29 $\pm$ 0.32 $\pm$ 0.005 GHz, H polarisation) of MTVZA-GY, on 2 February 2017, shown for calculations using a) ECMWF background fields, and b) Met Office background fields.
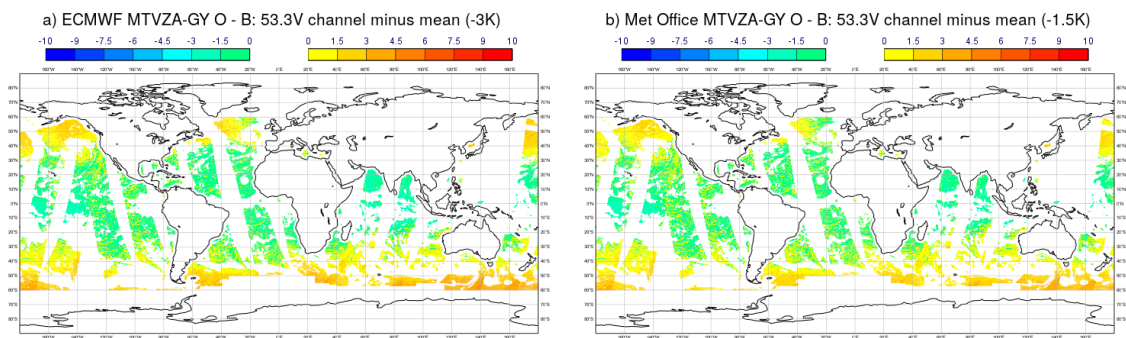
Figure 11: Maps of O - B for temperature-sounding channel 16 (53.3 GHz, V polarisation) of MTVZA-GY, on 2 February 2017, shown for calculations using a) ECMWF background fields, and b) Met Office background fields.

Channels 23 and 24 were found to have very large biases, of order 15 K, and 20 K, as illustrated in Fig. 13. This could be related to the strong orbital-dependent biases seen for these channels, or could also indicate additional problems, such as Radio Frequency Interference (RFI) on the satellite instrument, or that the channel frequencies are mis-specified. The mean and standard deviation of O - B, averaged over 5 days, is also shown in Fig. 14, with these two channels excluded. The biases and standard

11
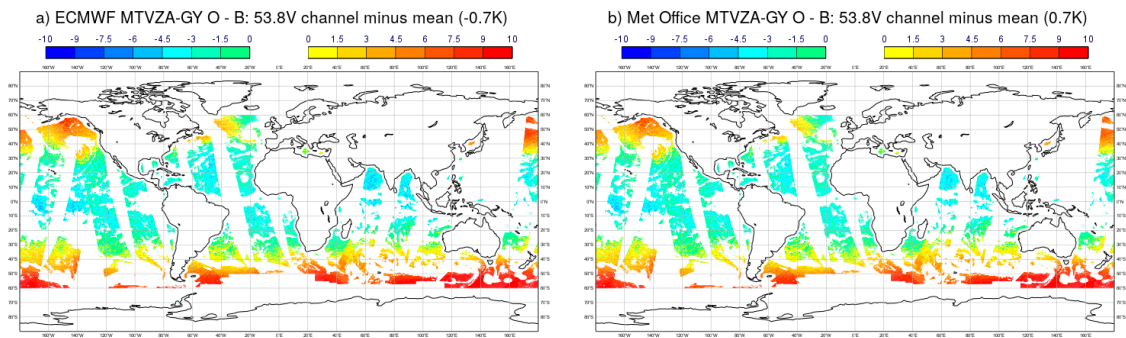
Figure 12: Maps of O - B for temperature-sounding channel 17 (53.8 GHz, V polarisation) of MTVZA-GY, on 2 February 2017, shown for calculations using a) ECMWF background fields, and b) Met Office background fields.
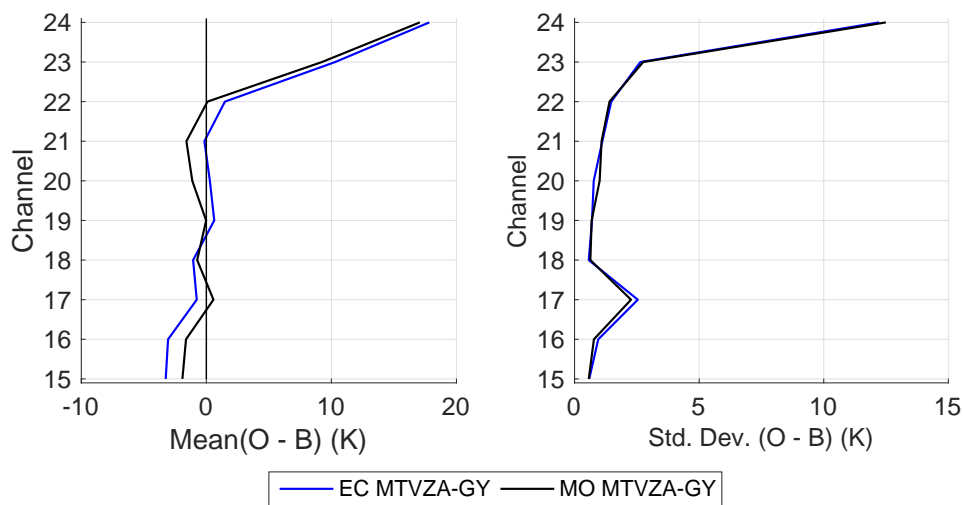

Figure 13: a) Mean and b) Standard deviation of the O - B values for the temperature-sounding channels of MTVZA-GY, averaged over 5 days of data. Values are shown for ECMWF (EC) and the Met Office (MO). Statistics are also shown for the equivalent channels of F-17 SSMI/S (clear-sky statistics averaged over the same 5 days).

deviations are much lower for the remaining channels. The magnitude of biases for channels 17 - 22 are generally of the order ∼1 K. This is much lower than for channels 23 and 24 but is still a little higher than would be expected of temperature sounding channels - usually biases of 0 - 0.5 K are observed. However these higher values may be due to the problems causing the orbital-dependent biases, which could potentially be corrected with a bias correction scheme such as the one developed by Booton et al. (2014) for SSMI/S. The lowest peaking temperature sounding channels (15 and 16) have quite a high magnitude of bias (2 - 4 K) and there are also unexpectedly large differences between the Met Office and ECMWF statistics (∼1K). Further investigation would be needed to understand the cause of these differences. One possibility is that they are due to the different versions of either RTTOV or FASTEM used for Met Office and ECMWF statistics.
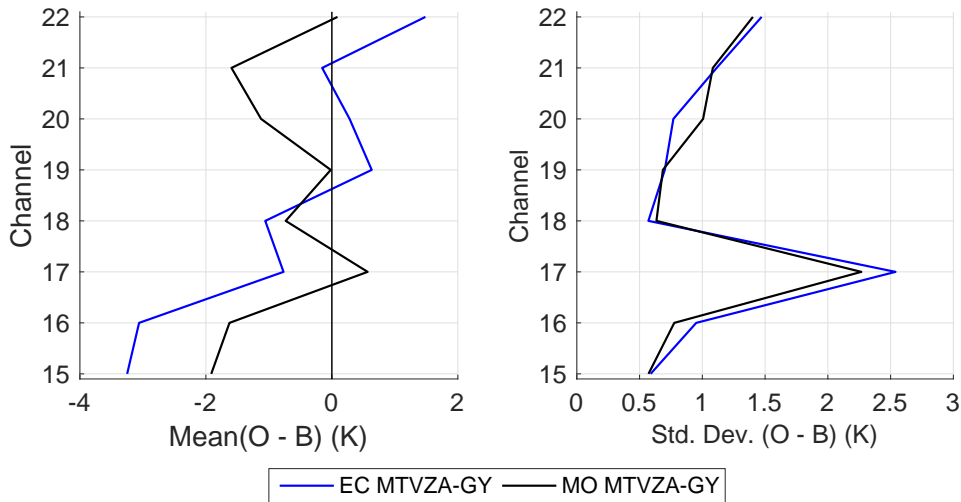
Figure 14: As Fig. 13 but excluding channels 23 and 24.
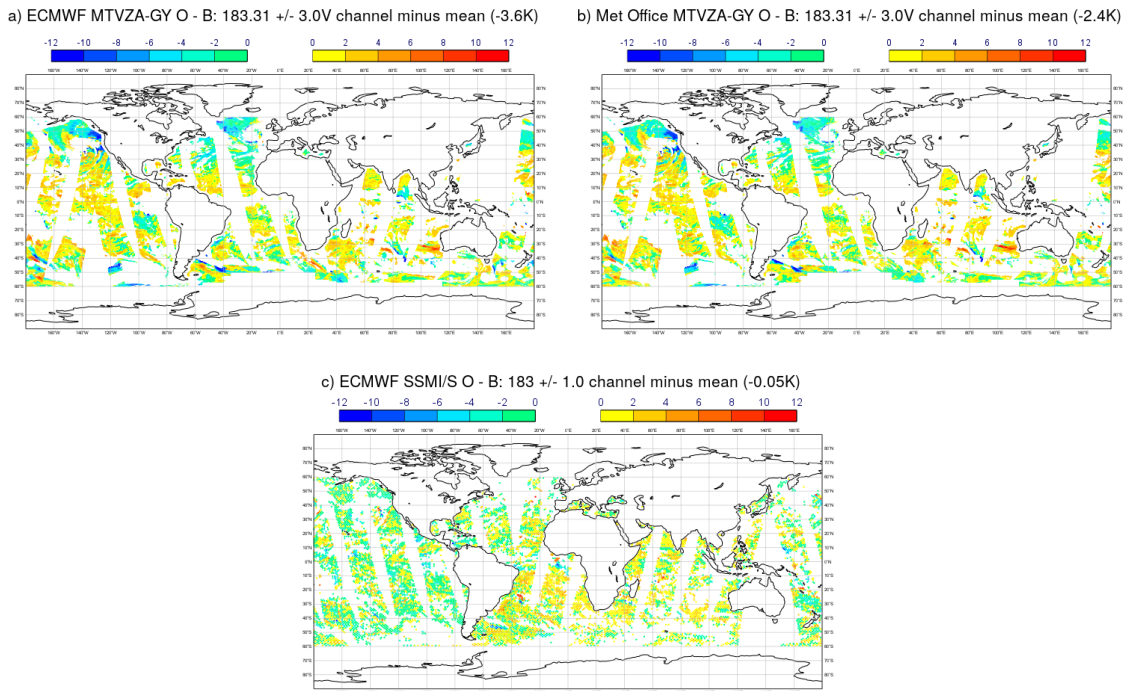
Figure 15: Maps of O - B for temperature-sounding channel 27 (183.31 ± 3 GHz, V polarisation) of MTVZA-GY, on 2 February 2017, shown for calculations using a) ECMWF background fields, and b) Met Office background fields. A map of ECMWF O - B for the equivalent channel of F-17 SSMI/S is also shown (c).

5.3 Humidity-sounding channels

Maps of O - B are shown in Figs. 15 - 17 for the humidity-sounding channels of MTVZA-GY, for 1 February 2017, with maps also shown for the ECMWF O - B of equivalent channels of F-17 SSMI/S for comparison. Note that as for AMSR-2, the O - B values for SSMI/S were taken from those stored during the operational ECMWF model run at the time (1 February 2017). Although the instrument is
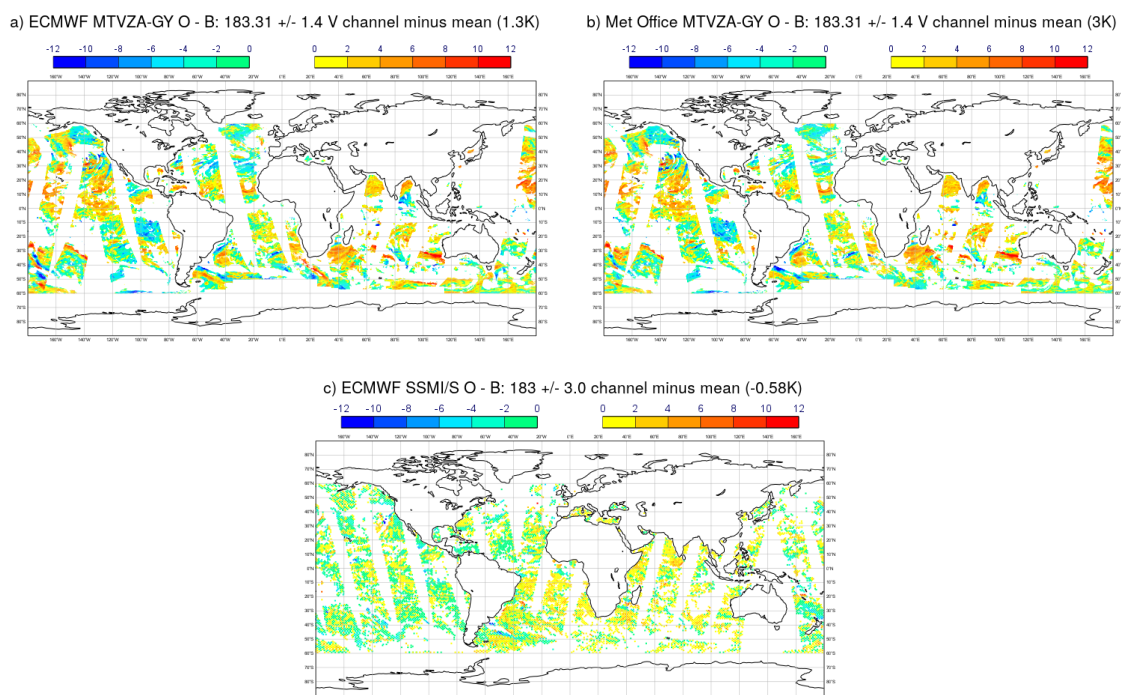
Figure 16: Maps of O - B for temperature-sounding channel 28 (183.31 $\pm$ 1.4 GHz, V polarisation) of MTVZA-GY, on 2 February 2017, shown for calculations using a) ECMWF background fields, and b) Met Office background fields. A map of ECMWF O - B for the equivalent channel of F-17 SSMI/S is also shown (c).

assimilated in all-sky conditions, the clear-sky background departures are also stored and these values are shown in this plot. Statistics are shown for SSMI/S after thinning and after applying a cloud screening (following the screening method applied in the online monitoring of the data). The SSMI/S data are for the period 21:00 31 January - 09:00 1 February, as for the operational ECMWF 0z cycle, and the MTVZA-GY data are shown for all available data on 1 February.

As Figs. 15 - 17 show, there is an orbital-dependent bias for the humidity-sounding channels of MTVZA-GY, similar to the temperature-sounding channels. The top part of the ascending orbit is cold and the bottom part of the descending orbit warm, similar to channel 19 for example, shown in Fig. 9.

The mean and standard deviation of O - B were calculated for 5 days for these channels and values are shown in Fig. 18, in comparison to the equivalent channels of F-17 SSMI/S. As this Figure shows, the humidity-sounding channels of MTVZA-GY have a higher magnitude of bias and higher standard deviation than equivalent channels of other instruments. This is likely due partly to the orbital-dependent bias, but it also indicates other issues, such as the instrument central frequency being mis-specified, or Radio Frequency Interference (RFI). This would need to be further investigated before assimilation of these channels could be tested.

14
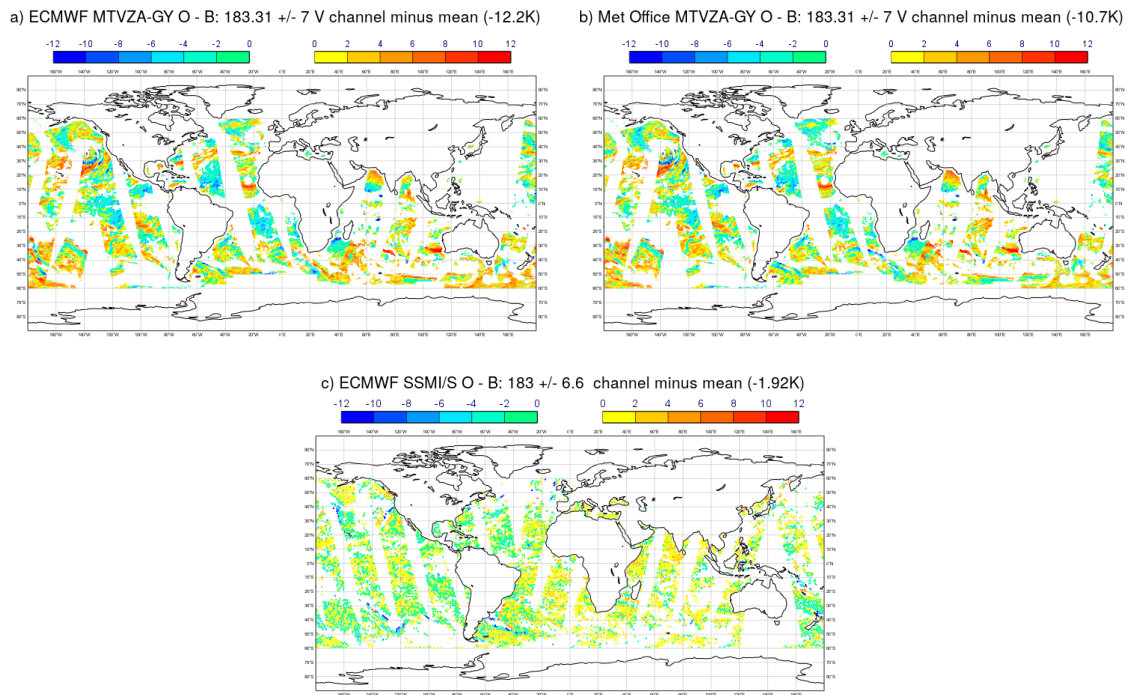
Figure 17: Maps of O - B for temperature-sounding channel 29 (183.31 $\pm$ 7.0 GHz, V polarisation) of MTVZA-GY, on 2 February 2017, shown for calculations using a) ECMWF background fields, and b) Met Office background fields. A map of ECMWF O - B for the equivalent channel of F-17 SSMI/S is also shown (c).
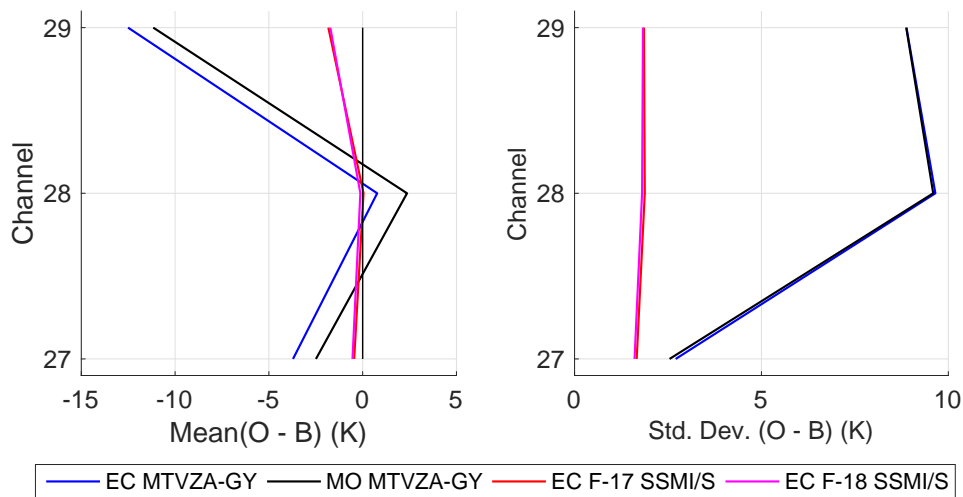

Figure 18: a) Mean and b) Standard deviation of the O - B values for the humidity-sounding channels of MTVZA-GY, averaged over 5 days of data. Values are shown for ECMWF (EC) and the Met Office (MO). The ECMWF O - B statistics are also shown for equivalent channels of F-17 and F-18 SSMI/S for comparison. These were calculated for clear sky background fields, after cloud screening, and for the same days as the MTVZA-GY data.

6 Conclusions and Perspective

In this study we have evaluated the quality of the data from the MTVZA-GY instrument, flown on the Meteor-M N2 satellite, using O - B statistics. This indicated a number of instrument-related problems including:

- orbital-dependent biases for most channels which are most likely due to solar heating of the instrument combined with an emissive reflector. Such a bias could potentially be corrected during assimilation in a variational bias correction scheme with use of a bias predictor such as the orbital angle (Booton et al., 2014) or the solar hour (Geer et al., 2010). This would require further work, however, to develop such a bias correction scheme,

- Large magnitude of bias for most channels, particularly the 2 highest peaking temperature sounding channels (10 - 20 K bias), the 24 - 37 GHz imager channels (5 - 20 K magnitude of bias), and the lowest-peaking humidity sounding channel (-10 K bias),

- Latitude-dependent biases for the imager channels and the lowest peaking temperature-sounding channels, which had a high magnitude for some channels ($\sim$10 K for channel 17),

- Striping noise observed for some of the temperature-sounding channels, similar to that observed previously for ATMS and MWHS-2 instruments,

- Strong scan-angle biases for the 10.66 GHz channels.

The orbital-dependent biases were observed previously by Uspensky et al. (2015). However in comparison to this previous study, the global biases seem to now have a higher magnitude and latitude-dependent biases have been observed. Before the data could be assimilated in a Reanalysis system the high magnitude of bias would need to be understood and corrected if possible, and a bias correction scheme developed for the orbital-dependent bias.

This report demonstrates how short-range forecasts from NWP systems can be used to evaluate new satellite instruments, and identify potential issues which need to be corrected. If there are issues such as orbital-dependent biases they can be identified with just 24 hours of data, particularly for temperature sounding channels where the short-range forecasts are particularly accurate. (However, a longer time series of statistics would be needed to further analyse such biases and develop a correction.) It is important to compare statistics wherever possible to similar channels of other instruments since this can confirm whether the observed biases are due to the instrument or whether they might be due to radiative transfer errors or systematic forecast errors. For example the comparison to AMSR-2 for the MTVZA-GY imager channels allowed us to confirm that the ascending/descending bias is not due to forecast model error. In the future there will be more launches of the Meteor-M satellite series, and future MTVZA-GY instruments could be evaluated using a similar method to the one presented in this study.

Acknowledgements

Chiara and Cristina Lupu (ECMWF) are kindly acknowledged for their help in developing the offline method for calculating the ECMWF O - B values for MTVZA-GY.

References

W. Bell, B. Candy, N. Atkinson, F. Hilton, N. Baker, N. Bormann, G. Kelly, M. Kazumori, W.F. Campbell, and S.D. Swadley. The assimilation of SSMIS radiances in numerical weather prediction models. *IEEE Trans. Geoscience. Rem. Sensing.*, 46:884 – 900, 2008.

A. Booton, W. Bell, and N. Atkinson. An improved bias correction for SSMIS. *Proceedings of the International TOVS Study Conference (ITSC) 19, Jeju Island, South Korea*, 2014.

N. Bormann, A. Fouilloux, and W. Bell. Evaluation and assimilation of ATMS data in the ECMWF system. *J. Geophys. Res.*, 118:12970 – 12980, 2013.

A.J. Geer, P. Bauer, and N. Bormann. Solar biases in microwave imager observations assimilated at ECMWF. *IEEE Trans. Geoscience. Rem. Sensing.*, 48:2660–2669, 2010.

J. Hocking, P. Rayer, D. Rundle, R. Saunders, M. Matricardi, A. Geer, P. Brunel, and J. Vidot. RTTOV v11 users guide. pages available online: https://www.nwpsaf.eu/site/software/rttov/rttov–v12/, 2015.

J. Hocking, P. Rayer, D. Rundle, R. Saunders, M. Matricardi, A. Geer, P. Brunel, and J. Vidot. RTTOV v12 users guide. pages available online: https://www.nwpsaf.eu/site/software/rttov/rttov–v12/, 2017.

M. Kazumori and S. English. Use of the ocean surface wind direction signal in microwave radiance assimilation. *Quart. J. Roy. Meteorol. Soc.*, 141:1354 – 1375, 2015.

H. Lawrence, F. Carminati, W. Bell, N. Bormann, S. Newman, N. Atkinson, A. Geer, S. Migliorini, Q. Lu, and K. Chen. An evaluation of FY-3C MWRI and assessment of the long-term quality of FY-3C MWHS-2 at ECMWF and the Met Office. *ECMWF Tech. Memo.*, 798, 2017.

Q. Lu, W. Bell, P. Bauer, N. Bormann, and C. Peubey. Characterizing the FY-3A microwave temperature sounder using the ECMWF model. *J. Atmos. Oceanice Technol.*, 28:1373–1389, 2011.

Q. Lu, H. Lawrence, N. Bormann, S. English, K. Lean, N. Atkinson, W. Bell, and F. Carminati. An evaluation of FY-3C satellite data quality at ECMWF and the Met Office. *ECMWF Tech. Memo.*, 767, 2015.

C. Lupu and A. J. Geer. Operational implementation of RTTOV-11 in the IFS. *ECMWF Tech. Memo.*, 748, 2015.

L. M. Mitnik, V. P. Kuleshov, M. L. Mitnik, A.M. Streltsov, G. M. Cherniavsky, and I. V. Cherny. Microwave scanner-sounder MTVZA-GY on new russian meteorological satellite Meteor-M no. 2: modeling, calibration and measurements. *Proceedings, Microrad conference*, 2016.

S. Newman, W. Bell, and K. Salonen. Calibration/validation study of AMSR-2 on GCOM-W1. *GAIA-CLIM Deliverable 4.2, available online*, 2016. URL `http://www.gaia-clim.eu`.

R. Saunders, M. Matricardi, and P. Brunel. An improved fast radiative transfer model for assimilation of satellite radiance observations. *Q. J. R. Meteorol. Soc.*, 125:1407–1425, 1999.

R. Saunders, J. Hocking, D. Rundle, P. Rayer, S. Havemann, M. Matricardi, A. Geer, C. Lupu, P. Brunel, and J. Vidot. RTTOV-12 science and validation report. page available online: https://www.nwpsaf.eu/site/software/rttov/documentation/, 2017.

S. Uspensky, E. Kramchaninova, A. Uspensky, P. Poli, S. English, and C. Lupu. An initial assessment of microwave imager/sounder MTVZA-GY data from Meteor-M N2 satellite. *Presentation, International TOVS Study Conference (ITSC) XX*, 2015.

GAIA-CLIM Report

Gap Analysis for Integrated Atmospheric ECV CLImate Monitoring:

Assessment of reference data in global assimilation systems and characterisation of key satellite datasets

Assessment of new satellite missions

Calibration/validation study of GPM GMI

Work Package	WP 4
Deliverable	Assessment of new satellite missions
Title	Calibration/validation study of GPM GMI
Nature	R
Dissemination	PU
Beneficiary	Met Office
Date	20/12/2017
Status	2.0
Authors	Fabien Carminati, Jacqueline Goddard, Heather Lawrence, Stuart Newman
Reviewers	Peter Thorne, Anna Mikalsen
Contacts	fabien.carminati@metoffice.gov.uk
URL	http://www.gaia-clim.eu/

Abstract

The Global Precipitation Measurement (GPM) Microwave Imager (GMI) is a state-of-the-art conical-scanning radiometer. A dual calibration system confers to the instrument the highest standards of radiometric calibration and stability achieved to date. This study evaluates GMI observations in the framework of the Gap Analysis for Integrated Atmospheric ECV CLImate Monitoring (GAIA-CLIM) project using Numerical Weather Prediction (NWP) models from the Met Office and the European Centre for Medium-Range Weather Forecasts (ECMWF) as a reference comparator. Departures between short-range forecasts and GMI observations are found to be stable over the period of study and smaller than for other instruments of comparable radiometric capabilities. Observed biases are principally related to areas that remain poorly simulated by NWP models due to high wind speed, low surface temperature, and cloud residuals.

Contents

1. Introduction

The production of Climate Data Records (CDR) (Yang et al., 2016) and reanalyses (Uppala et al., 2005) relies to a large extent upon the large spatial coverage and frequent revisit rate offered by space observations. The characterisation of satellite data quality is therefore a fundamental activity required to take place upstream prior to the production of such records. The assessment of instrument biases has traditionally been carried out using: a) in situ or remote ground based and airborne measurements from existing networks or dedicated validation campaigns, and b) satellite-to-satellite match ups in intercomparison studies. In situ measurements often offer relative high vertical resolution compared to satellite measurements. However, very few have traceable uncertainty to International Standards (SI), and these tend to be sparse in space and time. Satellite intercomparisons can offer an improved coverage with respect to in situ networks, but currently lack SI traceability.

Within the framework of the Gap Analysis for Integrated Atmospheric ECV CLImate Monitoring (GAIA-CLIM) project, we investigate the use of Numerical Weather Prediction (NWP) models as a complementary assessment technique to characterise satellite biases (Saunders et al., 2013). The spatially and temporally continuous representation of the atmosphere in NWP models offers a key advantage with respect to conventional networks. The evolution of the model is constrained by the knowledge of the physics and dynamics of the atmosphere making model fields physically consistent, while the Data Assimilation (DA) systems, driving NWP models, provide a high-quality homogeneous framework where model errors are minimized by the ingestion of a large volume of observations (satellite, balloon-borne, airborne, ground-based, buoys ...).

NWP-based satellite assessment has become a mature technique over the past decade, successfully employed for the validation of sounding instruments (e.g. Bell et al., 2008; Lu et al., 2011a, 2011b; Zou et al., 2011; Doherty et al., 2012; Bormann et al., 2013; Lu and Bell, 2014). The validation of imager instruments (mainly sensitive to the surface) is, however, more challenging due to gaps in the representation of surface (or near-surface) properties in NWP models. Nevertheless, studies conducted as part of GAIA-CLIM have demonstrated the soundness of this approach for the Advanced Microwave Scanning Radiometer 2 (AMSR-2) (Newman et al., 2015) and the MicroWave Radiation Imager (MWRI) (Lawrence et al., 2017). NWP field uncertainty characterisation and traceability to SI, accounting for geophysical variables uncertainty mapped to radiance space, uncertainty in radiative transfer modelling, scale mismatches, interpolations, and cloud-screening residual, are also being evaluated as part of GAIA-CLIM, though these are not yet available at the time of writing.

In this study, we evaluate the Global Precipitation Measurement (GPM) Microwave Imager (GMI), a state-of-the-art conical-scanning radiometer, which, according to the U.S. National Aeronautics and Space Administration (NASA), has achieved the highest standards of radiometric calibration and stability to date. NWP models from the UK Met Office and the European Centre for Medium-Range Weather Forecasts (ECMWF) are used for this evaluation.

The remainder of the report is structured as follows. Section 2 introduces the instrument, the two models, and describes the data processing. Section 3 presents the results from the comparison between observations and simulated observations from the models. Section 4 concludes.

2. Data and data processing

GPM GMI

The GPM mission is the result of an international effort led by the NASA and the Japan Aerospace and Exploration Agency (JAXA) built on the Tropical Rainfall Measuring Mission (TRMM) legacy. The platform was launched on February 27, 2014, in a 65° inclination orbit at 407 km mean altitude. It carries a Ka/Ku-band Dual-frequency Precipitation Radar (DPR) and a multifrequency microwave radiometer, GMI. The combination of passive radiometric measurements and high-resolution precipitation profiles (from the radar backscatter) provides a reference standard for precipitation measurements from Space, whilst improving climate, weather, and hydro-meteorological science (Hou et al., 2014).

GMI, commissioned by the NASA Goddard Space Flight Centre and built by Ball Aerospace & Technologies Corporation, was turned on on March 1, 2014, and has been operating since March 4, 2014. It is composed of a 1.22 m deployable antenna, rotating at 32 rotations-per-minute, and a receiver subsystem, rotating with the reflector, composed of six feed horns (from left to right in the sense of rotation: 36, 89, 18/23, 183, 166, and 10 GHz). Note that given the direction of rotation and the disposition of the feed arrays, the radiometric information first reaches the 36 GHz feed horn, while the 10 GHz horn comes last, 0.06 seconds and 12° later (see figure 2 and 3 by Draper et al., 2015a). This configuration gives the instrument nine imaging channels in the 10-89 GHz spectral range and four sounding channels at 166-183 GHz (table 1).

Table 1: (from left to right) GMI channel number, centre frequency, polarization, bandwidth, off-nadir angle, Earth-incidence angle (EIA), swath width, beam width, instantaneous field of view (IFOV), effective field of view (EFOV), on-orbit NEDT.

Channel	Centre frequency (GHz)	Polarization	Bandwidth (MHz)	Off-nadir angle (deg)	EIA (deg)	Swath width (km)	Beam width (deg)	IFOV (km)	EFOV (km)	On-orbit NEDT (K)
1	10.65	V	96.5	48.43	52.74	931	1.72	19x32	20x32	0.77
2	10.65	H	94.7	48.42	52.73	931	1.72	19x32	20x32	0.78
3	18.7	V	193	48.44	52.76	931	0.98	11x18	12x18	0.63
4	18.7	H	194	48.44	52.76	931	0.98	11x18	12x18	0.60
5	23.8	V	367	48.45	52.76	931	0.85	10x16	10x16	0.51
6	36.64	V	697	48.47	52.79	933	0.82	9x15	10x15	0.41
7	36.64	H	707	48.47	52.79	933	0.82	9x15	10x15	0.42
8	89	V	5470	48.46	52.78	932	0.38	4x7	6x7	0.32
9	89	H	5516	48.46	52.78	932	0.38	4x7	6x7	0.31
10	166	V	3138	45.28	49.11	826	0.38	4x6	6x6	0.70
11	166	H	3202	45.28	49.11	826	0.37	4x6	6x6	0.65
12	183.31±3	V	2964	45.28	49.11	826	0.37	4x5	6x5	0.56
13	183.31±7	V	3748	45.28	49.11	826	0.37	4x5	6x5	0.47

The antenna provides Earth observations by the way of a conical scan around the platform track with nominal off-nadir incidence angles of 48.5° for the low frequency (10-89 GHz) and 45.3° for the high frequency (166-183 GHz). The corresponding footprint resolution ranges from 25 km at the lowest

frequency for a total swath of 931 km (±25 km) to 6 km at the highest with a total swath of 826 km (±22 km).

The instrument radiometric capability potentially provides useful information on precipitation, surface temperature, wind speed, water vapour and cloud liquid water column, and surface snow and ice cover.

GMI is designed to be the GPM calibration standard and benefits from a number of enhancements over its heritage from the TRMM Microwave Imager (TMI) and similar instruments. The primary on board calibration system is common to most microwave imagers and consists of an external hot load and a cold sky reflector. On each 1.875-second scan, the antenna, which benefits from an improved low emissivity coating, receives radiometric measurements from three sectors composed of 1) 152°of Earth view, 2) the hot load view, designed to avoid solar intrusions and thermal gradients, and 3) the cold sky view. GMI was however, at the time of launch, the first of its kind to resort to a dual calibration system through the addition of internal noise diodes. The noise diodes, which provide additional calibration points from 10 to 37 GHz, are used to estimate the receiver non-linearity and transient anomalies in the primary calibration system.

A comprehensive overview of GMI characteristics is provided by Draper et al. (2015a) and summarized in table 1, while calibration and radiometric performances have been reported by Newell et al. (2014; 2015), Draper et al. (2015a; 2015b; 2015c), and Wentz and Draper (2016). Wentz and Draper (2016) report in particular on the absolute calibration that they estimated be approximately 0.25 K in root mean square (rms).

A preliminary NWP-based assessment using the ECMWF model has been carried out and reported by Lean et al. (2017). The authors analysed 10 days of super-obbed GMI observations from August 2016 compared to simulated ECMWF all-sky brightness temperatures. Both observed and simulated brightness temperature were cloud-screened using the normalised polarisation difference as described in the *Data selection* section. They concluded that GMI mean global bias lies with ±0.8 K for all but the 89 GHz channels. The larger bias (~1.5 K) at 89 GHz was suggested to be due to model errors. In this study, we build on the work of Lean et al. (2017) and investigate further GMI biases with a double model comparison (Met Office and ECMWF) and over longer periods.

Met Office NWP
The Met Office data assimilation system operates as follows.

Satellite raw data are transmitted to and processed by ground stations where they are transformed into calibrated, geolocated brightness temperatures (Tb) and sent for onward distribution. The data received by the Met Office are ingested in the Meteorological Data Base system (MetDB) and archived in the Managed Archive Storage System (MASS). Note that GMI data are archived since July 2015.

The assimilation in operation of satellite data is a two-step process.

First, a low resolution N768L70 (~25 km at mid-latitudes, 70 levels from surface to 80 km) one-dimensional variational analysis (1D-Var) is performed to derive physical parameters used in the subsequent main variational process. The fast radiative transfer model RTTOV version 11 (Saunders

et al., 2012) is used to map model variables in the observation spectral domain. Surface emissivity (oceanic) is calculated using FASTEM 6 (Kazumori and English, 2015). The first guess, or background, used for the retrieval is the 6-hour forecast (T+6) of the previous assimilation cycle, interpolated at the observation location and time. Quality controls (QC), including cloud screening, are conducted as part of the 1D-Var analysis. The 4D-Var data assimilation system at the Met Office (see below) uses a clear-sky scheme, therefore radiances that are significantly affected by clouds are discarded.

Second, the data go through the main assimilation system, a hybrid incremental 4D-Var assimilation model of resolution N320L70 (~40 km at mid-latitudes, 70 levels from surface to 80 km) and 6-hour time window (Courtier et al., 1994; Rawlins et al., 2007). The forecast model used in operations has a resolution of N1280L70 (~10 km at mid-latitudes, 70 levels). A variational bias correction of satellite brightness temperatures as described by Auligné et al. (2007) is in place since 2016.

Because GMI is not yet assimilated operationally at the Met Office, data have to be treated in an off-line processing mode. This also means that the model background used for the comparison is fully independent from the observations. The off-line routine proceeds in four steps: 1) GMI observations are retrieved from the MetDB, 2) the background from the operational system is retried from MASS, 3) the N768L70 1D-Var is performed, and 4) collocated brightness temperatures and retrieved quantities are saved in netCDF format. No bias correction is applied to GMI observations and data are neither thinned nor super-obbed. QC applied to GMI observations are described in the *Data selection* section.

ECMWF NWP
The ECMWF data assimilation system operates as follows.

The data are received by ECMWF in BUFR and are pre-screened and then transformed into the Observation Data Base (ODB) format. After processing and calculation of first guess departures, they are archived in the Meteorological Archival and Retrieval System (MARS).

At ECMWF, a hybrid incremental 4D-Var assimilation model is used with a 12-hour assimilation window. The forecast model used in operations has a resolution of Tco1279 (~9 km, 137 levels). For the purpose of monitoring GMI data, the experiments have a reduced resolution of Tco 399 (~25 km, 137 levels).

Since 2009, ECMWF has assimilated microwave imager radiances in all-sky conditions over ocean. The GMI microwave imager channels have been assimilated in all-sky conditions operationally since August 2015, and this gives beneficial reductions in short and medium-range forecast errors of around 0.5% (Peter Lean, Alan Geer and Katrin Lonitz, 2017). ECMWF's all-sky assimilation stream is described in more detail by Bauer et al. (2010), Geer and Bauer (2010), and Geer et al. (2017). All observations, whether clear, cloud, or precipitating, are expected to be assimilated, and the observation-equivalent is simulated using a scattering-capable radiative transfer model RTTOV-SCATT (Bauer et al., 2006), currently at RTTOV version 11.3.

The data from GMI imager channels (1-9) and sounding channels (10-13) come in two separate data streams and the individual fields of view within each swath are not exactly co-located. Each stream undergoes pre-screening of the BUFR code and super-obbing onto a T255-equivalent reduced Gaussian model grid (and this has half the grid points removed in a diamond pattern, for additional thinning). Super-obbing the imager and sounding channels to the same grid collocates them to a common resolution and is intended to be representative of the spatial scales of the forecast model; this is a circle of approximately 60 km radius. Standard ECMWF quality control is applied, including a check on the size of the normalised first guess departures, and also variational quality control (VarQC, Järvinen and Unden,1997). The first guess, or background, used for the retrieval is the short-range forecast of the previous assimilation cycle, interpolated at the observation location and time. A variational bias correction of satellite brightness temperatures as described by Dee (2004) is used in assimilation.

As with other microwave imaging channels at ECMWF, channels 1-9 are only used over ocean and within 60° of the equator, to avoid areas where surface emissivity modelling errors can become too large. Channels 10-13 are currently used only over ice-free oceans. The imager channels and lowest peaking 183 GHz channel also have the Cold-Air Outbreak screening applied (Lonitz and Geer, 2015). This removes observations in areas of cold-air outbreak where there is a known model problem: the ECMWF model produces too much ice cloud instead of super-cooled liquid water cloud in these areas.

For consistency with the Met Office dataset, the super-obbing has been turned off for the set of experiments monitoring the imaging channels, but had to be left on for technical reasons for the set of experiments monitoring the sounding channels. Note that in those experiments, GMI was monitored passively and uncorrected (i.e. not assimilated in the background).

Data selection
Three periods of study have been selected for the assessment of GMI observations:

1) August 1, 2016 to September 30, 2016 (hereafter referred to as summer);
2) December 1, 2016 to January 31, 2017 (hereafter referred to as winter); and
3) March 6, 2017 to March 20, 2017 (hereafter referred to as post-cal).

The post-cal period is aimed to evaluate a calibration change[1] affecting GMI L1C data as of March 4, 2017.

For the assessment to be conducted in the most reliable way, the following screening has been applied to the data:

In order to avoid regions where our confidence in model surface emissivity is low, only data over ocean, at latitudes between 60° north and 60° south, and with a retrieved skin temperature greater than 274 K, are used.

---

[1] http://www.eorc.jaxa.jp/GPM/doc/product/ReleaseNote/GMI_and_partner_L1C_V5.pdf

Similarly, because our confidence in simulated cloud emissivity is low (or not available), only clear-sky data are used. To identify clear-sky data, RTTOV-SCATT is used in an off-line routine to express the cloud amount in both observation and background as a function of the normalized polarization at 37 GHz as described by Lawrence et al. (2017) and summarized below:

$$C_{37}^{obs} = 1 - \frac{Tb_V^{obs} - Tb_H^{obs}}{Tb_{V,clear}^{back} - Tb_{H,clear}^{back}} \qquad (1)$$

$$C_{37}^{back} = 1 - \frac{Tb_V^{back} - Tb_H^{back}}{Tb_{V,clear}^{back} - Tb_{H,clear}^{back}} \qquad (1)$$

where C^{obs}_{37} and C^{back}_{37} are the observation and background cloud amount, respectively. Tb^{obs}_V and Tb^{obs}_H are GMI brightness temperatures at 37 GHz with vertical and horizontal polarization (hereafter V and H-pol), respectively. Tb^{back}_V and Tb^{back}_H are model V and H-pol brightness temperatures simulated with RTTOV-SCATT (i.e. including the scattering due to clouds in the radiation transfer equation). $Tb^{back}_{V,clear}$ and $Tb^{back}_{H,clear}$ are model V and H-pol brightness temperatures simulated with RTTOV (i.e. ignoring the scattering effect, also referred to as clear-sky). Note that the hydrometeors included in the calculation of C^{back}_{37} are cloud liquid water, cloud ice, snow and rain at ECMWF, but only cloud liquid water and cloud ice at the Met Office. Consistently with Lawrence et al. (2017), only data with $C^{obs}_{37} < 0.05$ and $C^{back}_{37} < 0.05$ are used.

In the ECMWF system, GMI observations from the sounding channels (10-13) are super-obbed with imaging channels, therefore the 37 GHz-based cloud screening can be applied to observations for all channels. While the 37 GHz-based cloud screening is also applied at the Met Office to the data from the imaging channels, this is not possible for data from the sounding channels as no super-obbing is used (different geolocations and footprints).

Met Office sounding channels are screened for cloud as follows: a) a departure-based test is conducted on channel 10 (166 GHz V-pol), i.e. if the difference between observed and simulated brightness temperature is greater than 2.1 K the observation is marked as cloudy and rejected, b) a cirrus cost test, i.e. a cost function using channel 10, 12, and, 13, in combination with an imposed threshold on the magnitude of the departure in channel 13 as described by Doherty et al. (2012), and c) a threshold on the retrieved liquid water path, i.e. observations with more than 0.01 kg.m^{-2} are rejected.

In addition to the common screening described above, general NWP centre-dependent QC are checked as follows: data from ECMWF with QC flags 2, 3, 4, 5, 7, 8, 12, 13, 14, 15, 16, 17, or 21 are rejected and data from the Met Office with QC flags 2, 5, 6, 14, 17, 18, 19, 21, 22, 25, 26, 27, 28, 29, or 31 are rejected. The detail of ECMWF and Met Office QC flags is given in appendix A, table A.1.

Finally, only data with GMI quality flag (as distributed by data provider) set to zero are used (see appendix A, table A.2).

3. Results

The data presented in this section shows the comparison between GMI observations and simulated observations from the T+6 NWP forecasts (i.e. the background) from the Met Office clear-sky scheme,

the ECMWF clear-sky scheme, and the ECMWF all-sky scheme. This is referred to as background departure to observation. All data have been filtered as detailed in the previous section.

Global departures

Global background departures have been calculated for the three periods of study for each GMI channel. Because different cloud screens are applied to GMI sounding channels (10-13) processed at the Met Office, imaging and sounding channels are analysed independently.

Figure 1 shows the background departures from the Met Office and both clear and all-sky ECMWF along with the 1σ standard deviation in the departures for GMI imaging channels. The figure also shows the difference between Met Office and ECMWF backgrounds, and between GMI observations as processed at each centre (left panels). Both departures and standard deviations are very similar over the three periods of study, meaning that the instrument has been stable at least between August 2016 and March 2017. The departures from the Met Office and ECMWF all-sky vary in a consistent way and agree within ±1 K (except for channel 7 that differs by 1 K and, to a lesser extent, channel 5 that differs by 0.5 K). Departures from ECMWF clear-sky present a different pattern. They vary from -0.5 K to 4 K, generally increasing with the frequency.

The discrepancies in departures obtained for ECMWF clear and all-sky, and in comparison with the Met Office, pose two main questions:

1) What causes the differences between ECMWF clear and all-sky departures?
2) Why does the Met Office clear-sky match better the ECMWF all-sky rather than the clear-sky?

The left panel of figure 1 shows that ECMWF clear-sky background is cold biased with respect to ECMWF all-sky (difference between solid and dashed lines) by up to 3 K. This has been traced back to a residual effect of clouds not removed by the 37 GHz-based cloud screening. Off-line calculations have shown that the difference in ECMWF clear and all-sky background is reduced to less than 0.01 K when all background cloud proxies are used in the cloud clearing process (rain water path, cloud liquid water path, cloud ice water path, and snow water path less than 0.0001 kg.m^{-2}). Those proxies are not available at the Met Office and therefore cannot be use for consistency in the intercomparison.
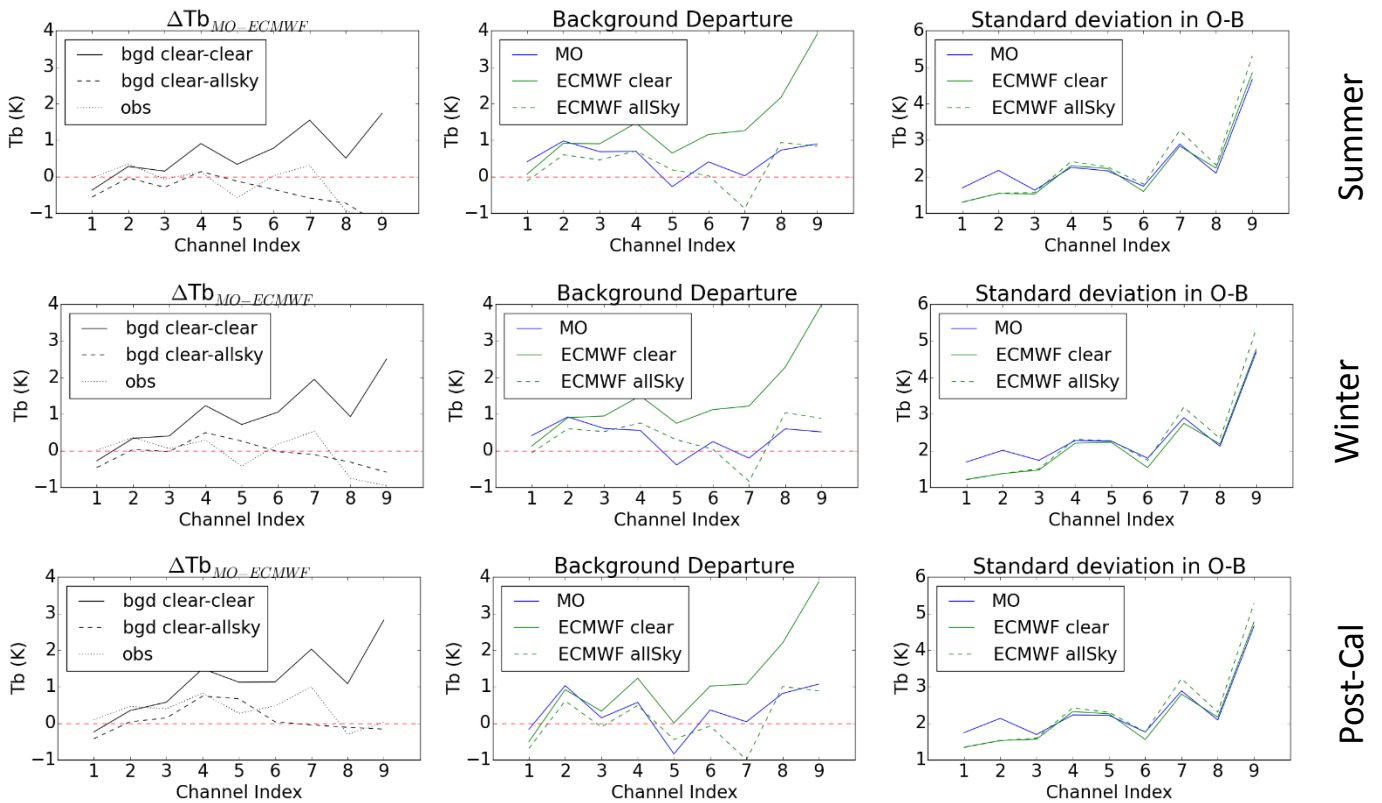
Figure 1: (Top left) mean difference between the simulated brightness temperature from the Met Office clear scheme and ECMWF clear scheme (solid line), the Met Office clear scheme and ECMWF all-sky scheme (dashed line), and GMI observed brightness temperature processed at the Met Office and at ECMWF (dotted line). (Top middle) mean background departure (i.e. observation - background) for the Met Office dataset (blue), ECMWF clear-sky dataset (solid green), and ECMWF all-sky dataset (dashed green). (Top right) 1σ standard deviation in the background departure from the Met Office (blue), ECMWF clear-sky (green), and ECMWF all-sky (dashed green) datasets. All three panels show GMI imaging channels for the summer period. (Middle) Same as top but for winter period. (Bottom) Same as top but for Post-Cal period.

The greater agreement between Met Office clear-sky and ECMWF all-sky departures compared to ECMWF clear-sky can be explained by the use of the RTTOV model. ECMWF clear-sky background is calculated with RTTOV (i.e. clear-sky radiative transfer ignoring scattering) ignoring all cloud proxies, while ECMWF all-sky background is calculated with RTTOV-SCATT (accounting for the scattering) and includes the effect of cloud liquid water, cloud ice, snow, and rain. At the Met Office, the 1D-Var analysis (used to calculate GMI background departures) uses RTTOV with cloud liquid water (i.e. ignoring scattering but adding the contribution of cloud liquid water to the calculation of the optical depth affecting the absorption). The impact of accounting for the cloud liquid water path in RTTOV is shown in figure 2. With a cloud amount threshold similar to that used for the screening of GMI data (0.05, blue line), the simulated brightness temperatures accounting for the cloud liquid water are up to 3.5 K larger than when cloud liquid water is ignored, which is consistent with ECMWF clear-sky background. Figure 2 also shows that this effect can be mitigated with a tighter cloud amount threshold (difference reduced to 1.5 K in channel 9 with threshold of 0.02).

The standard deviation in departures, shown in the right panels, figure 1, is consistent for both centres. It increases with the frequency from 1-2 K up to 5 K as the higher frequency channels are more sensitive to clouds. However, the standard deviation for the Met Office in channel 1 and 2 is 0.5 K larger than for ECMWF. This is largely due to the large footprint of the 10 GHz channels, which overlaps with land surface near coastlines and result in higher departures and variability in the Met Office datasets. The effect is not present in the ECMWF datasets where coastlines are screened out by one of the QC checks.

Finally, it worth noting that GMI mean departures (ignoring ECMWF clear-sky) at 10.64 GHz V and H-pol, 18.7 GHz V-pol, 23.8 GHz V-pol, and 36.64 GHz V and H-pol are significantly smaller (by one order of magnitude in most cases) than those reported by Lawrence et al. (2017) for MWRI and AMSR-2, as shown in table 2. At 18.7 GHz H-pol and 89 GHz V and H-pol, GMI departures are similar to those of MWRI, but still significantly smaller than AMSR-2 departures.

Figure 3 is similar to figure 1 but for GMI sounding channels. The sounding channels, although more sensitive to scattering (e.g. caused by ice cloud), are peaking higher in the atmosphere than imaging channels and therefore are less affected by unscreened low-level liquid clouds. For this reason, the background departures for ECMWF clear and all-sky are more consistent (less than 0.5 K difference) than the imaging channels. The background and observations processed at the Met Office are cold biased with respect to the ECMWF equivalents. This is partly caused by the different (less efficient) cloud screening applied to the sounding channels at the Met Office.

Table 2: MWRI and AMSR-2 background departure (K) and 1σ standard deviation (K), shown between brackets, estimated by Lawrence et al. (2017) for the September 2016 time period compared to GMI's (summer period) at GMI frequency. The smallest departures are green shaded. Note that only statistics for ECMWF all-sky is shown.

	Background departure (K) and 1σ standard deviation (K)								
	10.65GHz V-pol	10.65GHz H-pol	18.7GHz V-pol	18.7GHz H-pol	23.8GHz V-pol	36.64GHz V-pol	36.64GHz H-pol	89GHz V-pol	89GHz H-pol
MWRI (MetO.)	-6.45 (3.86)	-6.77 (6.44)	-1.80 (2.31)	-0.56 (3.58)	-2.36 (2.19)	-2.44 (1.79)	-1.99 (2.73)	0.24 (1.95)	0.95 (4.09)
MWRI (ECMWF)	-6.97 (2.84)	-7.32 (3.88)	-2.12 (1.76)	-0.68 (2.63)	-1.86 (2.10)	-2.90 (1.64)	-2.77 (2.83)	0.38 (2.13)	0.70 (4.66)
AMSR-2 (ECMWF)	0.56 (2.03)	2.41 (3.09)	0.84 (2.33)	3.02 (3.23)	3.25 (1.29)	4.33 (1.43)	2.04 (2.43)	3.39 (2.05)	4.27 (3.67)
GMI (MetO.)	0.41 (1.69)	0.97 (2.17)	0.68 (1.63)	0.69 (2.25)	-0.27 (2.16)	0.40 (1.74)	0.02 (2.89)	0.72 (2.09)	0.89 (4.66)
GMI (ECMWF)	-0.11 (1.29)	0.60 (1.54)	0.46 (1.56)	0.70 (2.41)	0.18 (2.27)	0.03 (1.79)	-0.86 (3.26)	0.93 (2.32)	0.83 (5.30)

The discrepancies between background departures from Met Office and ECMWF mainly result from the super-obbing applied to ECMWF data. Nevertheless, at 183 GHz (channels 12 and 13) GMI departures are within ±1.1 K, two-time smaller than the departures reported by Lawrence at al. (2017) for the Microwave Humidity Sounder 2 (MWHS-2) at equivalent frequencies.
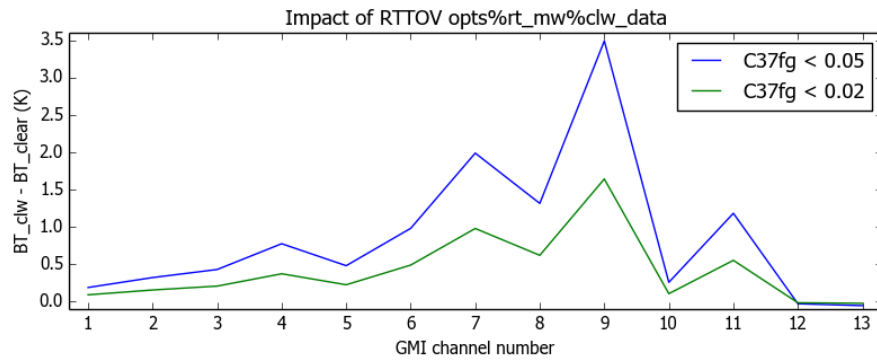

Figure 2: Difference in simulated brightness temperature using RTTOV with and without cloud liquid water path (clw) in the Met Office background at GMI channel frequencies. The blue (green) line shows data with a cloud amount less than 0.05 (0.02).

Like for the imaging channels, the departures and the standard deviations are stable over the three periods of study. Minor differences in the Post-Cal dataset may be due to the calibration change, but this is not easily disentangled from seasonal and sampling variations.
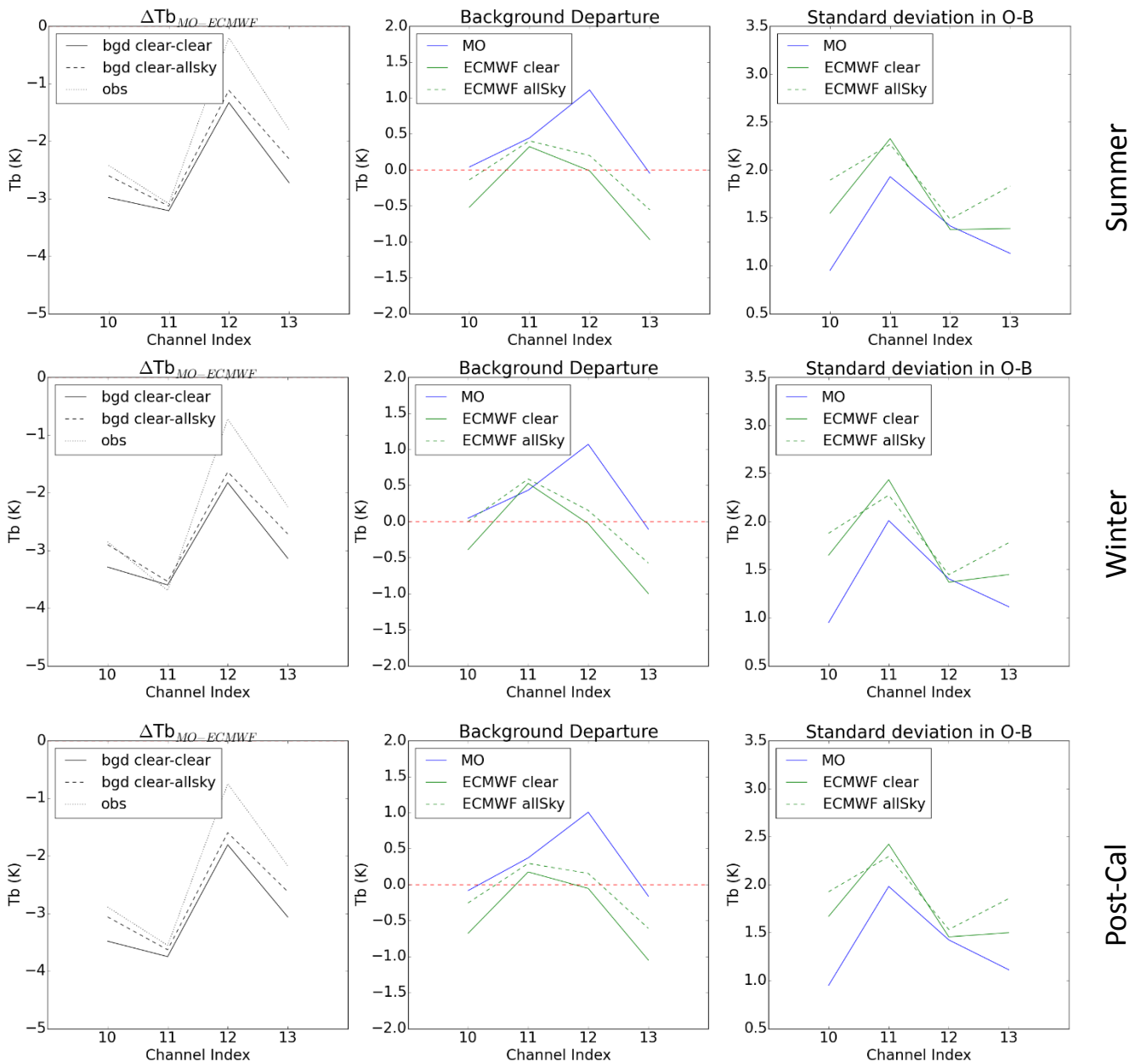
Figure 3: Same as figure 1 but for GMI sounding channels.

Geographical bias distribution

Global mean biases give a good indication of the instrument performances but may hide regional patterns at synoptic and/or meso scales. Background departures from the Met Office and ECMWF clear and all-sky have been averaged in 1°x1° (latitude x longitude) bins for each of the GMI channel and each period of study. Anomaly maps, expressed as the bin value minus the global mean, complement the analysis.
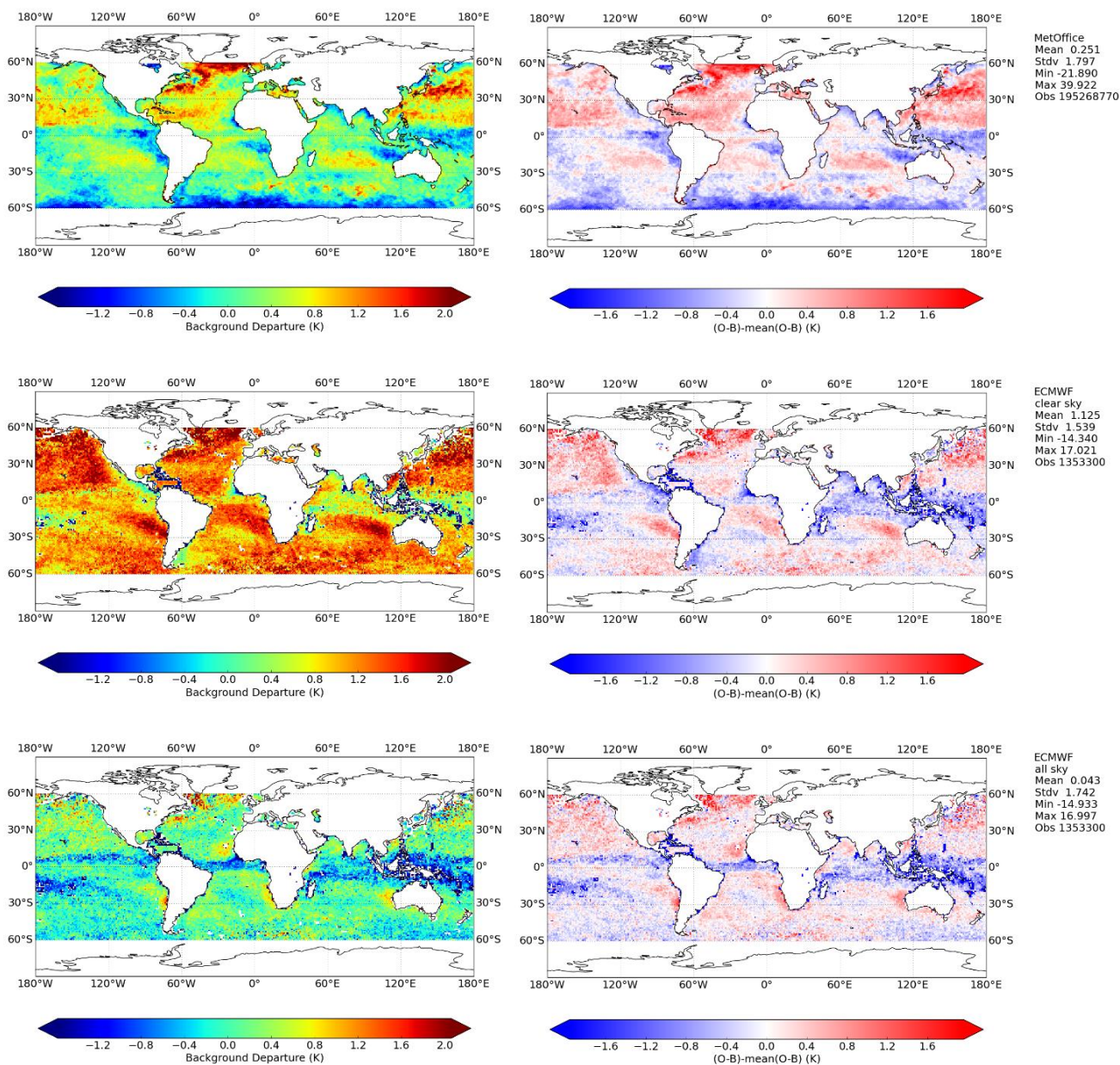
Figure 4: (Top left) Background departure (observation minus background, or O-B) averaged in 1° latitude x1° longitude bins for GMI channel 6 (36.64 GHZ V-pol) and the Met Office clear-sky background over the winter period. (Top right) GMI channel 6 background departure anomaly expressed as (O-B) – mean(O-B), winter period. (Middle) Same as top but for ECMWF clear-sky dataset. (Bottom) Same as top but for ECMWF all-sky dataset.

Figure 4 illustrates GMI channel 6 (36.64 GHz V-pol) departure and anomaly maps averaged over the winter period. The Met Office dataset mean global departure is 0.251 K but the northern Atlantic and northern Pacific present local biases of over 2 K, while a negative bias of the same order of magnitude is visible over the Austral Ocean. The negative biases in the Austral Ocean as well as patches over the western coasts of South America, Africa, Australia, and over the Western Pacific, are likely a residual effect of low level and shallow clouds, which have not been successfully screened. The positive biases

at high northern latitudes are consistent with strong winter winds known to cause biases in the forward model due to systematic errors in the surface emissivity model FASTEM. A similar bias is observed in the Austral Ocean during the summer period (see appendix B). Figure 5 further explores the relationship between background departures, wind speed, and latitude for GMI channel 6. Departures, slightly negative at low wind speed, become positive at wind speed around 10 m.s^{-1} (at high latitudes) and increase up to over 4 K. This confirms the predominant role of high-speed wind on this high latitude winter bias. Note that most V-pol channels present this bi-polar bias, while H-pol channels are mostly positively biased (not shown). Only channel 9 presents a reversed pattern with positive bias at low wind speed and negative bias at high wind speed (see appendix C). It is worth noting that the wind-speed dependent bias may be mitigated with the implementation of a background departure-based quality control triggered when the wind-speed reaches a defined threshold (e.g. 7 m.s^{-1} as suggested by Newman et al., 2015). Further analyses, beyond the scope of this study, may however be required to estimate the best configuration for such a quality control.
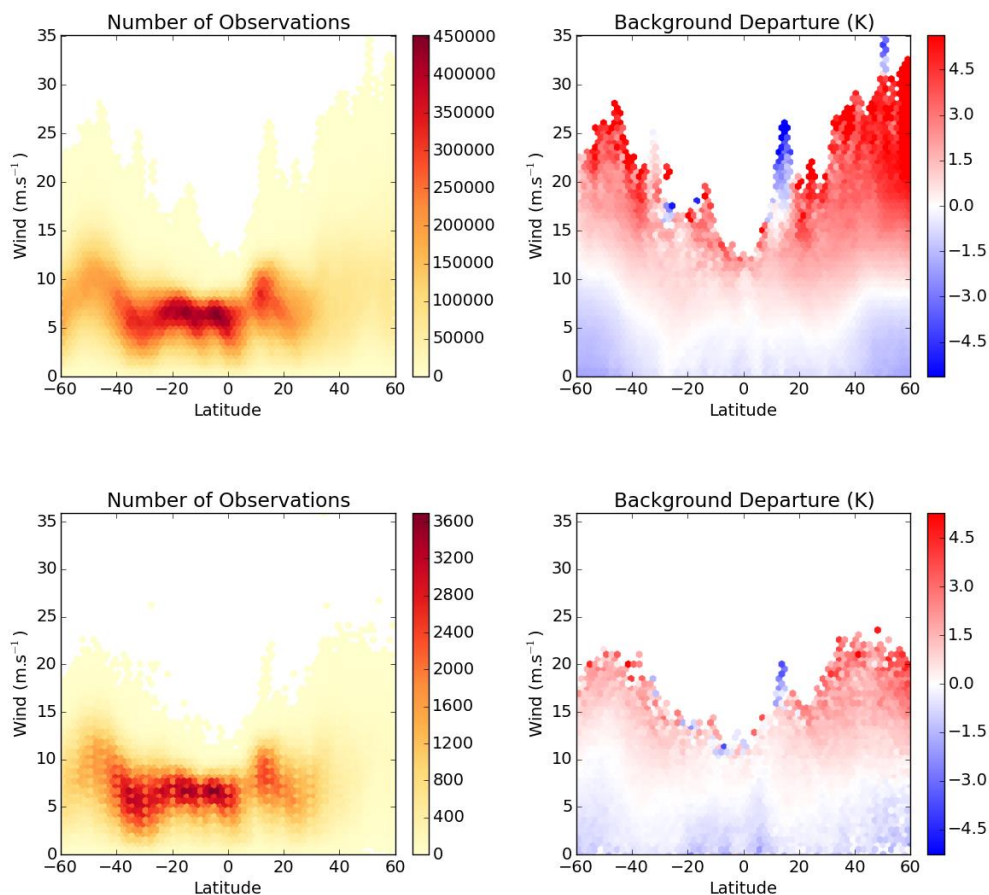
Figure 5: (Top) Number of observations (left) and background departure (right) for GMI channel 6 (36.64 GHz V-pol), Met Office dataset, winter period, expressed as a function of latitude and wind speed. (Bottom) Same as top but for ECMWF all-sky dataset.

In spite of different global mean values for ECMWF all-sky and clear-sky departures (1.125 K for clear-sky and 0.043 K for all-sky), both show the northernmost positive bias associated with high wind speed. The tropics and the southern hemisphere differs however from the Met Office maps. Most notably, the Inter Tropical Convergence Zone (ITCZ) stands out with a negative bias, while the Austral Ocean does not present the marked bias seen in the Met Office dataset. This might reflect a greater sensitivity to deep convective clouds, typically found in the ITCZ, and a better handling of low and shallow clouds in the ECMWF model (or better cloud-screening due to the cold air out break screen).

ECMWF all-sky Summer

Ch3
(18.7GHz V-pol)

Ch4
(18.7GHz H-pol)
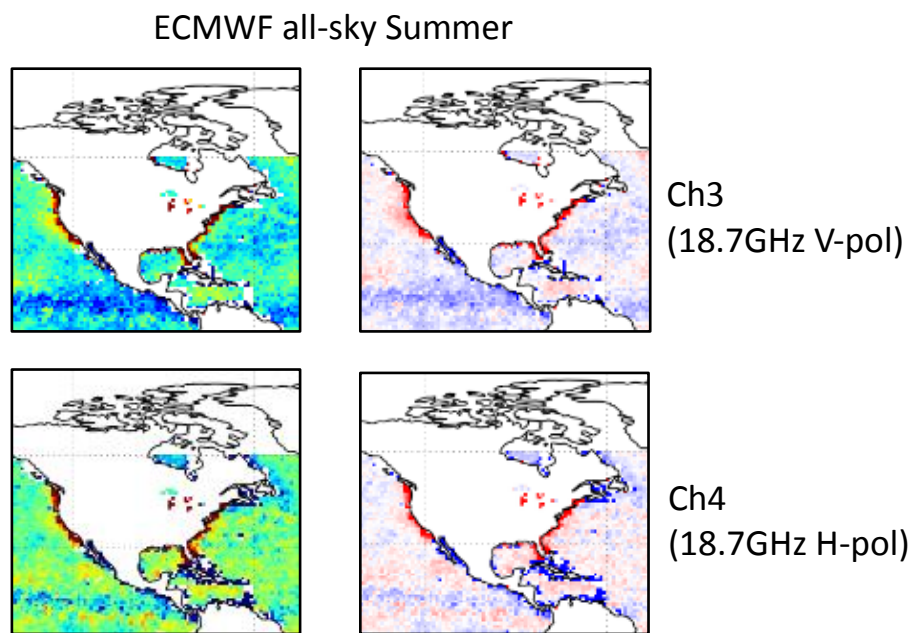
Figure 6: (Top) Cropped section of figure B.3 (appendix B) of GMI channel 3 background departures (left) and anomalies (right) from ECMWF all-sky dataset, summer period, centred on the USA. (Bottom) Same as top but for channel 4.

Departure and anomaly maps of GMI channels 1-5 and 7-9, during winter and summer, are shown in appendix B. It is worth noting the presence of atypically large positive departures (positive anomaly) along the coastline of the United States of America main land for GMI channels 3 and 4 (18.7 GHz V and H-pol, respectively). The phenomenon is observed for all periods and all datasets. Figure 6 shows a cropped section of GMI channels 3 and 4 departure and anomaly maps (see appendix B for whole figures) centred over the USA during the summer period. The coastline bias is over 3 K and is spatially limited to the US territory, i.e. not extending over Canadian or Mexican coastlines. This bias can be traced back to Radio Frequency Interferences (RFI) from the US television provider DirectTV whose satellites operate at frequencies between 18.3 and 18.8 GHz as described by Zou et al. (2014). It is however surprising that the GMI RFI detection algorithm[2] (triggering QC flag 2, table A.2, appendix A) is not capturing this relatively strong signal. In comparison, the RFI detection algorithm performs well in the 10.65 GHz channels that are also prone to RFI, mainly in Europe as reported by Lawrence et al. (2017), but apparently unaffected (e.g. figures B.1 and B.2, appendix B).

---

[2] https://pmm.nasa.gov/sites/default/files/document_files/GPMGMIL1BATBDV2.3.pdf

Sounding channels present larger differences in terms of mean departures than the imaging channels, principally due to the different way they are processed (super-obbing and cloud screen), but their anomalies are generally consistent (i.e. negative anomalies in the tropics, positive at mid- and high-latitudes at 166 GHz and the opposite at 183 GHz, see appendix B). One exception is seen in channel 13 (183±7 GHz). As shown in figure 7, ECMWF all-sky dataset presents large positive biases in regions where the residual effect of cloud is potentially large (e.g. high latitudes, maritime continent), while the other two datasets are mostly negatively biased over the same areas. At 183±7 GHz frequency, channel 13 should not be highly sensitive to the surface parameters (even though the small water burden at high latitude causes the channel to peak at lower level than in the tropics) such as wind and surface temperature or type. The residual effect from clouds in the lowermost troposphere is the most likely source for this bias. This is further corroborated by the absence of such biases at 183±3 GHz (channel 12, see appendix B) that is mostly sensitive to the mid-troposphere.

Negative departures such as those observed in the Met Office and ECMWF clear-sky datasets results from observations brightness temperatures appearing colder than the background due to the presence of unscreened clouds (the top of the cloud having a lower brightness temperature than the cloud-free atmosphere). On the contrary, the positive bias seen in the ECMWF all-sky dataset suggests an overestimation of the cloud amount in the lowermost troposphere leading to a colder background (as seen in figure 3).

Note that a 2°x2° average is used for sounding channels to cope with the lesser number of observations in ECMWF datasets due to the super-obbing.
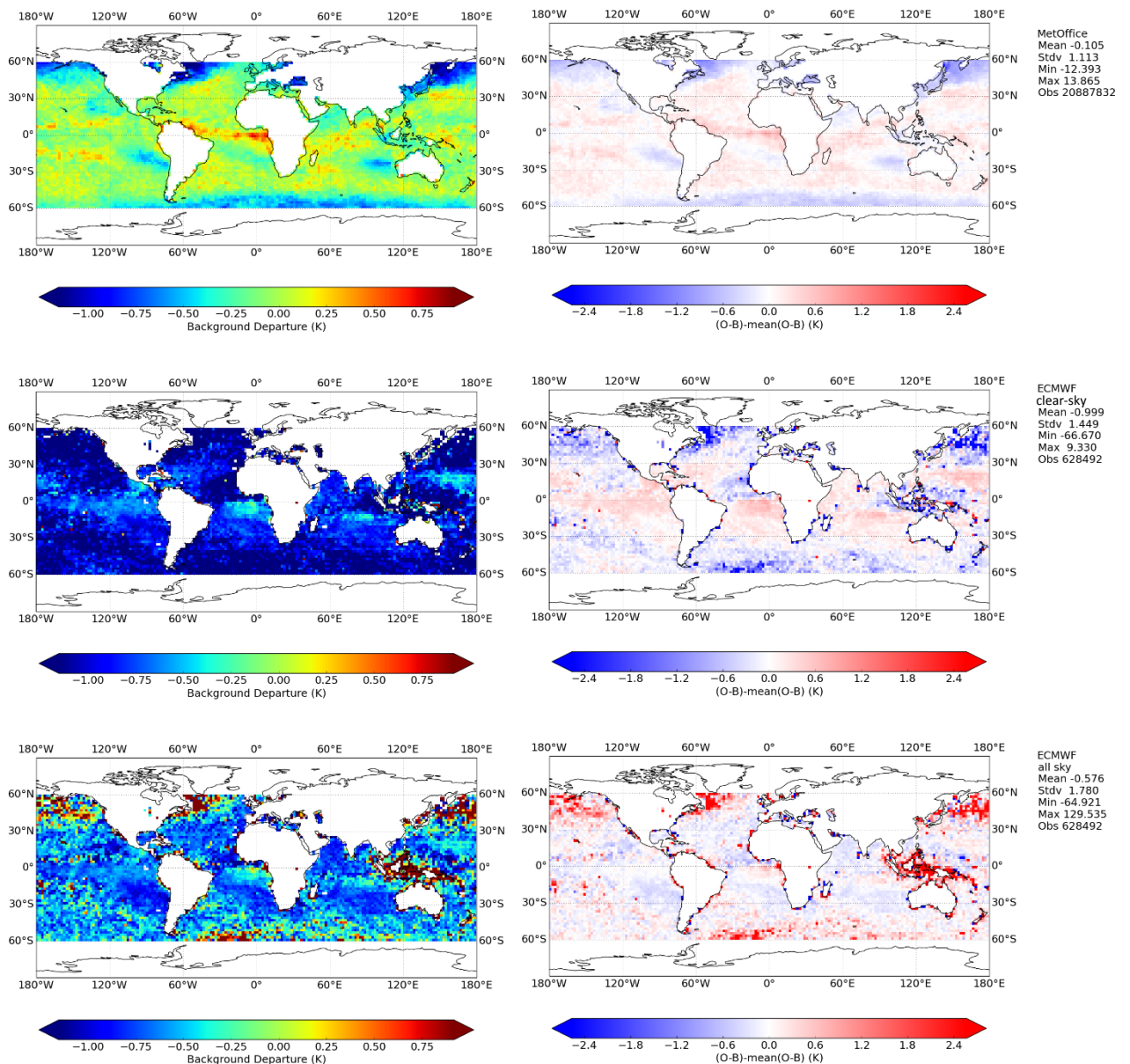
Figure 7: Same as figure 4 but for channel 13, with 2°x2° bins.

Orbital angle dependency

Historical microwave imagers such as the Special Sensor Microwave Imager Sounder (SSMIS), TMI or the more recent MWRI, are known to suffer orbital angle dependent bias (Bell et al., 2008; Geer et al., 2010; Lawrence et al., 2017). During the half orbit exposed to the sun, the thermal emission coming from part(s) of the instrument heated by sunlight contaminates the information transmitted by the main reflector. Sunlight may also interfere with the primary calibration via direct or indirect contamination of the hot load.

GMI has been designed with a protected hot load and a low emissivity coating to address those issues. An effective way to assess the observations against such bias is to compare the background departure from the half orbit on the daytime side of the Earth and that of the half orbit on the night-time side of the Earth. This has been estimated using the local time at the observation location during the post-cal period (6-20 March 2017). Over that period, daytime observations, defined as observations obtained between 08:00 and 15:00 local time, correspond to the descending orbit and night-time observations, defined as observations obtained between 20:00 and 03:00 local time, correspond to the ascending orbit. The mean difference ascending minus descending (or night minus day) is shown in figure 8. Note that only the ECMWF clear-sky dataset has been used. Both datasets consistently confirm the absence of a significant ascending/descending bias, with double differences ranging from -0.1 to 0.25 K and within the 0.25 K rms calibration uncertainty estimated by Wentz and Draper (2016). In comparison, MWRI ascending-descending departure difference (~2 K) found by Lawrence et al. (2017) is one order of magnitude larger than that of GMI.
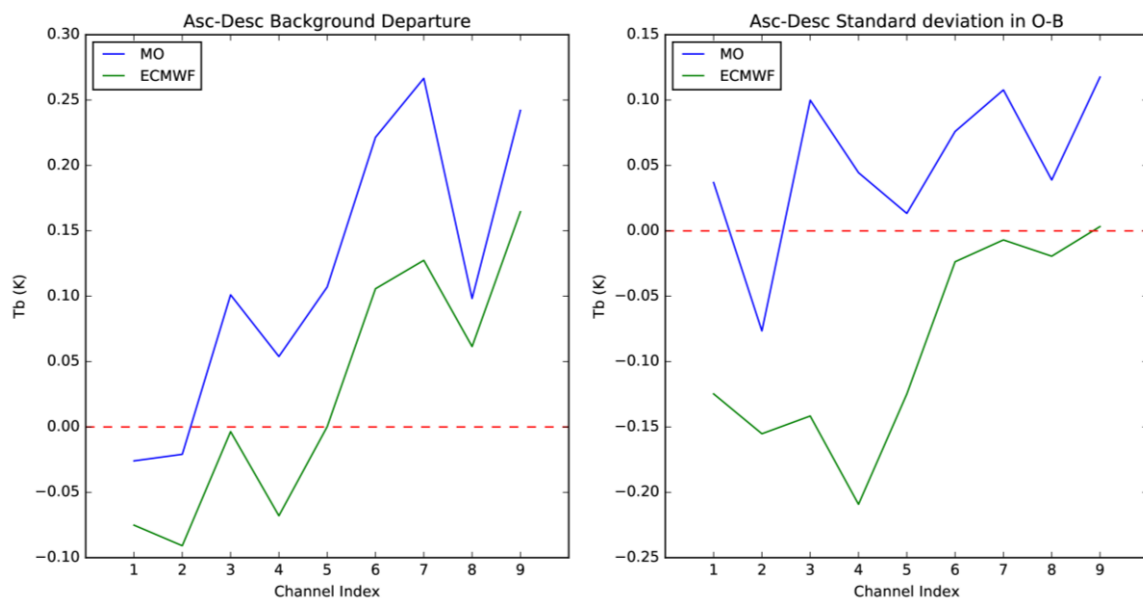
Figure 8: (Left) difference between the background departure from GMI ascending and descending nodes for the Met Office dataset (blue) and ECMWF clear-sky (green), post-cal period. (Right) 1σ standard deviation in the ascending – descending departures.

4. Conclusion

This work carries on the GAIA-CLIM initiative to demonstrate the benefits of NWP systems for the assessment of satellite observations. In this study, GPM GMI, a state-of-the-art conical microwave imager, is evaluated with the help of NWP systems from the Met Office and ECMWF.

To achieve the best degree of accuracy and consistency in this analysis, careful processing and data selection have been carried out. The numerical simulations have been conducted at similar resolution with, as far as possible, similar versions of the radiative transfer model and emissivity model. Data

have been selected over ocean in clear-sky conditions in order to avoid known model deficiencies. Periods of study have been selected so as to consider both boreal summer and wintertime (two months each) and a shorter more recent period (two weeks in March 2017) aimed to evaluate the impact of a planned operational calibration change.

The analysis of global mean observation minus model background difference shows little variations in the statistics between seasons, further testifying to GMI stability (at least over the periods of study). No impact from the calibration change have been detected or clearly disentangled from natural variability. The global mean departures range within ±1 K in the imaging channels (10-89 GHz) in the Met Office and ECMWF with all-sky scheme datasets, but reach up to 4 K in the ECMWF with clear-sky scheme dataset at high frequency. The difference between the two ECMWF schemes have been attributed to the residual effect of undetected clouds. The global mean departures in the sounding channels (166-183 GHz) vary between -1 and 1.1 K, noting that the consistency of the comparison is not as high as in the sounding channels (due to processing differences in the two centres). If the global statistics for GMI sounding channels are of the same order as well-established instruments of similar sounding capability, the sounding channels appear to be the less biased (better calibrated) compared to other imagers such as MWRI and AMSR-2.

The evaluation of a daytime and night-time subset of departures suggests the absence of an orbital angle dependent bias, which is commonly found in the observations of this kind of instrument.

Local biases stand out when a geographical-based approach is considered. Nevertheless, the nature of those biases suggests model-related origins (e.g. high surface wind) or deficiencies in the data screening (e.g. cloud residual effect). This suggests that NWP-related systematic uncertainties are the main limiting factor for the validation of high calibration standard microwave imager instruments and tighter quality controls may be required for the assessment of future instruments with similar mission requirements.

Reference

Auligné, T., McNally, A.P. and Dee, D.P., 2007. Adaptive bias correction for satellite data in a numerical weather prediction system. Quarterly Journal of the Royal Meteorological Society, 133(624), pp.631-642.

Bauer, P., Geer, A. J., Lopez, P. and Salmond, D., 2010. Direct 4D-Var assimilation of all-sky radiances: Part I. Implementation. Quart. J. Roy. Meteorol. Soc. 136, 1868–1885

Bauer, P., Lopez, P., Salmond, D. and Geer, A. J., 2006. Assimilation of cloud and precipitation affected microwave radiances. ECMWF Tech. Memo., 502. https://www.ecmwf.int/sites/default/files/elibrary/2006/7998-assimilation-cloud-and-precipitation-affected-microwave-radiances.pdf

Bell, W., Candy, B., Atkinson, N., Hilton, F., Baker, N., Bormann, N., Kelly, G., Kazumori, M., Campbell, W.F., and Swadley, S.D., 2008. The assimilation of SSMIS radiances in numerical weather prediction models. IEEE Trans. Geoscience. Rem. Sensing., 46:884 – 900.

Bormann, N., Fouilloux, A. and Bell, W., 2013. Evaluation and assimilation of ATMS data in the ECMWF system. Journal of Geophysical Research: Atmospheres, 118(23).

Courtier P, Thepaut J-N, Hollingsworth A. 1994. A strategy for operational implementation of 4D-Var, using an incremental approach. Q. J. R. Meteorol. Soc. 120: 1367–1387.

Dee, D. , 2004. Variational bias correction of radiance data in the ECMWF system. In ECMWF workshop proceedings: Assimilation of high spectral resolution sounders in NWP, pp. 97–112. ECMWF, Reading, UK. https://www.ecmwf.int/sites/default/files/elibrary/2004/8930-variational-bias-correction-radiance-data-ecmwf-system.pdf

Doherty, A., Atkinson, N., Bell, W., Candy, B., Keogh, S. and Cooper, C., 2012. An initial assessment of data from the Advanced Technology Microwave Sounder. Forecasting Research Technical Report, no. 569, available from https://library.metoffice.gov.uk

Draper, D.W., Newell, D.A., Wentz, F.J., Krimchansky, S. and Skofronick-Jackson, G.M., 2015a.The global precipitation measurement (GPM) microwave imager (GMI): Instrument overview and early on-orbit performance. IEEE Journal of Selected Topics in Applied Earth Observations and Remote Sensing, 8(7), pp.3452-3462.

Draper, D.W., Newell, D.A., McKague, D.S. and Piepmeier, J.R., 2015b. Assessing calibration stability using the Global Precipitation Measurement (GPM) Microwave Imager (GMI) noise diodes. IEEE Journal of Selected Topics in Applied Earth Observations and Remote Sensing, 8(9), pp.4239-4247.

Draper, D., Remund, Q., Newell, D. and Krimchansky, S., 2015c. A comparison OF GPM Microwave Imager (GMI) high frequency channel brightness temperatures to the Advanced Technology Microwave Sounder (ATMS). In Geoscience and Remote Sensing Symposium (IGARSS), 2015 IEEE International (pp. 5146-5149). IEEE.

Geer, A.J., Bauer, P. and Bormann, N., 2010. Solar biases in microwave imager observations assimilated at ECMWF. IEEE Trans. Geoscience. Rem. Sensing., 48:2660–2669.

Geer, A. J. and Bauer P., 2010. Enhanced use of all-sky microwave observations sensitive to water vapour, cloud and precipitation. Published simultaneously as ECMWF Technical Memoranda 620 and ECMWF/EUMETSAT fellowship reports 20. https://www.ecmwf.int/sites/default/files/elibrary/2010/9506-enhanced-use-all-sky-microwave-observations-sensitive-water-vapour-cloud-and-precipitation.pdf

Geer, A. J., Baordo, F., Befort, K., Bormann, N., English, S., Kazumori, M., Lawrence, H., Lean, P. and Lupu, C., 2017. The growing impact of satellite observations sensitive to humidity, cloud and precipitation. Quart. J. Roy. Meteorol. Soc.

Hou, A.Y., Kakar, R.K., Neeck, S., Azarbarzin, A.A., Kummerow, C.D., Kojima, M., Oki, R., Nakamura, K. and Iguchi, T., 2014. The global precipitation measurement mission. Bulletin of the American Meteorological Society, 95(5), pp.701-722.

Jarvinen, H. and P. Unden, 1997. Observation screening and background quality control in the ECMWF 3D-Var data assimilation system. ECMWF Tech. Memo., 236. https://www.ecmwf.int/sites/default/files/elibrary/1997/10352-observation-screening-and-background-quality-control-ecmwf-3d-var-data-assimilation-system.pdf

Kazumori, M. and English, S. J., 2015. Use of the ocean surface wind direction signal in microwave radiance assimilation. Q.J.R. Meteorol. Soc., 141: 1354–1375.

Lawrence, H., Carminati, F., Bell, W., Bormann, N., Newman, S., Atkinson, N., Geer, A., Migliorini, S., 2017. An Evaluation of FY-3C MWRI and Assessment of the long-term quality of FY-3C MWHS-2 at ECMWF and the Met Office, ECMWF Tech. Memo., 798.

Lean P. and Geer A. and Lonitz K., 2017. Assimilation of Global Precipitation Mission (GPM) Microwave Imager (GMI) in all-sky conditions. ECMWF Tech. Memo., 799. https://www.ecmwf.int/sites/default/files/elibrary/2017/17174-assimilation-global-precipitation-mission-gpm-microwave-imager-gmi-all-sky-conditions.pdf

Lonitz, K. and Geer, A., 2015. New screening of cold-air outbreak regions used in 4D-Var all-sky assimilation. European Centre for Medium-Range Weather Forecasts. https://www.ecmwf.int/sites/default/files/elibrary/2015/10777-new-screening-cold-air-outbreak-regions-used-4d-var-all-sky-assimilation.pdf

Lu, Q., Bell, W., Bauer, P., Bormann, N. and Peubey, C., 2011a. Characterizing the FY-3A microwave temperature sounder using the ECMWF model. Journal of Atmospheric and Oceanic Technology, 28(11), pp.1373-1389.

Lu, Q., Bell, W., Bauer, P., Bormann, N. and Peubey, C., 2011b. An evaluation of FY-3A satellite data for numerical weather prediction. Quarterly Journal of the Royal Meteorological Society, 137(658), pp.1298-1311.

Lu, Q. and Bell, W., 2014. Characterising channel center frequencies in AMSU-A and MSU microwave sounding instruments, J. Atmos. Oceanic Tech.

Newell, D., Draper, D., Figgins, D., Berdanier, B., Kubitschek, M., Holshouser, D., Sexton, A., Krimchansky, S., Wentz, F. and Meissner, T., 2014. GPM microwave imager key performance and calibration results. In Geoscience and Remote Sensing Symposium (IGARSS), IEEE International, pp. 3754-3757.

Newman, S., Bell, W., and Salonen, K., 2015. Calibration/validation study of AMSR-2 on GCOM-W1. GAIA-CLIM Deliverable 4.2, http://www.gaia-clim.eu

Rawlins F, Ballard SP, Bovis KJ, Clayton AM, Li D, Inverarity GW, Lorenc AC, Payne TJ., 2007. The Met Office Global Four-Dimensional Variational Data Assimilation Scheme. Q. J. R. Meteorol. Soc. 133: 347–362.

Saunders, R., Hocking, J., Rayer, P., Matricardi, M., Geer, A., Bormann, N., Brunel, P., Karbou, F. and Aires, F., 2012. RTTOV-11 science and validation report. NWPSAF-MO-TV-032, v1. 11. EUMETSAT NWP-SAF.

Saunders, R.W., Blackmore, T.A., Candy, B., Francis, P.N. and Hewison, T.J., 2013. Monitoring satellite radiance biases using NWP models. IEEE Transactions on Geoscience and Remote Sensing, 51(3), pp.1124-1138.

Uppala, S.M., Kållberg, P.W., Simmons, A.J., Andrae, U., Bechtold, V.D., Fiorino, M., Gibson, J.K., Haseler, J., Hernandez, A., Kelly, G.A. and Li, X., 2005. The ERA-40 re-analysis. Quarterly Journal of the Royal Meteorological Society, 131(612), pp.2961-3012.

Wentz, F.J. and Draper, D., 2016. On-orbit absolute calibration of the global precipitation measurement microwave imager. Journal of Atmospheric and Oceanic Technology, 33(7), pp.1393-1412.

Yang, W., John, V.O., Zhao, X., Lu, H. and Knapp, K.R., 2016. Satellite Climate Data Records: Development, Applications, and Societal Benefits. Remote Sensing, 8(4), p.331.

Zou, X., Wang, X., Weng, F. and Li, G., 2011. Assessments of Chinese FengYun Microwave Temperature Sounder (MWTS) measurements for weather and climate applications. Journal of Atmospheric and Oceanic Technology, 28(10), pp.1206-1227.

Zou, X., Tian, X. and Weng, F., 2014. Detection of television frequency interference with satellite microwave imager observations over oceans. Journal of Atmospheric and Oceanic Technology, 31(12), pp.2759-2776.

Appendix A

Table A.1: Data quality control flags used at the Met Office (left) and ECMWF (right)

	Met Office QC flags	ECMWF QC flags
0	Thinned out	Observation active if only this bit set
1	Result of cloud cost test	Observed TB out of bounds
2	Conflicting surface types	Negative Q in model profile
3	High land spot	Surface T < 274K in model
4	Cost threshold based on these channels	Land in model
5	No retrieval for this observation	Sea ice in model
6	Error in forward model	Latitude outside bounds
7	Result of cirrus cost test	No observation for this grid point
8	Result of 183GHz SI test	Orography over land
9	Flag slow converging observation	Sea ice in observations (AMSU-A only)
10	None	Passive monitoring
11	Result of HIRS20 cloud test	Observation rejected if any important channels are bad
12	Any failure	No grid point for this obs
13	None	Winter cold sectors: model has too little water cloud
14	Unwanted surface type	RTTOV-SCATT is too responsive to snow at higher frequency
15	ATOVPP pre-processor flag	Observation value is missing
16	ATOVPP scan flag	Once-per-gridpoint R/T paradigm failure
17	Error identifying which channels are present	Winter cold sectors: model has too much water cloud
18	Error in forward model	Last timestep
19	Retrieval BT outside acceptable limits	None
20	Surface elevation too high	Ocean in model
21	Retrieval failed to converge	Lsm in model not in agreement with and/ocean assimilation
22	Background outside acceptable limits	Land emissivity retrieval failure
23	Bad predictors for bias correction	SI over land too big
24	Background BT outside acceptable limits	Transmittance screening over land
25	No channels for retrieval	Sea-ice surface type being assimilated
26	Bad predictors for extrapolation	None
27	Raw BT outside acceptable limits	None
28	Inusable scan position	None
29	Unidentified Flying Observation	None
30	Masked or filtered out	None
31	Outside of model area/time domain	None

Table A.2: GMI quality flag, value and description, as distributed by data provider.

| GMI quality flag	
Flag value	description
0	Good data
1	Possible sun glint
2	Possible radio-frequency interference
3	Degraded geolocation data
4	Data corrected for warm load intrusion
5	Scan blanking on
6	Data is missing from file or unreadable
7	Unphysical brightness temperature
8	Error in geolocation data
9	Data missing in one channel
10	Data missing in multiple channels
11	Lat/lon values are out of range
12	Non-normal status modes
13	Distance to corresponding if pixel > 7 km
14	Reserved
15	Missing value (no quality information available)

Appendix B
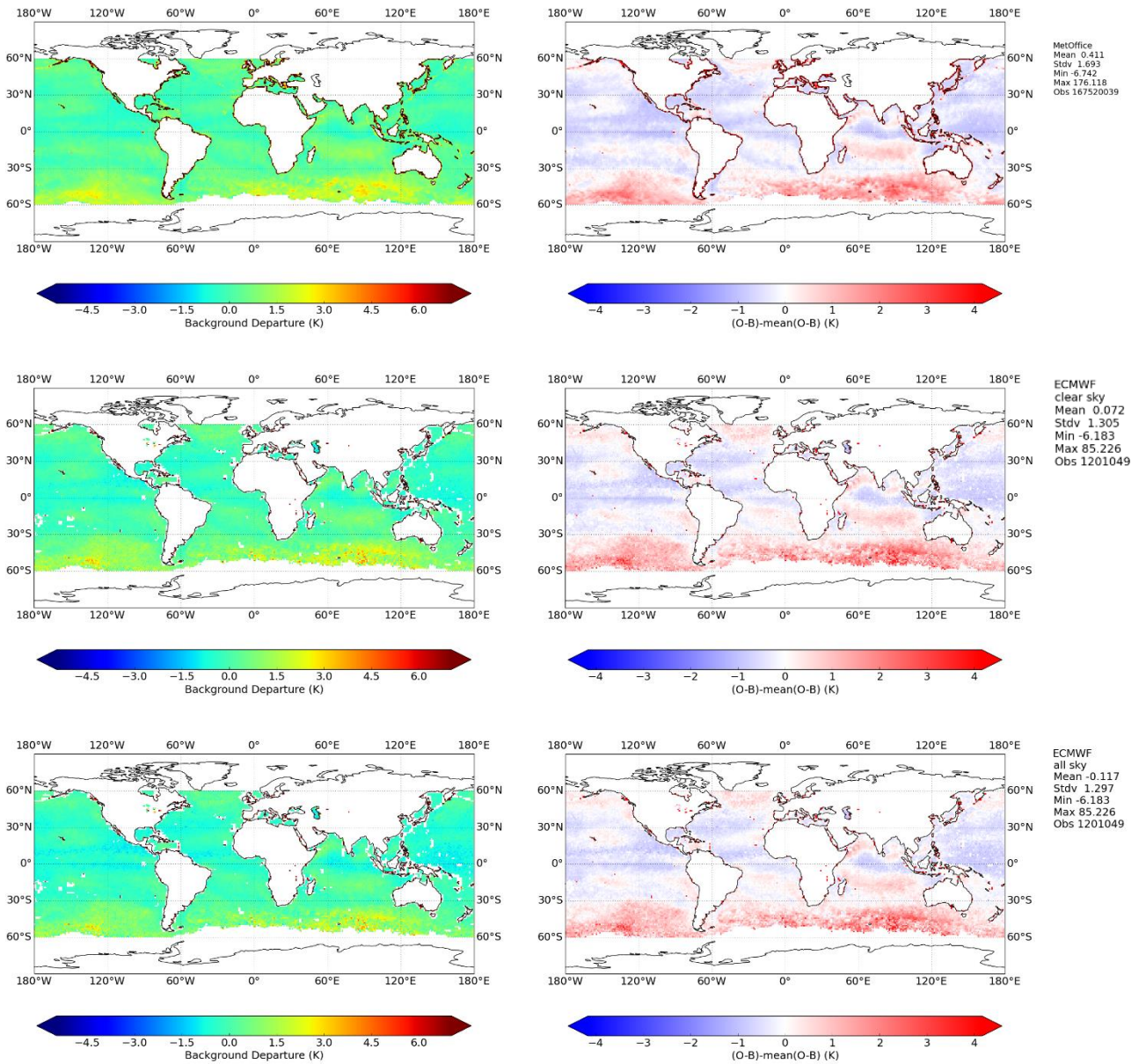
Figure B.1: Same as figure 4 but for GMI channel 1, summer.
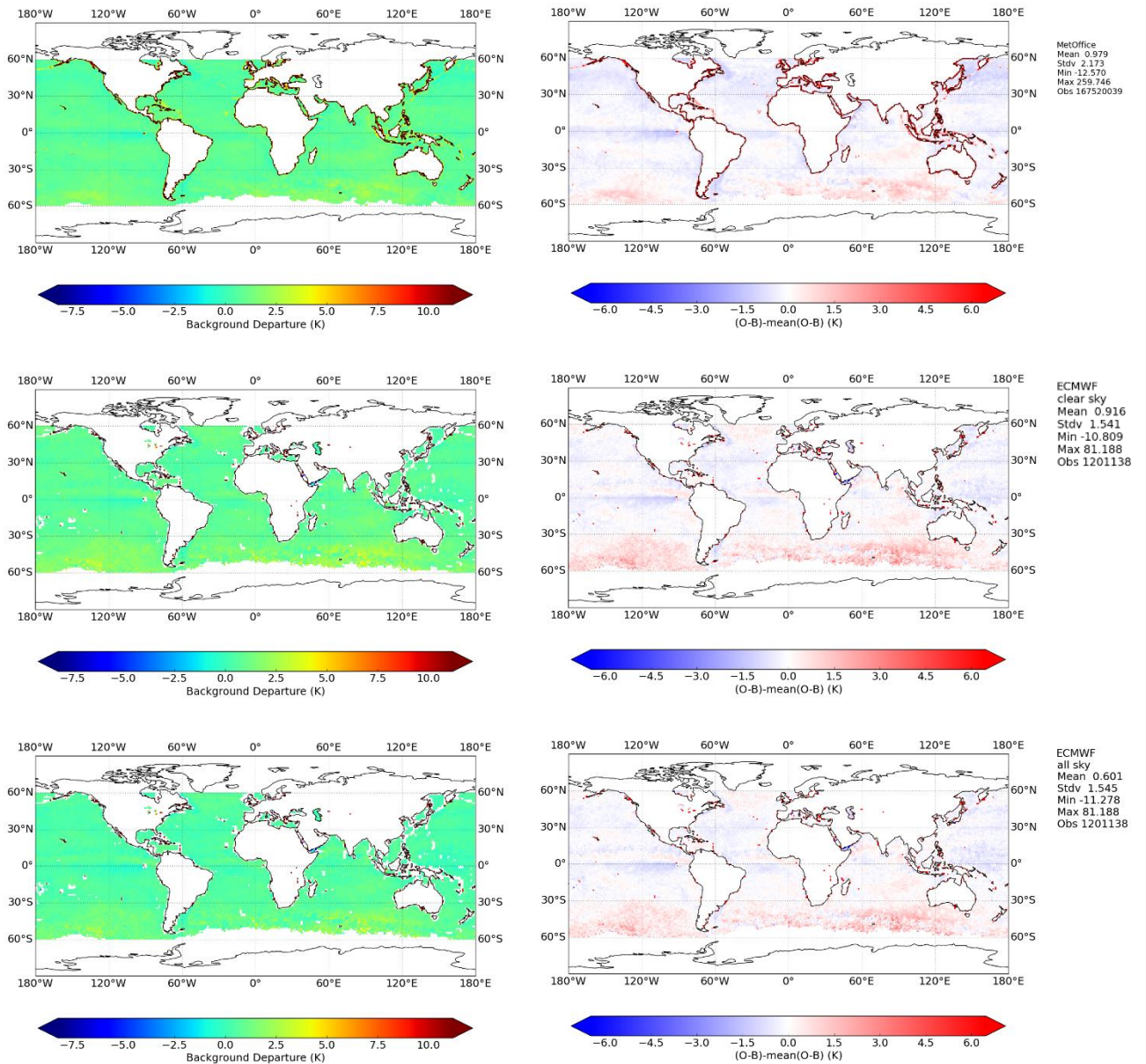
Figure B.2: Same as figure 4 but for GMI channel 2, summer.
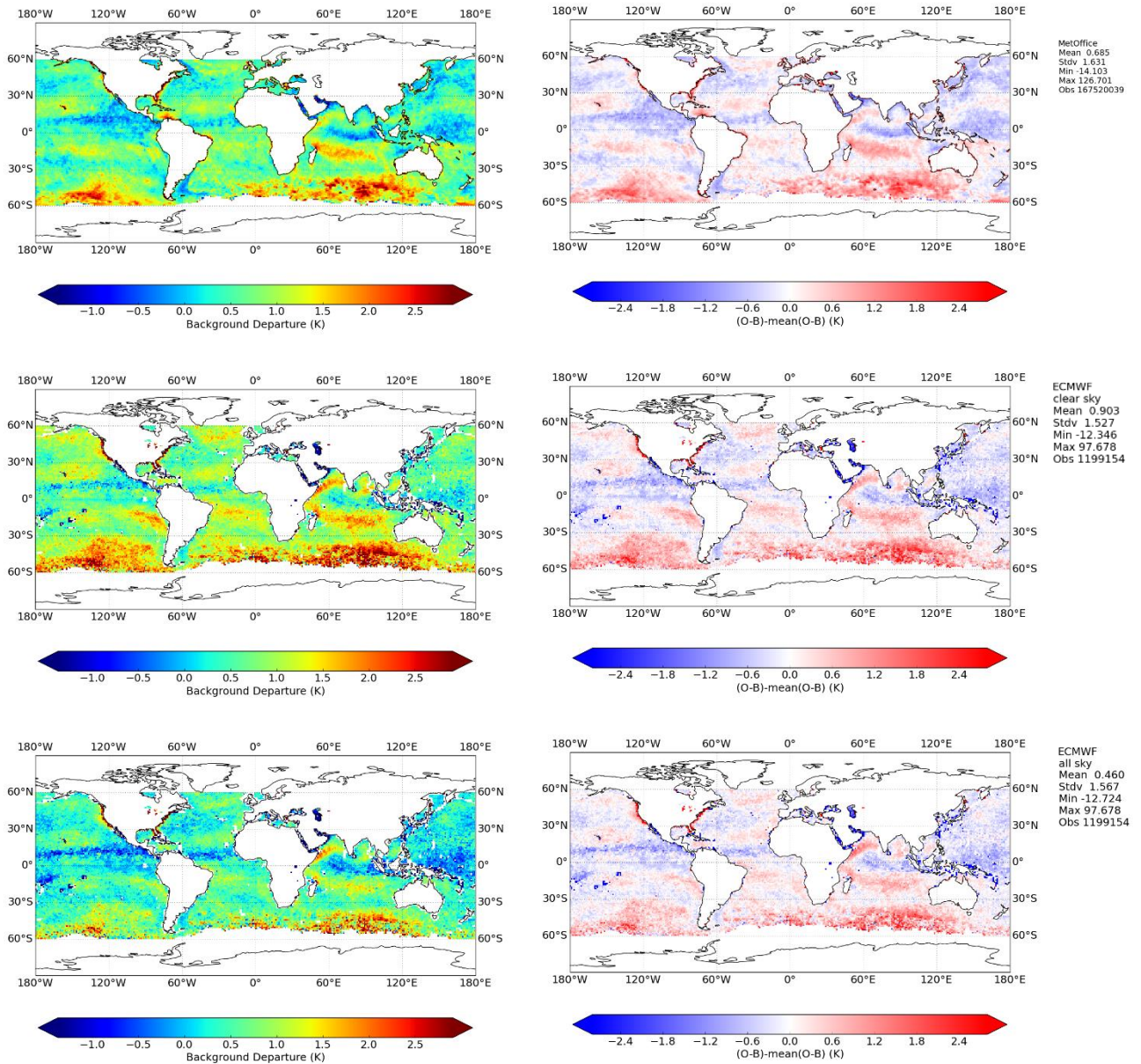
Figure B.3: Same as figure 4 but for GMI channel 3, summer.
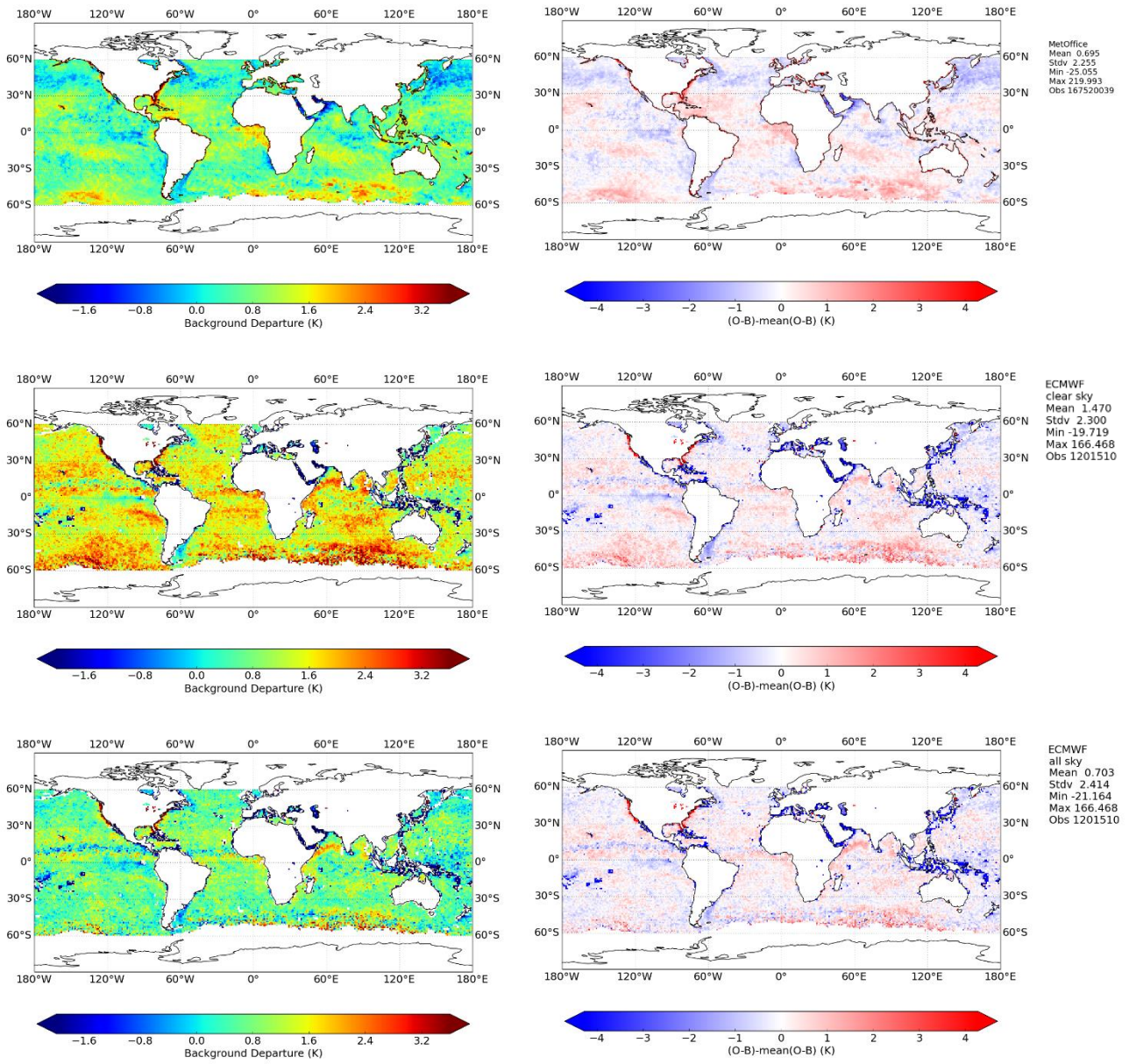
Figure B.4: Same as figure 4 but for GMI channel 4, summer.
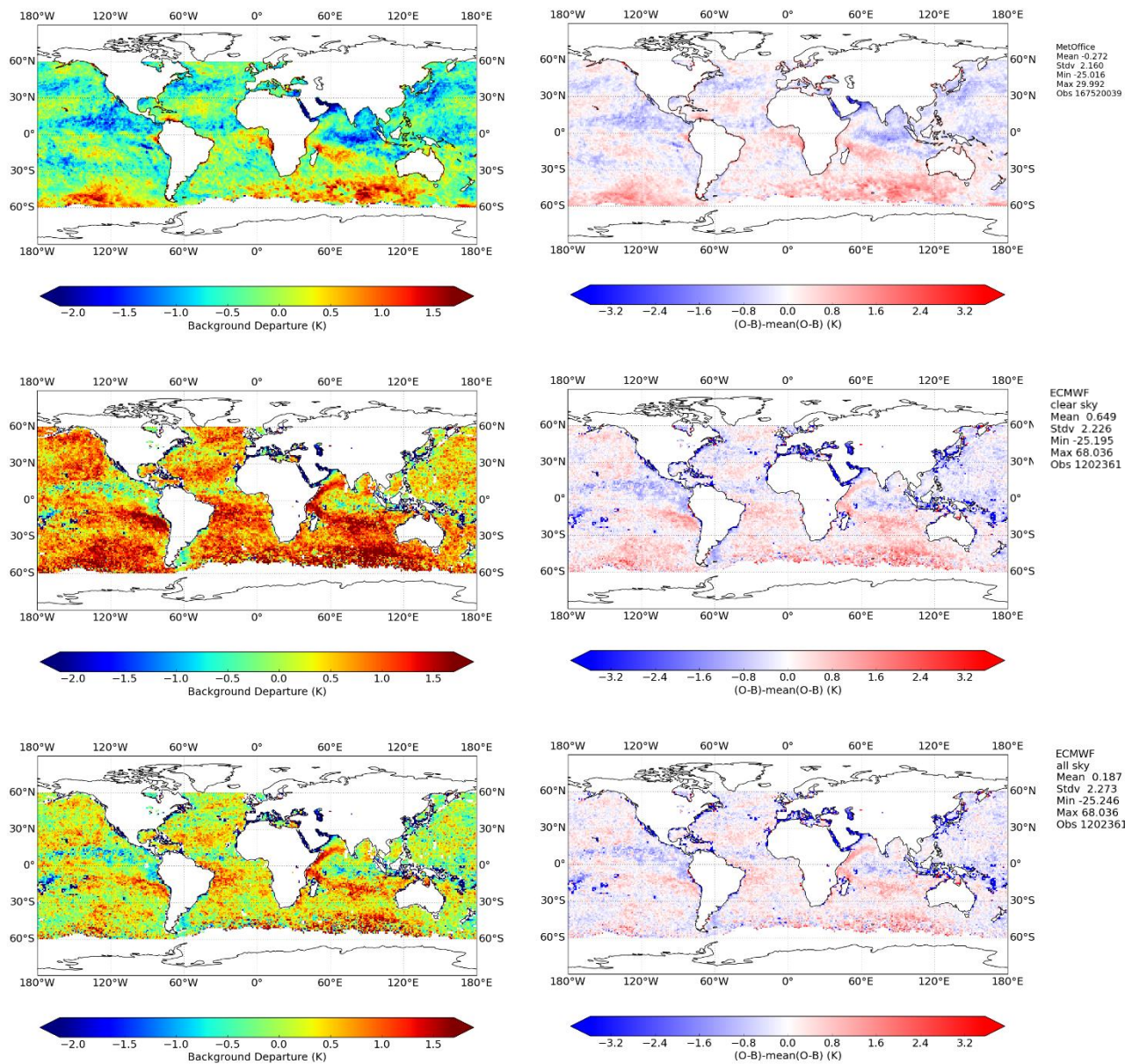
Figure B.5: Same as figure 4 but for GMI channel 5, summer.
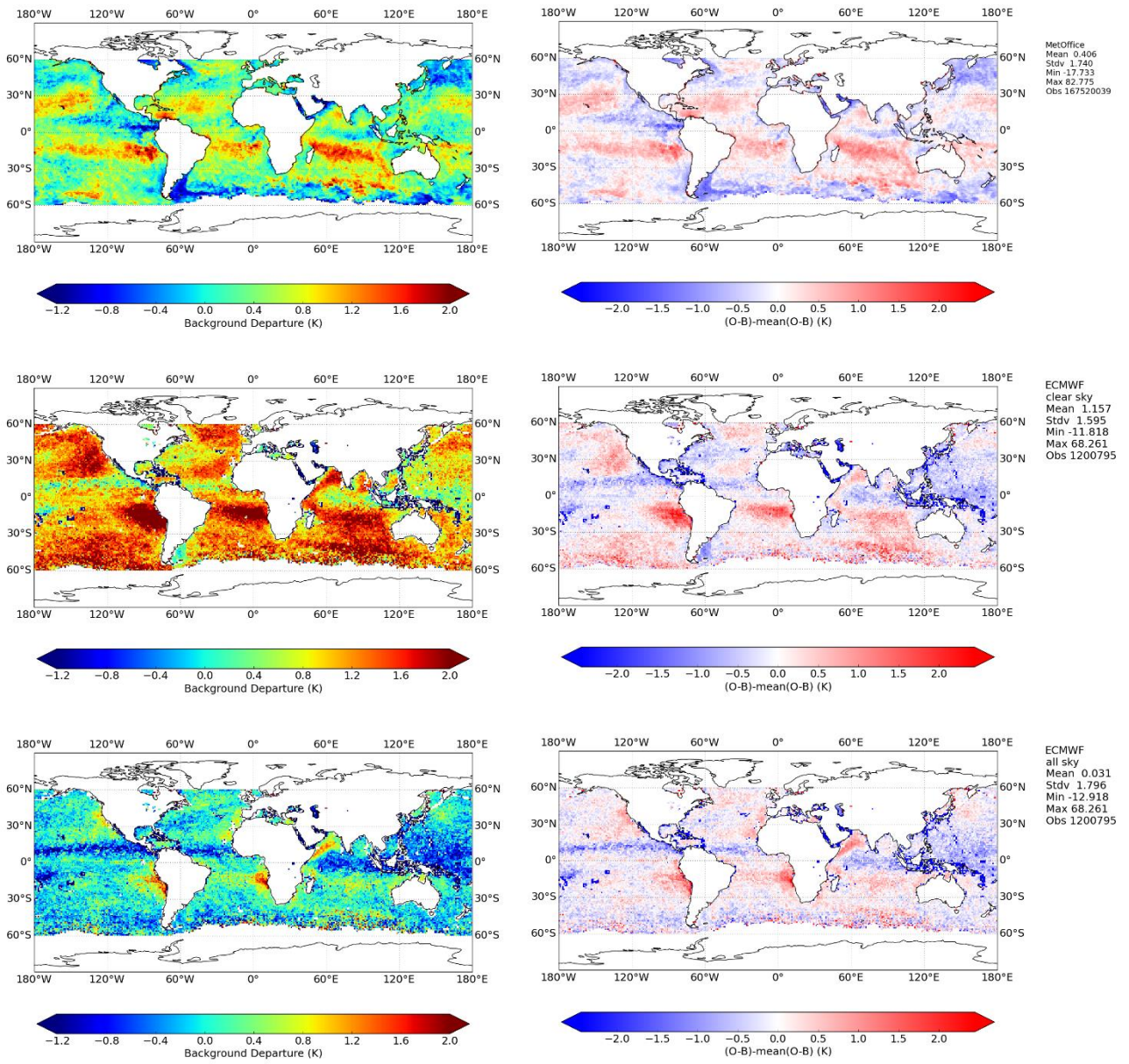
Figure B.6: Same as figure 4 but for GMI channel 6, summer.
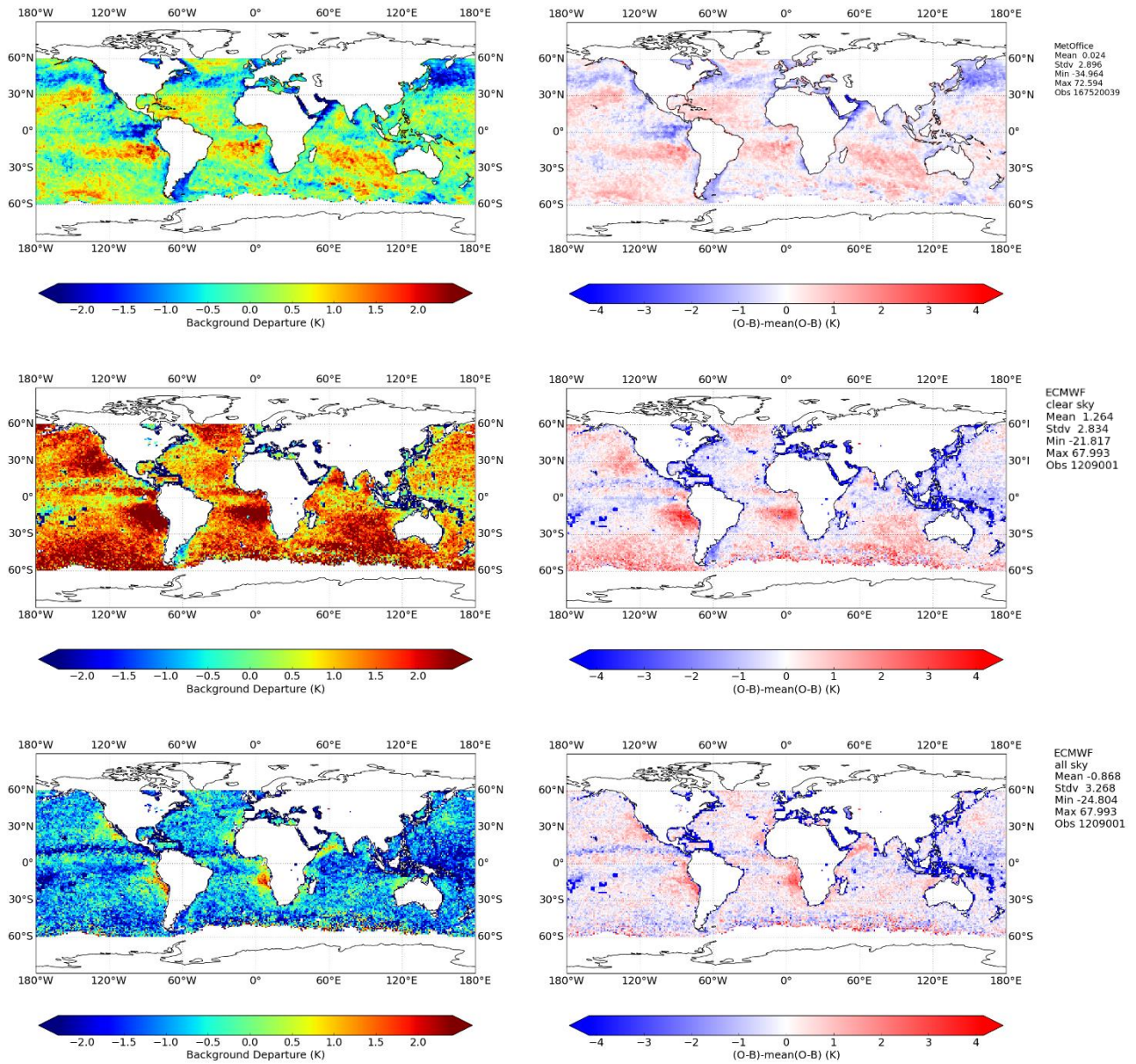
Figure B.7: Same as figure 4 but for GMI channel 7, summer.
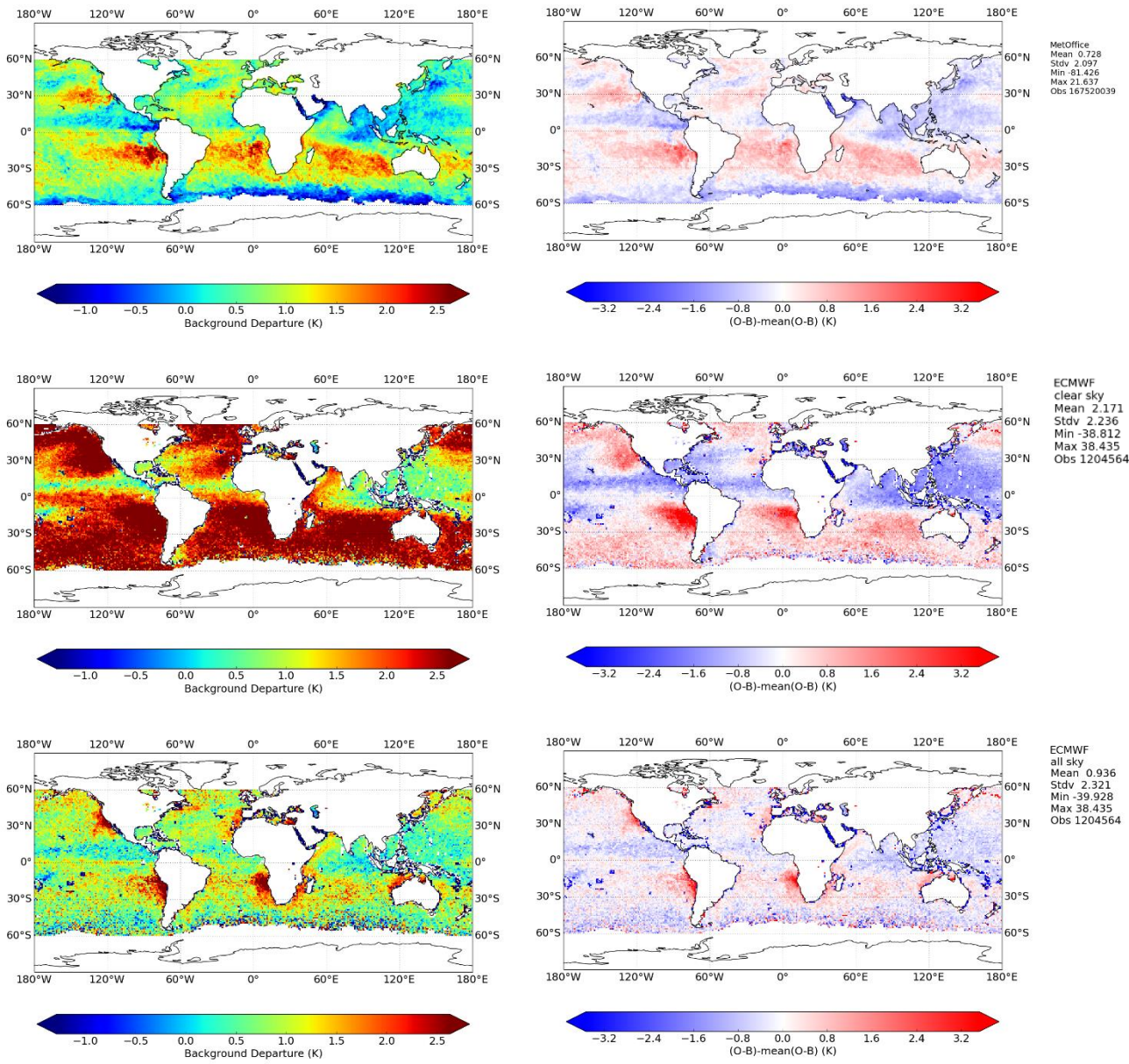
Figure B.8: Same as figure 4 but for GMI channel 8, summer.
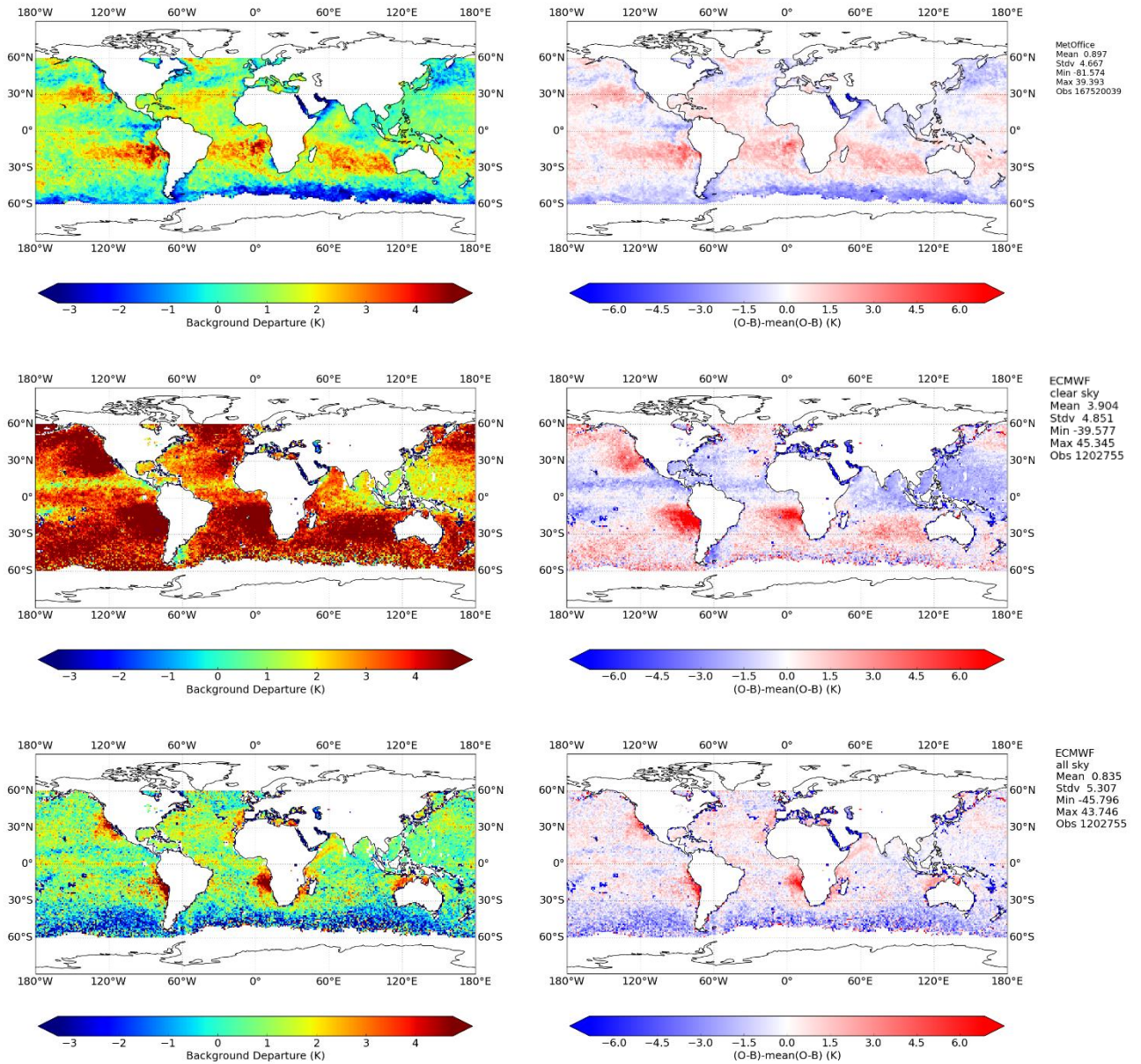
Figure B.9: Same as figure 4 but for GMI channel 9, summer.
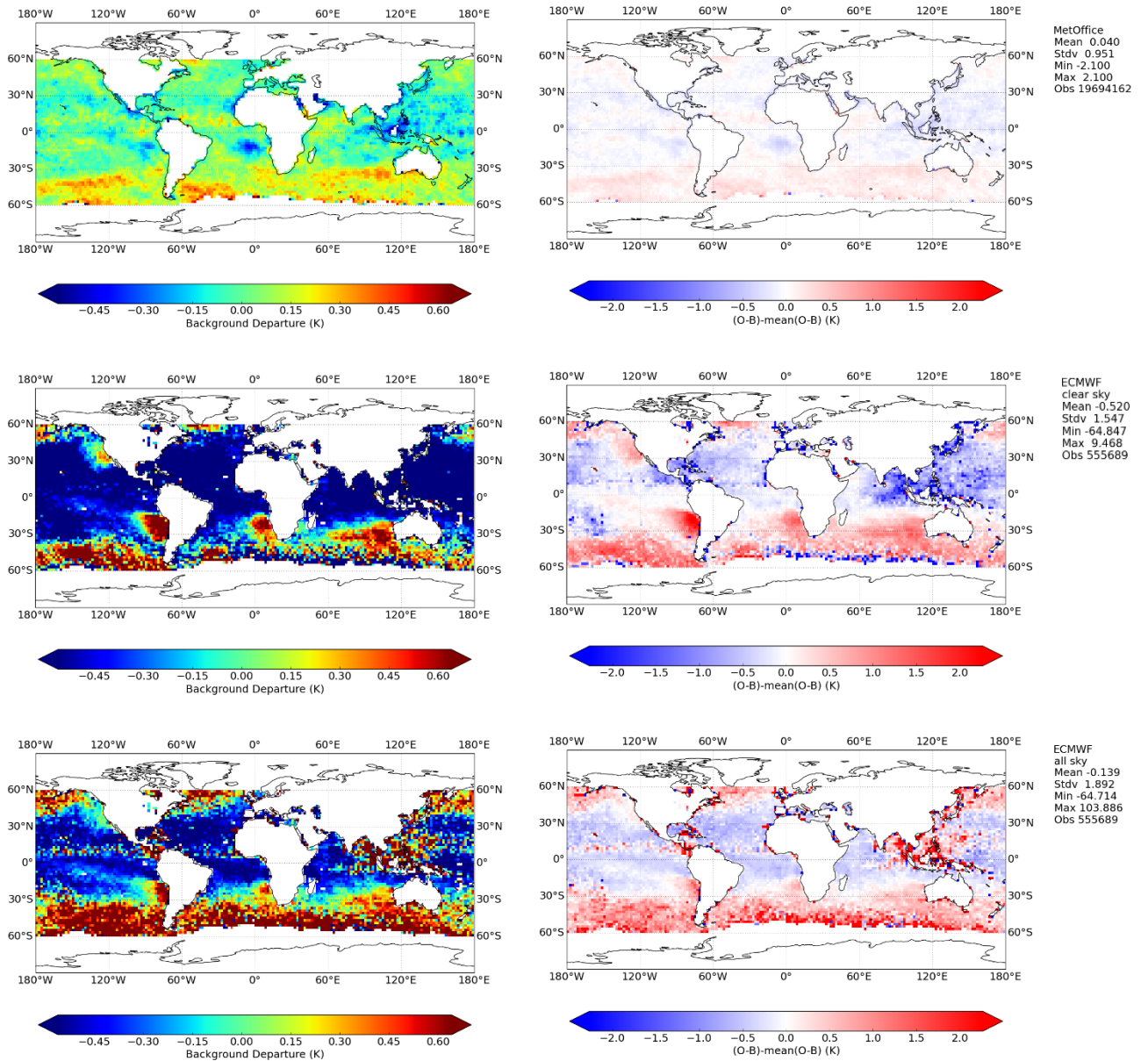
Figure B.10: Same as figure 7 but for GMI channel 10, summer.
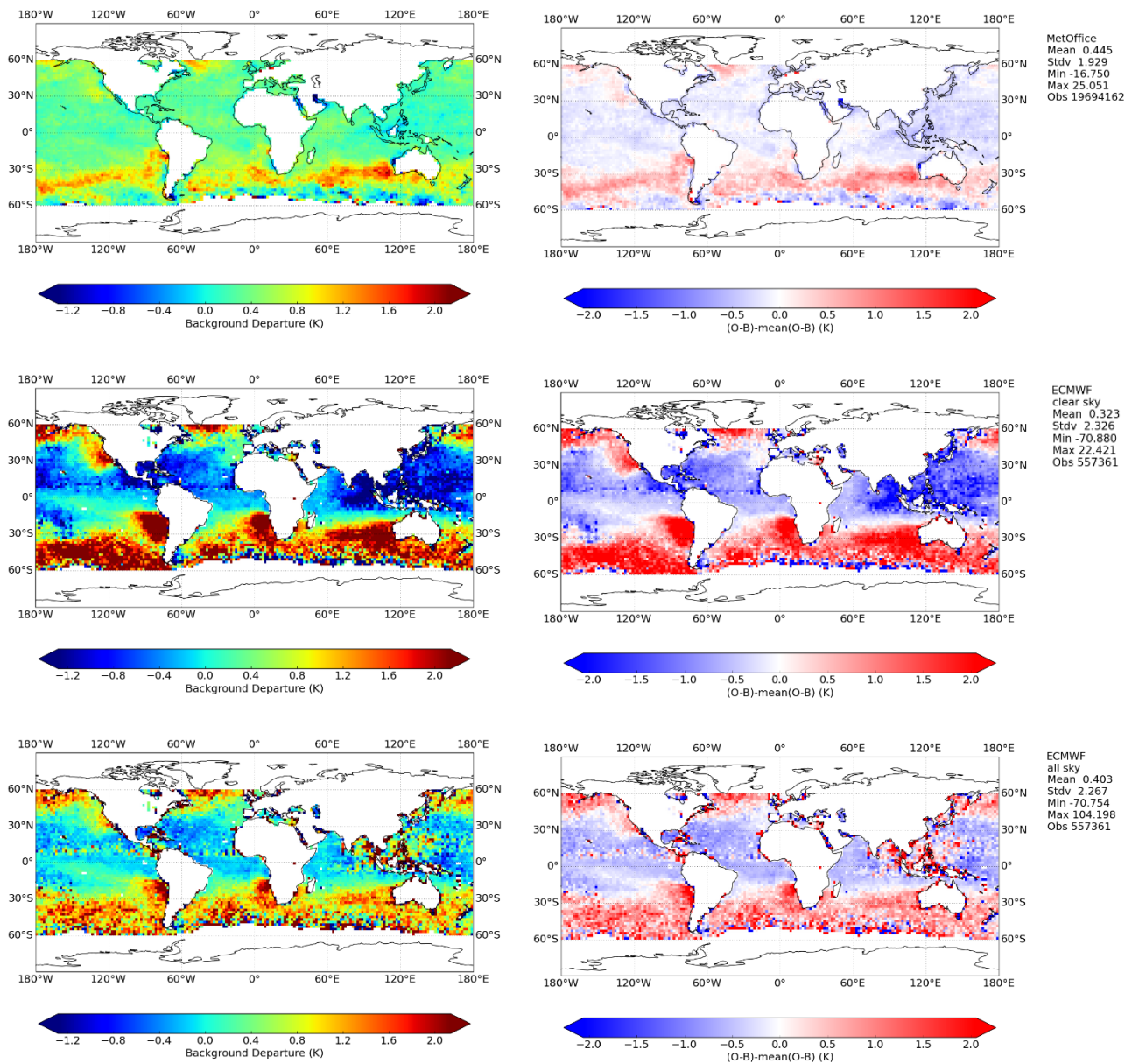
Figure B.11: Same as figure 7 but for GMI channel 11, summer.
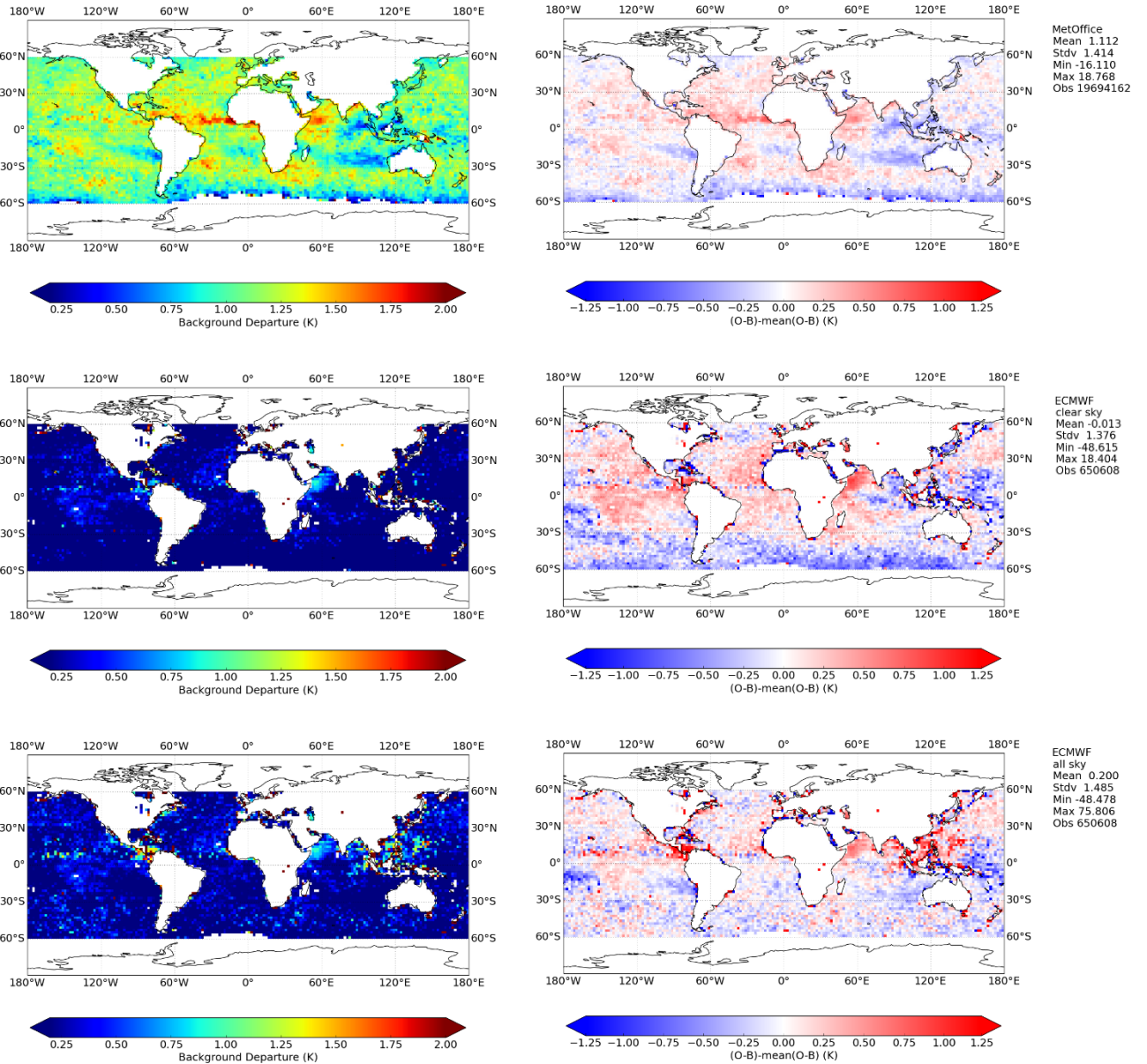
Figure B.12: Same as figure 7 but for GMI channel 12, summer.
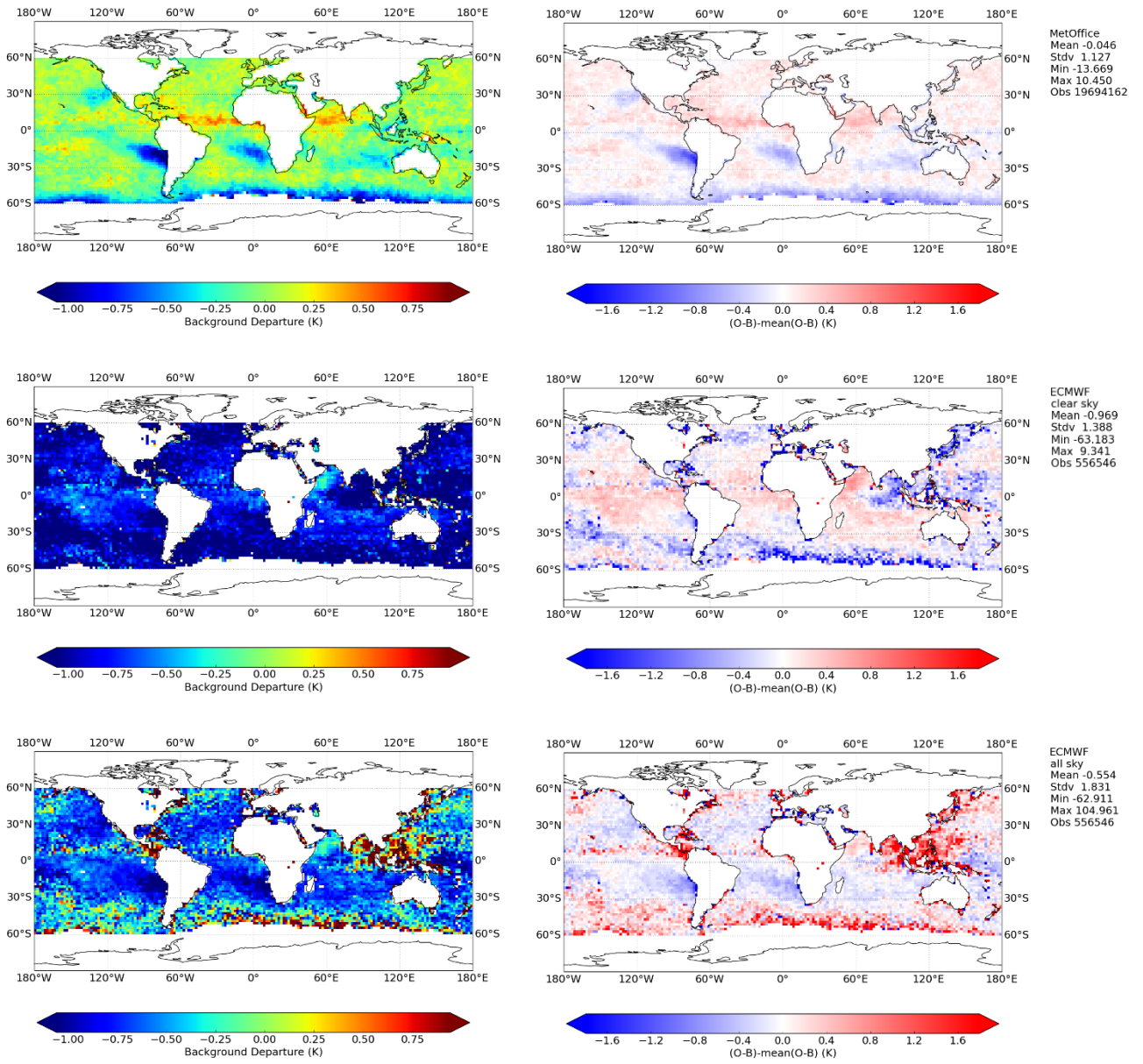
Figure B.13: Same as figure 7 but for GMI channel 13, summer.
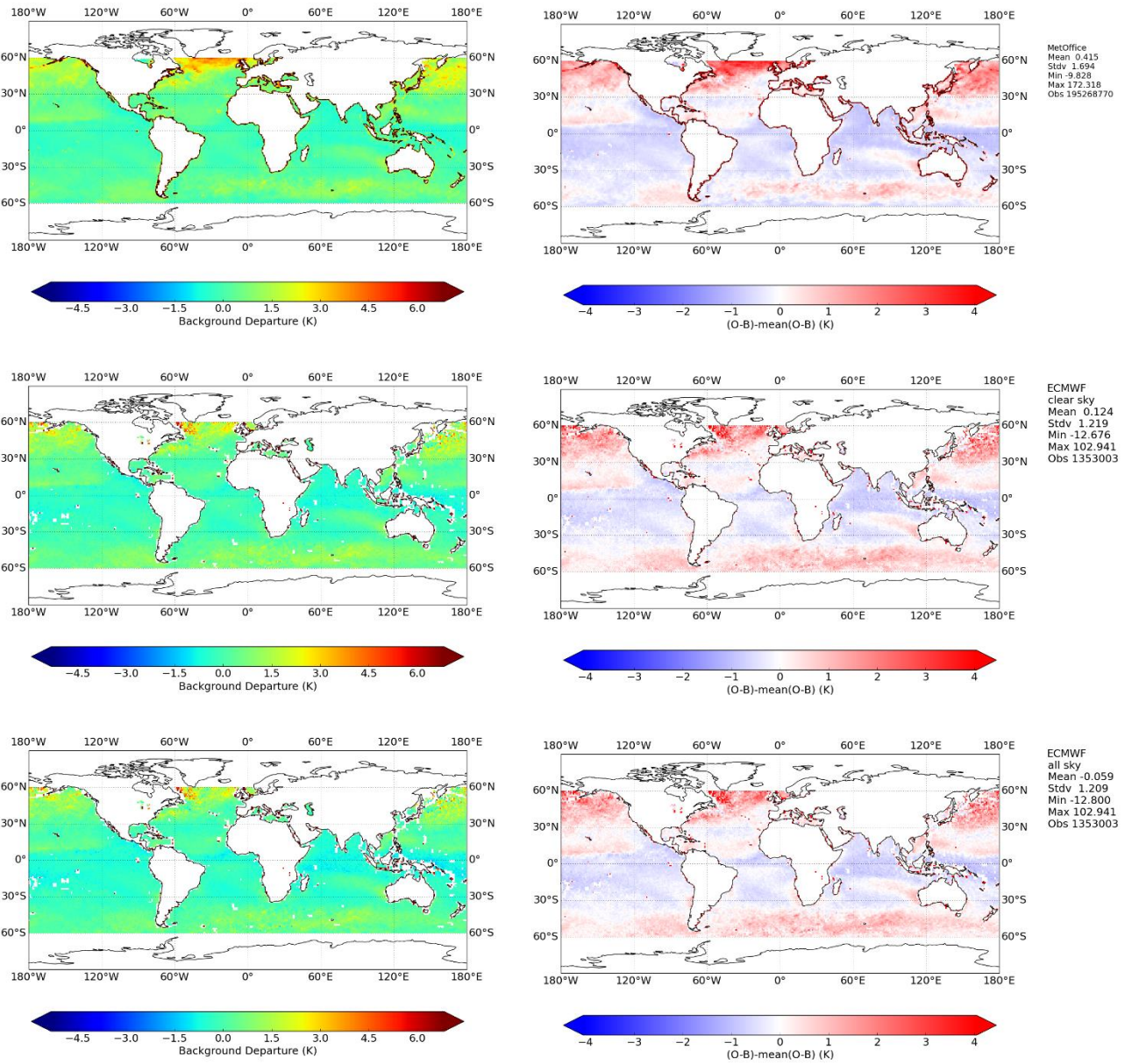
Figure B.14: Same as figure 4 but for GMI channel 1, winter.
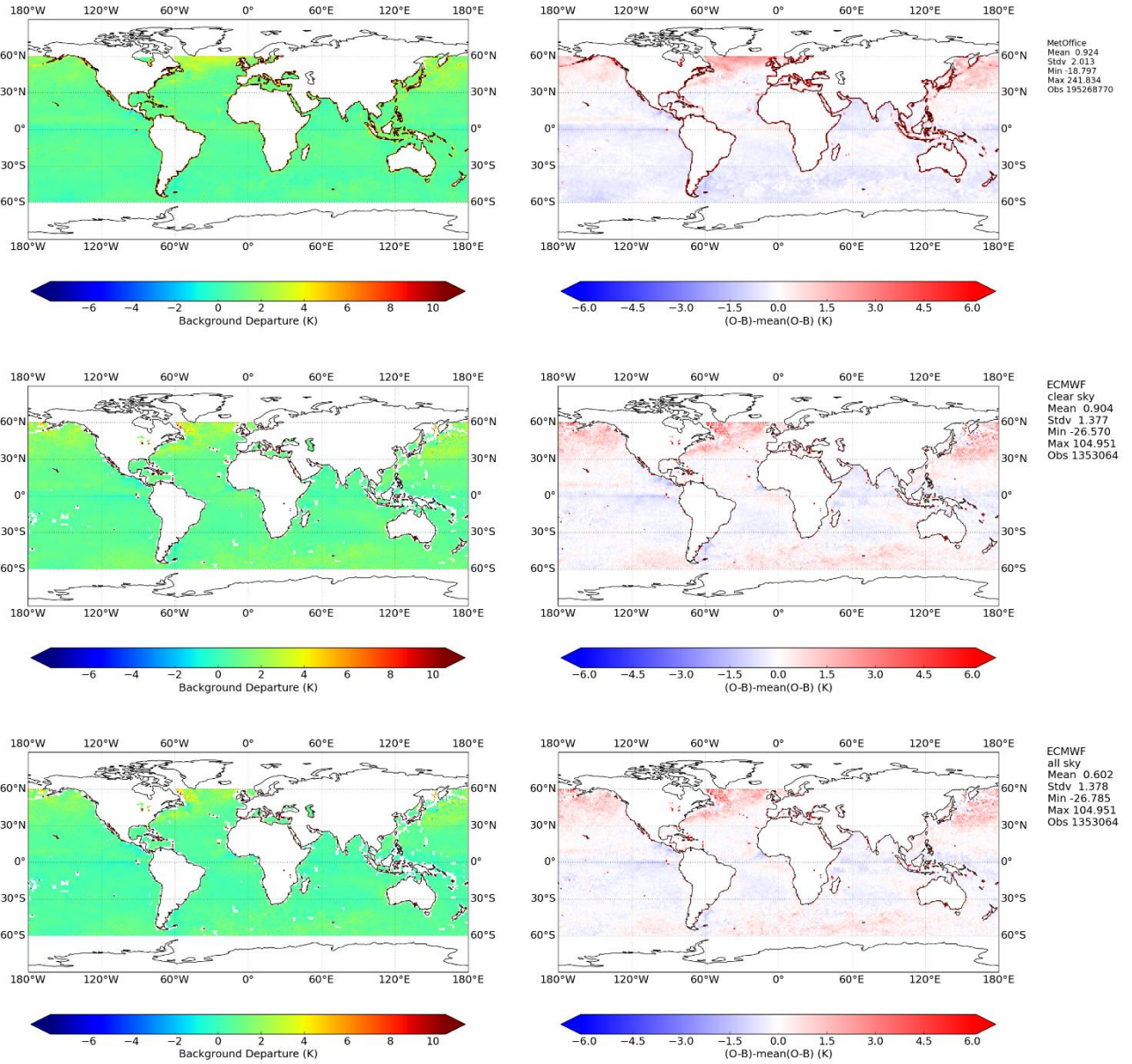
Figure B.15: Same as figure 4 but for GMI channel 2, winter.
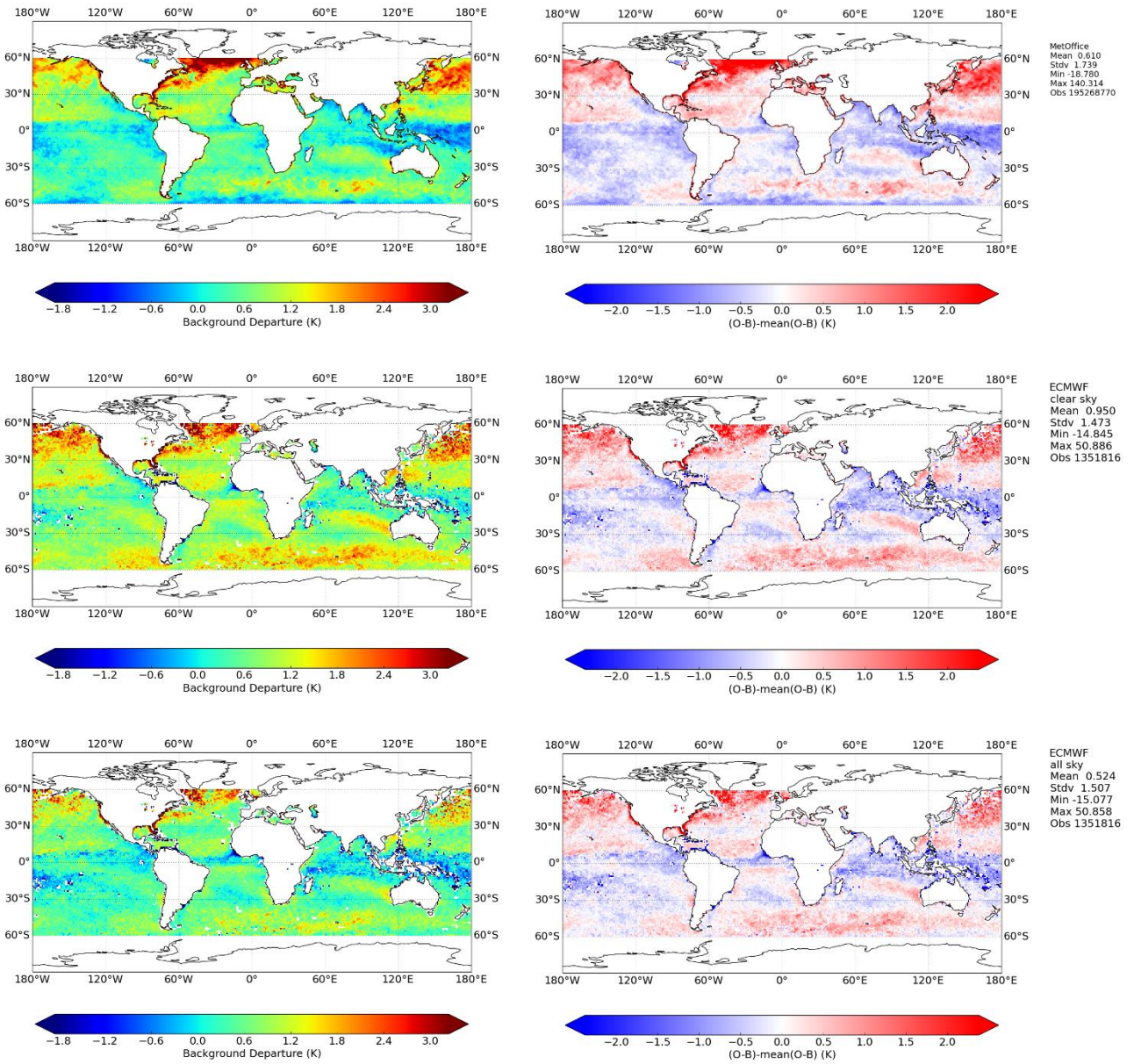
Figure B.16: Same as figure 4 but for GMI channel 3, winter.
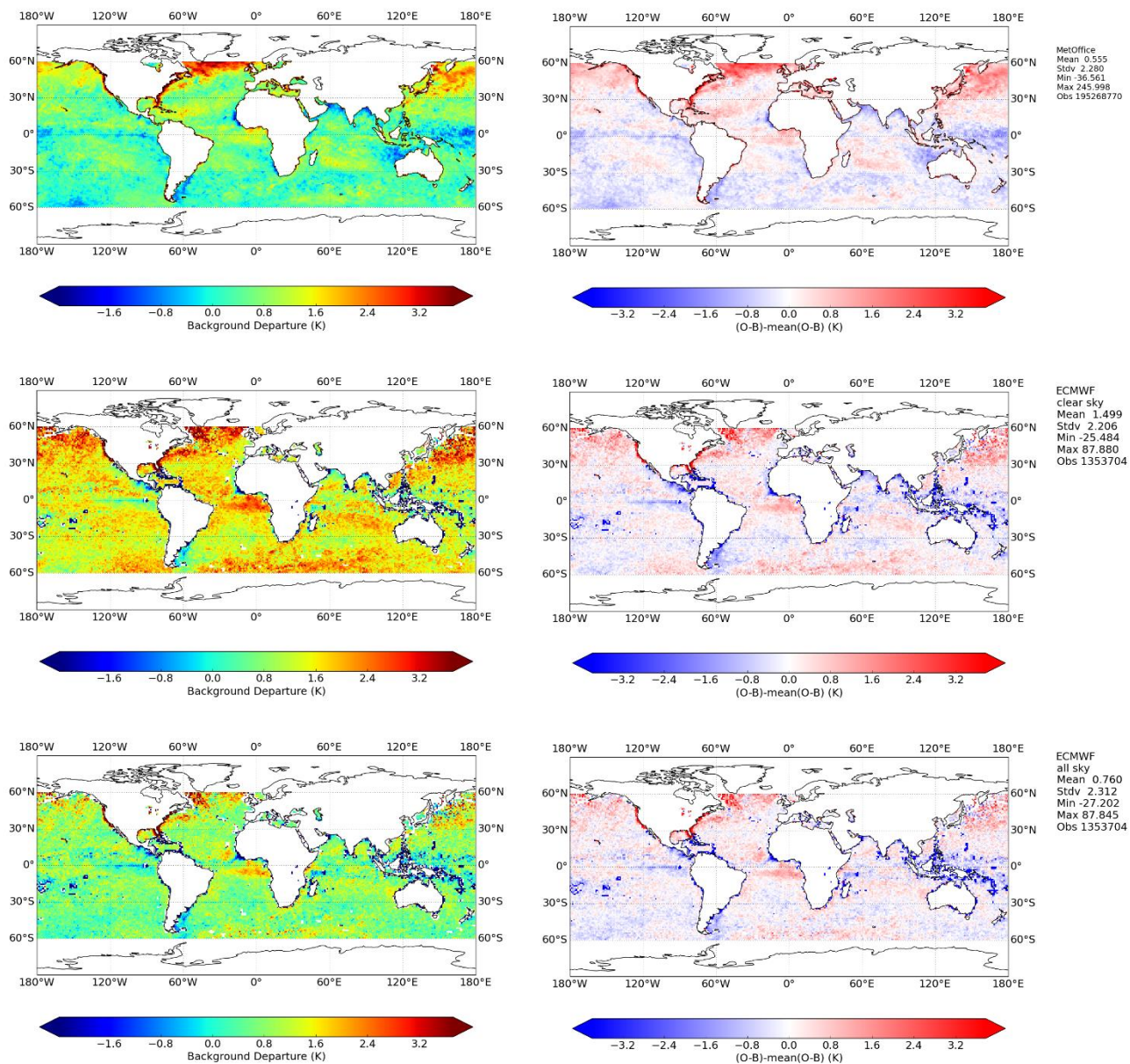
Figure B.17: Same as figure 4 but for GMI channel 4, winter.
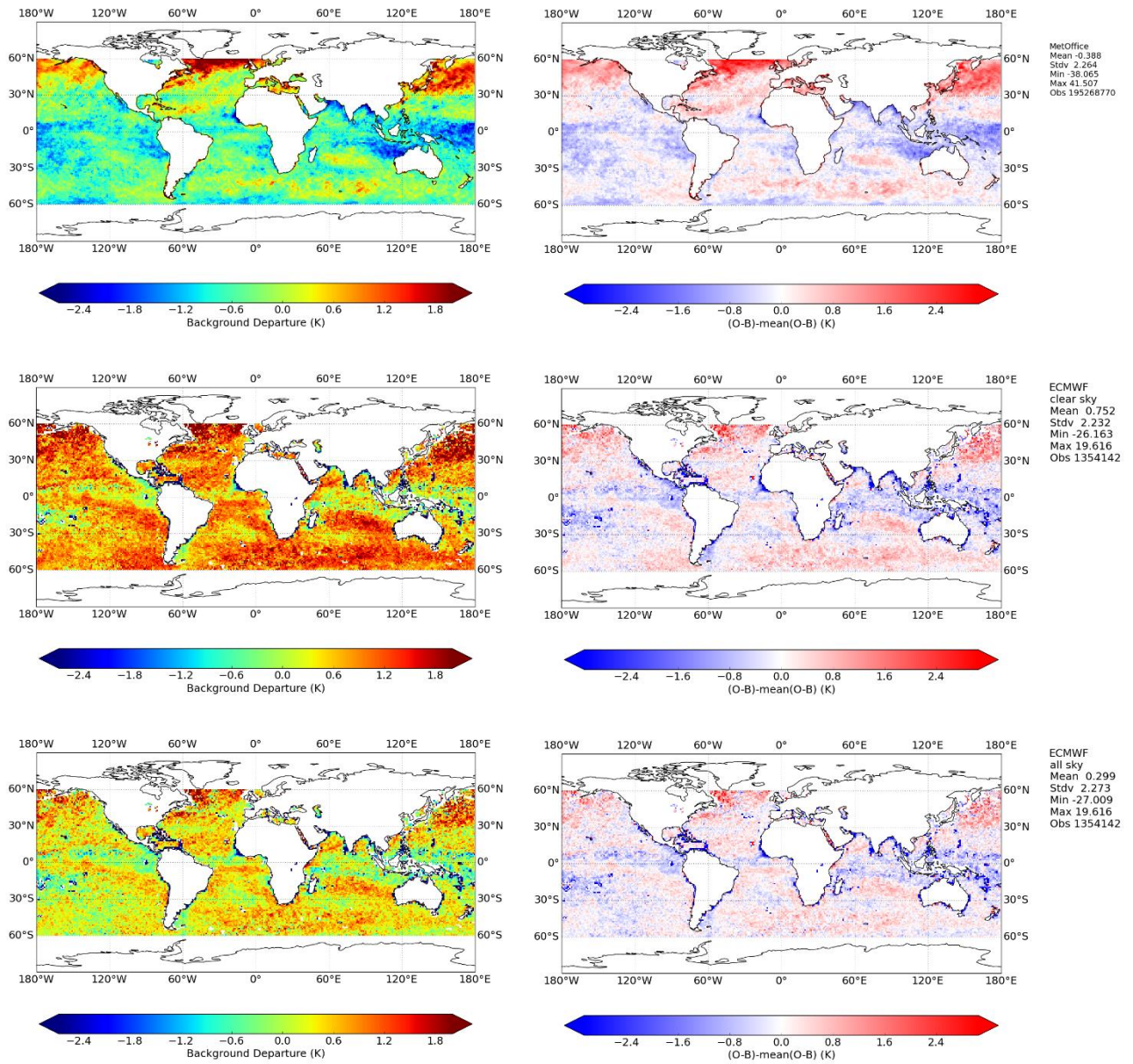
Figure B.18: Same as figure 4 but for GMI channel 5, winter.
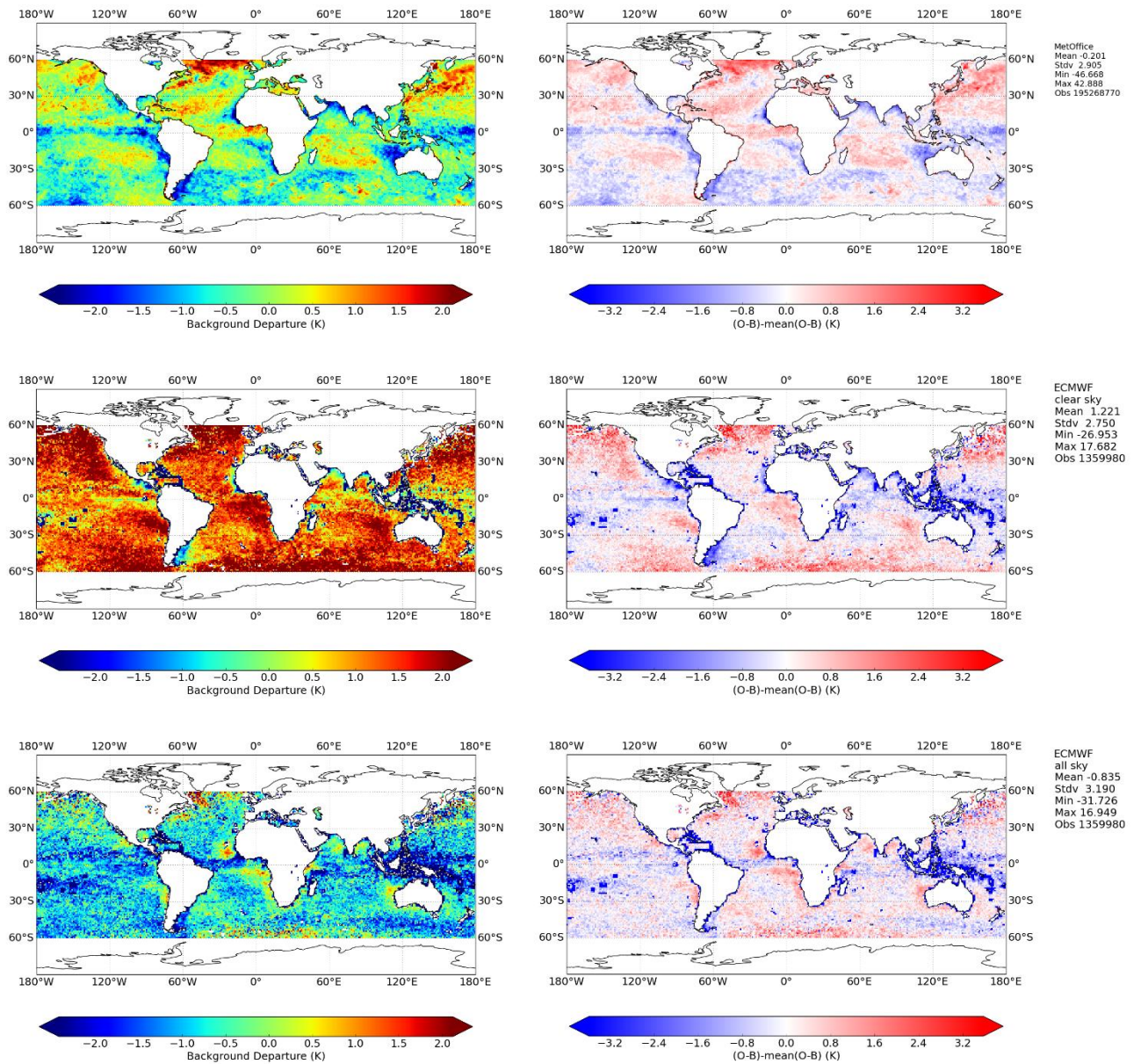
Figure B.19: Same as figure 4 but for GMI channel 7, winter.
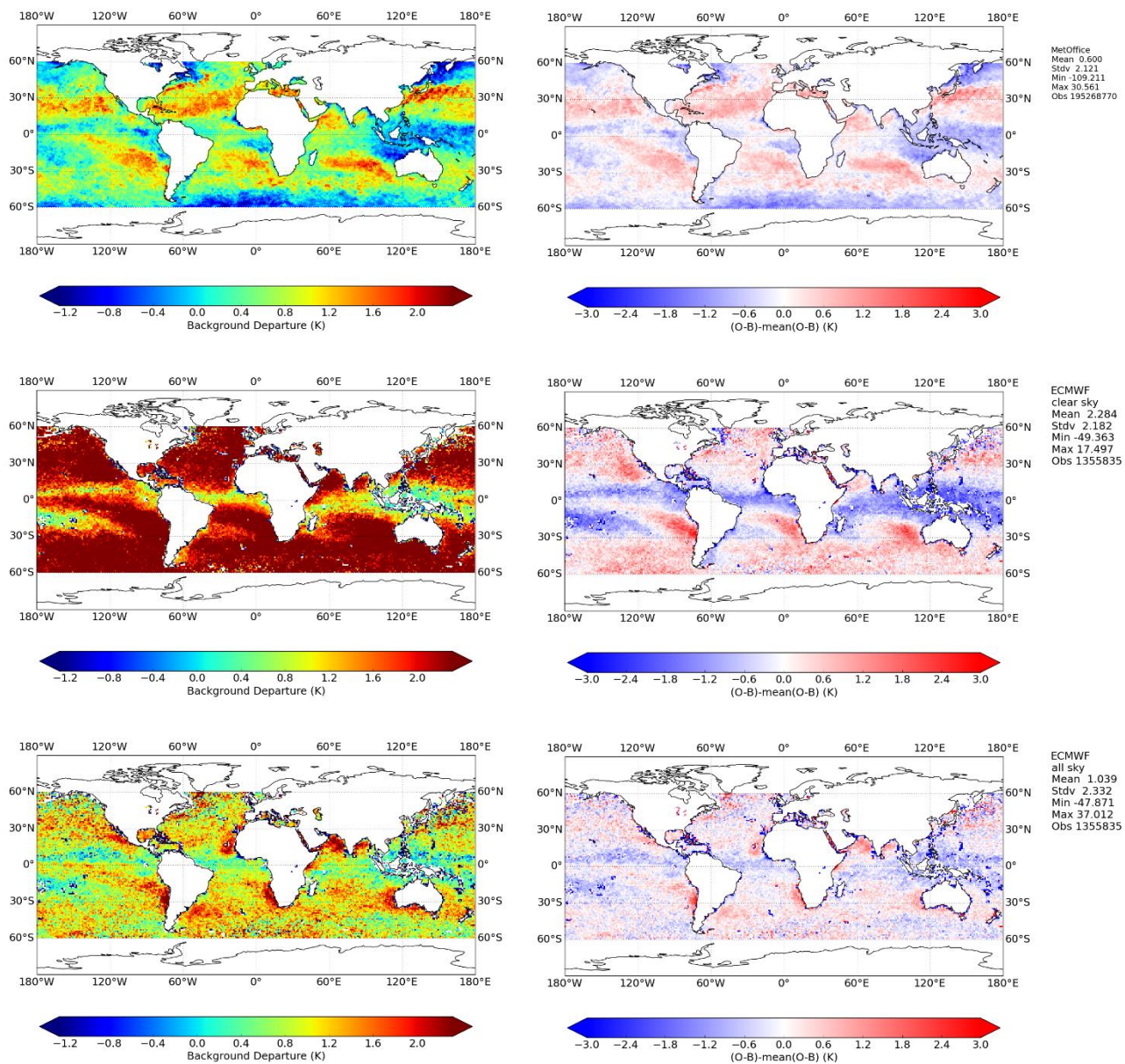
Figure B.20: Same as figure 4 but for GMI channel 8, winter.
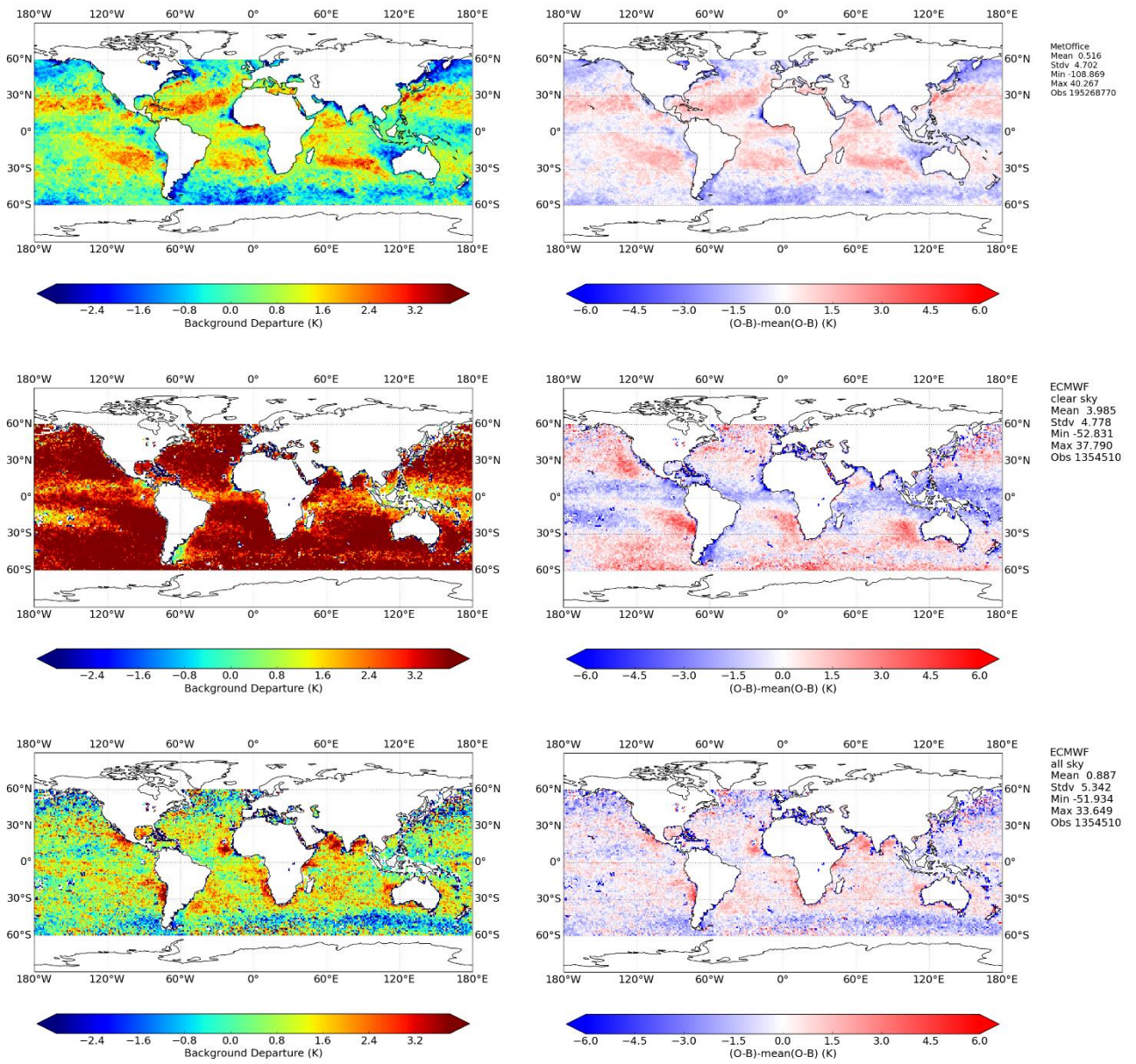
Figure B.21: Same as figure 4 but for GMI channel 9, winter.
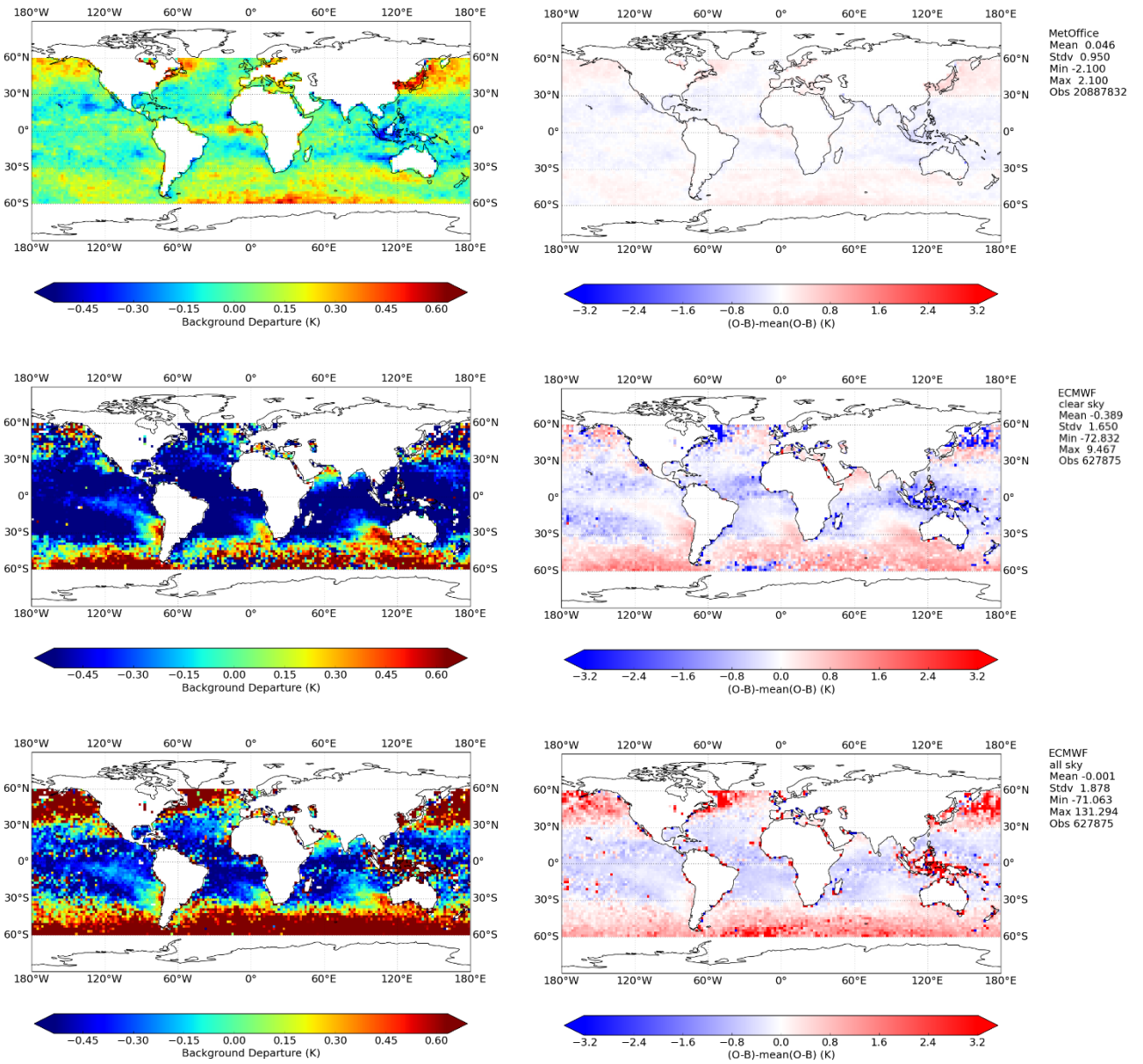
Figure B.22: Same as figure 7 but for GMI channel 10, winter.
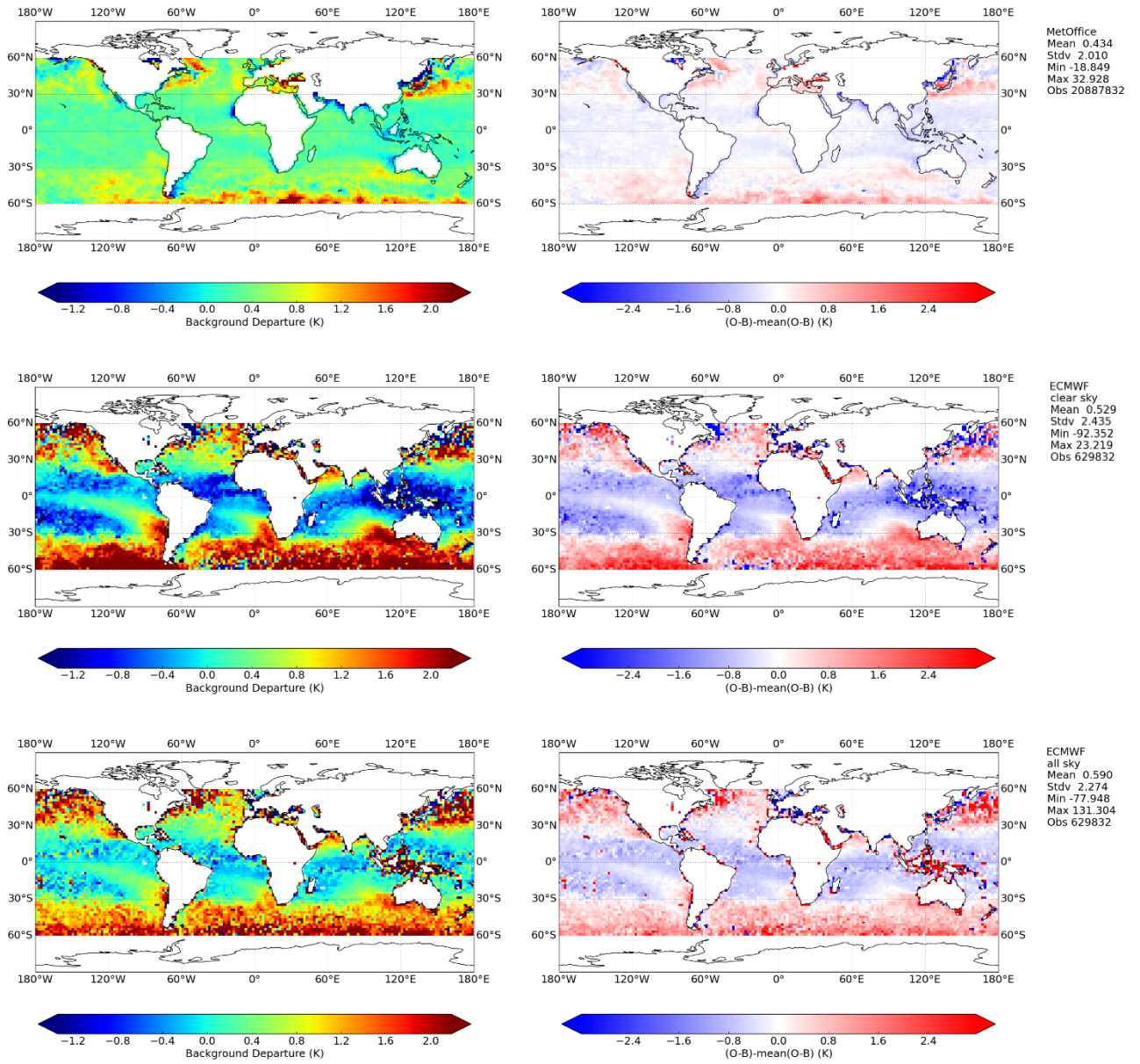
Figure B.23: Same as figure 7 but for GMI channel 11, winter.
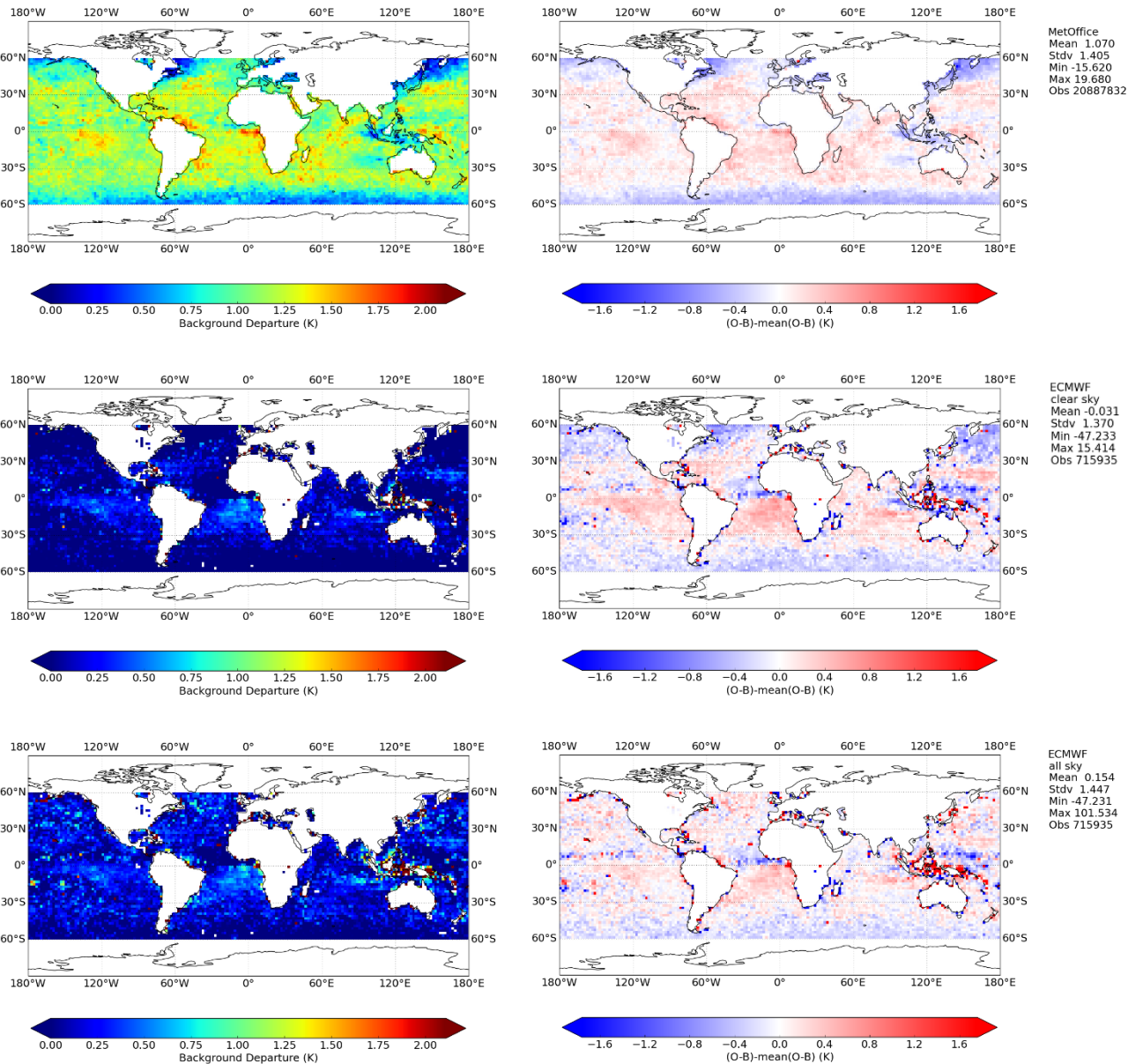
Figure B.24: Same as figure 7 but for GMI channel 12, winter.
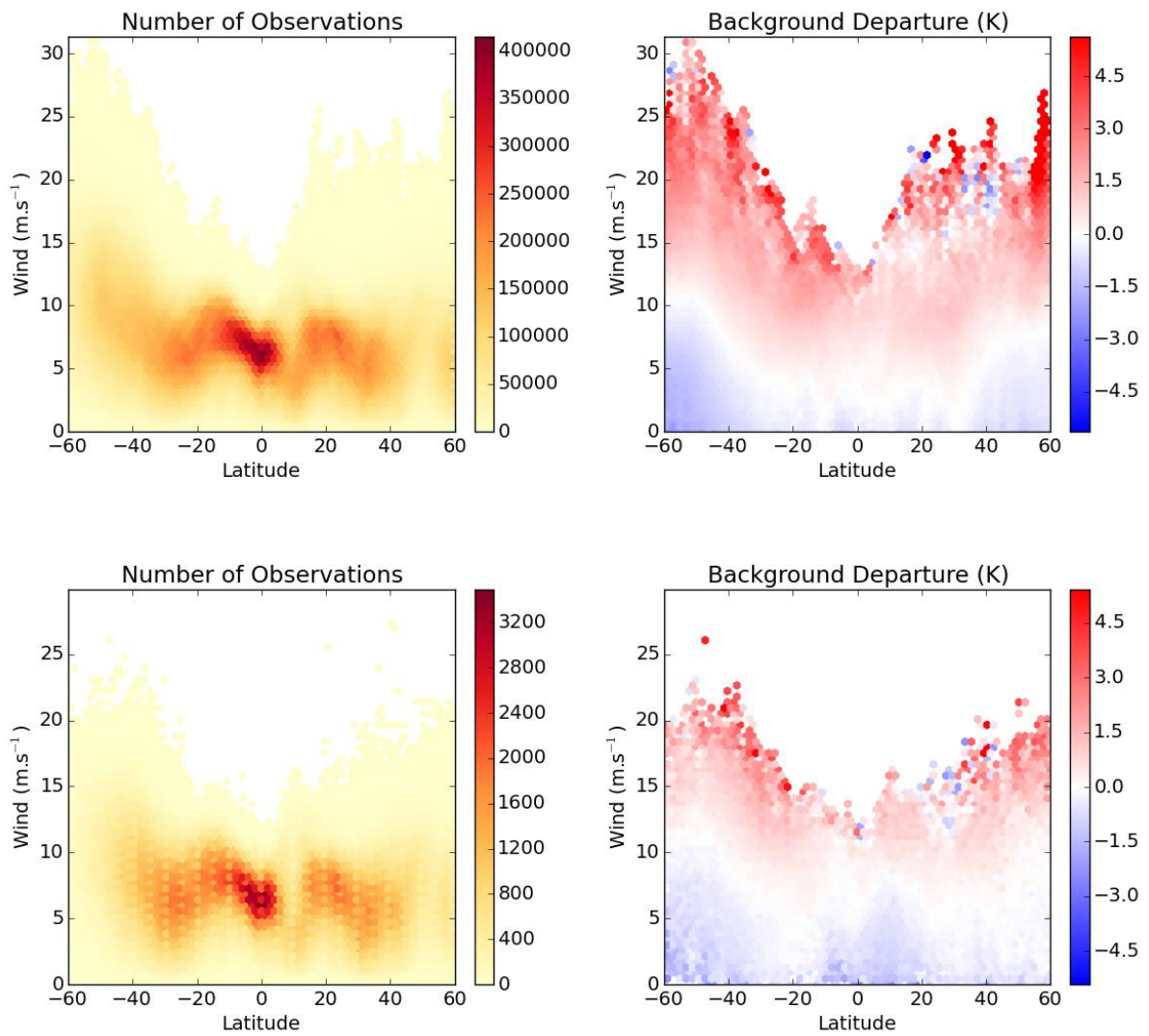
Figure C.1: Same as figure 5 but for GMI channel 6, summer.
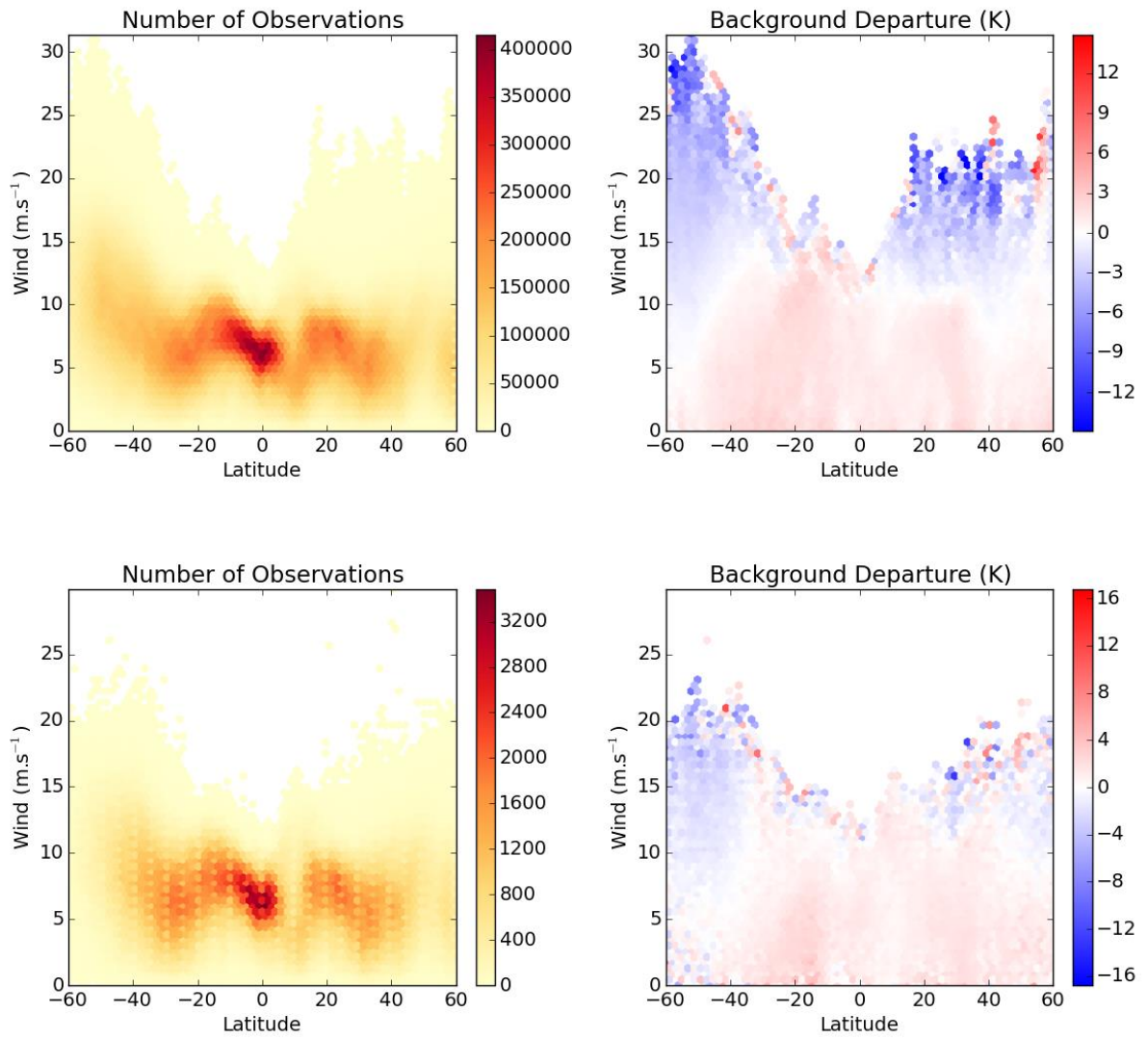
Figure C.2: Same as figure 5 but for GMI channel 9, summer.
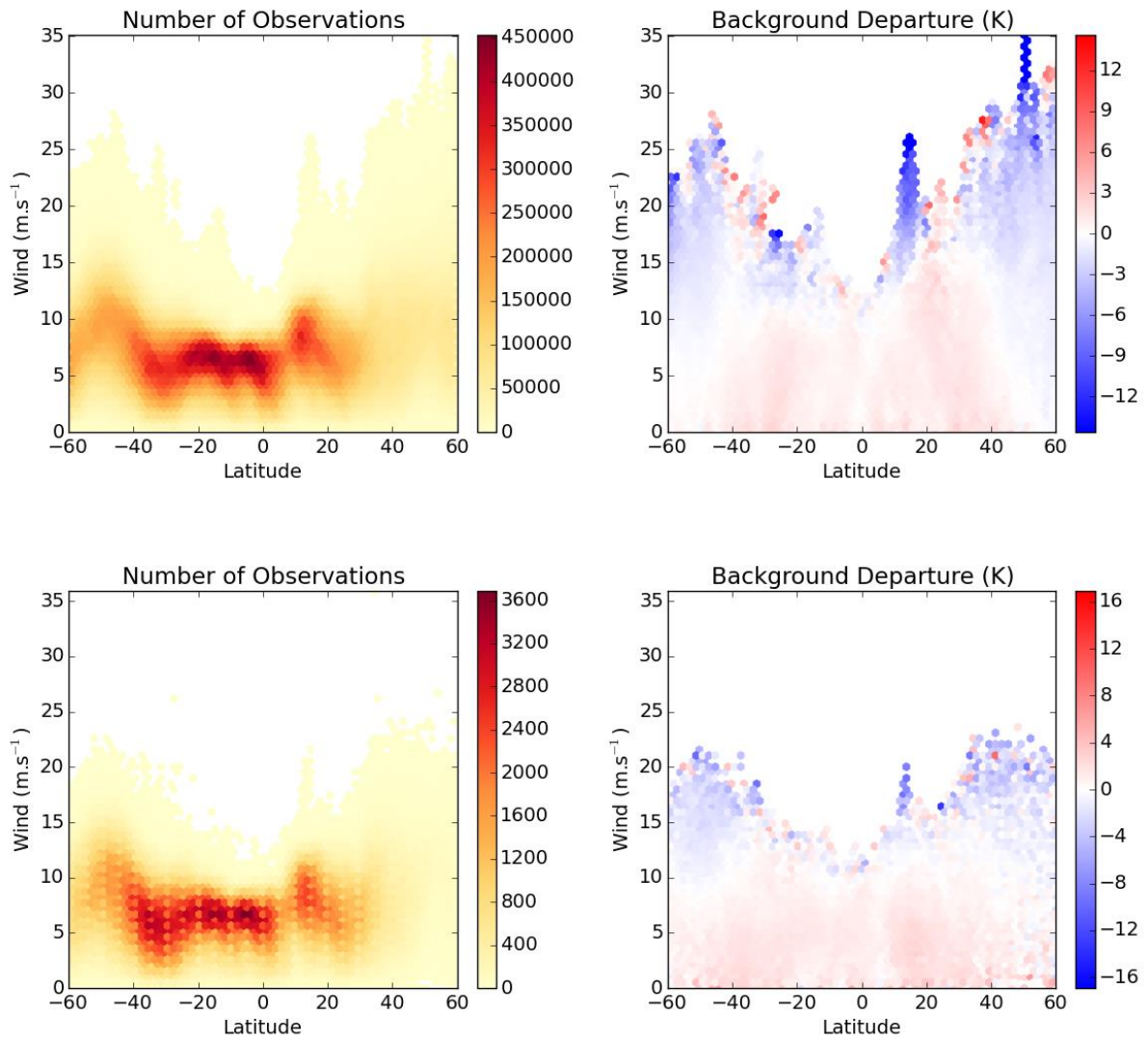
Figure C.3: Same as figure 5 but for GMI channel 9, winter.